

# POLITECNICO DI TORINO

MASTER OF SCIENCE IN CIVIL ENGINEERING



MASTER THESIS

## **Modelling and analysis of masonry building aggregates subject to various degrees of interconnection.**

### **Supervisor**

Prof. Fabio Di Trapani

### **Candidate**

Luca Medei

### **Co-supervisor**

Ing. Sofia Villar

Academic year 2023/2024

# Content

- Content ..... 1
- List of Figures ..... 4
- List of Tables..... 8
- 1. Introduction ..... 9
- 2. Seismic behaviour of unreinforced masonry aggregate buildings ..... 11
  - 2.1 The current state of the art of unreinforced masonry aggregates ..... 12
  - 2.2 Behaviour of the masonry ..... 14
  - 2.3 Global and local failure mechanisms of URMs ..... 15
  - 2.4 The “aggregate effect” ..... 19
    - 2.4.1 Impact of different floor typologies ..... 21
    - 2.4.2 Impact of Degrees of Interconnection Between Units ..... 23
- 3. Numerical modelling of masonry structures ..... 26
  - 3.1 FEM and DEM ..... 26
  - 3.2 Equivalent Frame Modelling..... 28
  - 3.3 Micro-modelling..... 32
  - 3.4 Macro-modelling: homogenized masonry approach..... 34
  - 3.5 Modelling interconnections between units..... 39
- 4. Analysis and verification methods ..... 42
  - 4.1 Modal analysis and response spectra ..... 42
  - 4.2 Nonlinear static analysis (pushover) ..... 46
    - 4.2.1 Horizontal load distribution ..... 49
  - 4.3 Non-linear dynamic analysis ..... 50
    - 4.3.1 Damping: the Rayleigh method..... 51
  - 4.4 Verification methods ..... 52
    - 4.4.1 Capacity assessment..... 53
    - 4.4.2 Seismic demand evaluation..... 54

4.4.3 Assessment criteria.....	56
5. Numerical modelling of aggregate buildings in Opensees using STKO .....	57
5.1 Introduction to OpenSees .....	57
5.2 Numerical modelling approach .....	60
5.2.1 Masonry structure modelling approach.....	60
5.2.2 Modelling of the slab.....	68
5.2.3 Modelling of the floor beams .....	69
5.2.4 Modelling of the connection between orthogonal walls .....	72
5.2.5 Modelling of openings in masonry walls .....	73
5.2.6 Modelling of connection between units of the URM aggregate. ....	74
5.2.7 Modelling Choices Summary .....	76
6. Characterization of the mortar connection.....	78
6.1 Mohr-Coulomb law .....	78
6.2 Material properties of the different mortars considered.....	79
6.3 Model definition.....	80
6.4 Mortar characterization. ....	83
7. Description of the aggregate case study.....	86
7.1 Geometry .....	86
7.2 Numerical models .....	89
7.3 Masonry material properties calibration .....	91
7.4 Material properties .....	93
7.5 Loads, masses and conditions .....	95
7.6 Analysis settings.....	96
7.7 Mesh architecture .....	100
8. Analysis and verification results .....	103
8.1 Eigenvalue analysis results.....	103
8.2 Non-linear static analysis results.....	107

8.2.1 Pushovers in positive direction .....	107
8.2.2 Pushovers in negative direction.....	111
8.2.3 Damage Analysis.....	114
8.3 Quantitative verification using the N2 method. ....	121
8.4 Non-linear dynamic analysis results .....	129
8.5 Results comparison and discussion .....	134
9. Conclusion.....	141
Appendix A .....	144
References .....	148

# List of Figures

Figure 1: Masonry aggregate building, Trevi, Italy. ....	11
Figure 2: Growth mechanism of aggregates (12).....	13
Figure 3: Example of masonry on existing buildings. ....	14
Figure 4: Masonry constitute model.....	15
Figure 5: In-plane failure mechanisms of masonry walls (20).....	16
Figure 6: (a) walls rigidly connected; (b) walls not connected (21). ....	17
Figure 7: Overturning mechanisms (21). ....	18
Figure 8: Vertical flexural mechanisms (21) .....	18
Figure 9: Horizontal flexural mechanisms (21). ....	19
Figure 10: Composed overturning mechanisms (21). ....	19
Figure 11: (a) stiff diaphragm; (b) rigid diaphragm (24). ....	21
Figure 12 (a) Rigid diaphragm; (b) Flexible diaphragm. ....	22
Figure 13: Details of the damage occurred between structural units (2). ....	23
Figure 14: Plan view (a) and model (b) of masonry aggregate tested in (7).....	24
Figure 15: Interface between units in the masonry aggregate (7). ....	24
Figure 16: Collapse mechanism obtained using DEM (a) and FEM/DEM (b) (20). ....	28
Figure 17: (a) Wall geometry; (b) schematization with infinitely rigid nodes; (c) schematization of Dolce (21). ....	30
Figure 18: (a)Example aggregate in Basel (Switzerland); (b) Laboratory tested masonry aggregate (8).....	31
Figure 19: EFM of the aggregate building (34). ....	32
Figure 20: a) Detailed micro-modelling; b) simplified micro-modelling. ....	32
Figure 21: Failure mechanisms of masonry (16). ....	33
Figure 22: (a) Experimentally obtained Crack pattern (b) Model results Crack pattern (41)..	34
Figure 23: Homogenized masonry. ....	35
Figure 24: Homogenization technique (42). ....	35
Figure 25: Experimental crack pattern of the tested wall (42). ....	37
Figure 26: Comparison between experimental results, interface model and homogenization model: (a) horizontal force vs. displacement; (b) vertical force vs. displacement (42). ....	37
Figure 27: Pushover curves: experimental results and numerical modelling (19). ....	38
Figure 28: Parametrical study: a) influence of the compressive strength; b) influence of the tensile strength (19). ....	38

Figure 29: Parametrical study: a) influence of the compressive fracture energy; b) influence of the tensile fracture energy (19).....	38
Figure 30: EFM model of the external unit (25).....	39
Figure 31: Pushover curves of (a) the intermediate unit and (b) external unit (25).....	40
Figure 32: Equivalent Frame Model of the aggregate (8).....	40
Figure 33: constitutive CohesionFriction3D model for unit-to-unit connections (8). ....	41
Figure 34: Comparison of seismic fragility curves for the four aggregate modelling approaches presented in (8).....	41
Figure 35: Modal decomposition of a n-degree of freedom system (47).....	42
Figure 36: Technical code elastic spectrum (50). ....	44
Figure 37: Inelastic constant ductility spectra.....	45
Figure 38: Newton-Raphson method illustrated (55).....	48
Figure 39: Newton-Raphson methods is not suitable for problems involving softening, buckling (55), .....	48
Figure 40: Capacity curves under uniform and modal horizontal load profiles, the real solution in between. (21).....	50
Figure 41: Rayleigh damping (51). ....	52
Figure 42: Equivalent SDOF capacity curve.....	53
Figure 43: Bilinear equivalent capacity curve.....	54
Figure 44: Elastic Spectrum. ....	55
Figure 45: The STKO work tree. ....	58
Figure 46: Layered Shell section(61).....	62
Figure 47: schematic representation of the elastic predictor followed by the plastic and damage correctors in a representative uniaxial case (62) .....	65
Figure 48. Energy dissipated by $e_2$ and $e_1$ .....	67
Figure 49: Rigid diaphragm example.....	69
Figure 50: Fiber section element (66). ....	70
Figure 51: Lumped and distributed plasticity (69).....	71
Figure 52: Zero length element structure (71). ....	73
Figure 53. Lintel geometry.....	74
Figure 54: EqualDOF interaction between mortar layer and masonry wall. ....	76
Figure 55: Modelling choices summary.....	77
Figure 56: Mohr-Coulomb failure criteria. ....	79
Figure 57: Mortar characterization model.....	81

Figure 58: Mortar characterization test set-up. ....	82
Figure 59: Results of Mortar Test. ....	83
Figure 60: Mortar Failure Conditions. ....	84
Figure 61: Reference aggregate's geometry: (a) Front wall; (b) Back wall.....	86
Figure 62: Units in the aggregate. ....	87
Figure 63: Front wall. ....	87
Figure 64: Middle wall. ....	87
Figure 65: Back wall. ....	88
Figure 66: a) External walls; b) internal walls; c) U1-U2 and U2-U3 shared walls. ....	88
Figure 67: orientation of slabs.....	88
Figure 68: (a) Fully-Connected aggregate (b) Rigid diaphragm.....	89
Figure 69: isolated units: (a) unit 1; (b) unit 2; (c) unit 3.....	90
Figure 70: Semi-Connected aggregate. ....	90
Figure 71: (a) Experimental cyclic test; (b) 3D numerical model (74).....	91
Figure 72: Results from experimental test: a) Door Wall; b) Window Wall (75). ....	91
Figure 73: Experimental and numerical curves: (a) Door Wall; (b) Window Wall (74). ....	92
Figure 74: Masonry constitutive model used in this study.....	93
Figure 75: Mortar constitutive model.....	95
Figure 76: Control node position for each analysis.....	99
Figure 77: Earthquake record of the L'Aquila earthquake at the Aterno-Colle Grilli station in 2009.....	100
Figure 78: Fully-Connected Model Partitioning. ....	101
Figure 79: Isolated Model Partitioning. ....	101
Figure 80: Semi-Connected Model Partitioning. ....	102
Figure 81: Pushover curves in positive direction. ....	108
Figure 82: Repartition of loads related to the aggregate-effect.....	109
Figure 83: Reaction forces measured in longitudinal walls in the X(+) direction with respect to the displacement of the barycenter of the unit. ....	110
Figure 84: Pushover curves in the negative direction. ....	112
Figure 85: Reaction forces measured in longitudinal walls in the X(-) direction with respect to the displacement of the barycenter of the unit. ....	113
Figure 86: Crack patterns related to the failure of the Fully Connected model in pushovers. ....	115
Figure 87: Crack patterns related to the failure of the Isolated model in pushovers.....	115

Figure 88: Crack patterns related to the failure of the Semi-Connected $m_1$ and $m_3$ models in pushovers.....	116
Figure 89: Crack patterns related to the failure of the Semi-Connected $m_4$ and $m_6$ models in pushovers.....	117
Figure 90: Conventional (a) and real (b) failure of Unit 3 in Semi-Connected $m_6$ .....	118
Figure 91: Disconnection between Unit 2 and 3 in the Semi-Connected $m_6$ Crack pattern. .	119
Figure 92: Conventional (a) and real (b) failure of Unit 1 in Semi-Connected $m_4$ .....	120
Figure 93: Equivalent SDOF and Bilinearized curves for Fully Connected and Isolated cases derived from pushovers in the positive direction. ....	122
Figure 94: Equivalent SDOF and Bilinearized curves for Semi-Connected cases derived from pushovers in the positive direction.....	123
Figure 95: Vulnerability indexes comparison for pushovers in positive direction. ....	124
Figure 96: Equivalent SDOF and Bilinearized curves for Fully-Connected and Isolated cases derived from pushovers in the negative direction. ....	126
Figure 97: Equivalent SDOF and Bilinearized curves for Semi-Connected cases derived from pushovers in the negative direction.....	127
Figure 98: Vulnerability indexes comparison for pushovers in negative direction. ....	128
Figure 99: Non-linear dynamic analysis showing the individual reactions of each unit. ....	130
Figure 100: Nonlinear dynamic analysis results on aggregate building. ....	131
Figure 101: Acceleration record with highlighted point indicating the interruption of dynamic analysis for Isolated units and Semi-Connected $m_1$ case. ....	131
Figure 102: Damage plot from dynamic analysis for Isolated and Semi-Connected $m_1$ models. ....	132
Figure 103: Damage plot from dynamic analysis for Semi-Connected $m_3$ and Semi-Connected $m_4$ models.....	133
Figure 104: Damage plot from dynamic analysis for Fully Connected and Semi-Connected $m_6$ models. ....	133
Figure 105: Pushover curves in the positive direction evaluated for each unit.....	134
Figure 106: Pushover curves in the negative direction evaluated for each unit.....	135
Figure 107: Pushover in $X^+$ for Unit 3, Semi-Connected $m_6$ . ....	136
Figure 108: Vulnerability indexes related to pushovers in positive and negative direction. .	137
Figure 109: Dynamic analysis crack pattern 3D. ....	138
Figure 110: Damage plot resulting from non-linear dynamic analysis.....	139



# List of Tables

Table 1: Properties of the considered mortar types..... 79

Table 2: Elastic material properties..... 81

Table 3: Levels of normal stress applied to different types of mortar. .... 82

Table 4: Friction and cohesion characterization of the mortars. .... 84

Table 5: masonry physical properties calibration from study (74). .... 92

Table 6: Masonry categories according to Tab C8.5.1 of NTC2018 (76). .... 93

Table 7. Wood physical properties..... 94

Table 8: Embedded settings ..... 94

Table 9: Lintel physical properties..... 94

Table 10. User-defined mortar parameters..... 95

Table 11: Dynamic properties of the Fully-Connected aggregate and units modelled as isolated. .... 103

Table 12: Dynamic properties of the Semi-Connected aggregate..... 103

Table 13: First 3 modal shapes of the Fully-Connected aggregate..... 104

Table 14: First 3 modal shapes of the isolated units. .... 104

Table 15: First 3 modal shapes of the Semi-Connected aggregate. .... 105

Table 16: Lateral force distribution in Fully-Connected aggregate. .... 106

Table 17: Lateral force distribution in Isolated units. .... 106

Table 18: Lateral force distribution in Semi-Connected aggregate. .... 106

Table 19: Parameters evaluated for the N2 method from pushovers conducted in the positive direction..... 121

Table 20: Parameters evaluated for the N2 method from pushovers conducted in the negative direction..... 125

# 1. Introduction

An unreinforced masonry aggregate is a type of building characterized by the assembly of multiple structures, referred to as units, that share a certain degree of connection. The aggregate configuration emerges from the gradual addition of new walls and units to existing structures, resulting from the continuous expansion of historic centers over time. Past and recent seismic events in mediterranean countries, such as Italy, have highlighted their vulnerability and the complexity of their structural response resulting from the varied layouts, construction methods, and materials of the units that compose the aggregate (1).

Recent studies have shown how the seismic response of a unit varies when it is considered as part of the aggregate, when compared to its isolated response. This phenomenon is commonly denoted as the "aggregate effect" (2), (3), (4). Accurately modelling the seismic response of these structures is inherently challenging due to various uncertainties, such as the quality of connections between adjacent units, the accumulation of damage over time, connections between floors and walls and the presence of irregularities (5).

The absence of specific guidelines and limited research on aggregates result in oversimplification in the seismic modelling of these buildings, considering units as either separated or rigidly connected (2), (4), (6). As a result, the actual impact of non-rigid connections between units tends to be overlooked, with only a few studies addressing it. A recent example is the experimental shake table test on a half-scale aggregate building (7), where researchers directly investigated the effects of connections between units. The same structure was modelled and studied in (8) by conducting a broad statistical analysis to illustrate the sensitivity of the results concerning the modeling hypotheses of the unit-to-unit interface. The authors in (8) chose to use the equivalent frame model approach, given the numerous analyses performed, and utilized zero-length elements with degrading behavior to simulate a realistic connection between units. They demonstrated that modeling units as isolated can be conservative, but these simplified approaches likely overlook damage and failure modes. However, many variables can influence the vulnerability of the aggregate in specific cases, and further research is needed to establish general guidelines.

Addressing the outlined needs, the present study aims to further explore the "aggregate effect" on individual unit response under varying degrees of interconnection. To do so, an aggregate building composed of three similar three-story units was designed and modelled using a 3D

Finite Element method. This method considers simultaneously in-plane and out-of-plane mechanisms and their interaction, unlike the equivalent frame method. A homogenized approach was utilized to model masonry walls, considering 2D layered shell finite elements. Three types of models were developed: one with rigid connections, referred to as “Fully-Connected”; a single model for each unit, referred to as “Isolated”; and a third with an intermediate degree of connection, referred to as the “Semi-Connected” condition, achieved by adding a layer of degrading mortar between units. In the Semi-Connected model, a parametric study of the mortar was performed, investigating four different types of mortar to evaluate the impact of connection strength variation between units. The mortars associated with interface layers were characterized based on cohesion-friction failure criteria.

The analysis for each model involved modal analysis to dynamically characterize the structure and assess its fundamental modal shape. This shape was then utilized to define the lateral force distribution in nonlinear static analyses, which were conducted in both the positive and negative longitudinal directions of the buildings. Seismic vulnerability was assessed based on pushover results using the N2 method (6). Subsequently, the results were compared with a nonlinear dynamic analysis, which considered the L’Aquila earthquake as the seismic input.

The analyses were carried out using STKO (Scientific ToolKit for OpenSees) (9), a framework for OpenSees (10) which, in addition to providing an interface, allows the use of advanced built-in materials and elements.

## 2. Seismic behaviour of unreinforced masonry aggregate buildings

Masonry buildings in aggregate configuration constitute a significant part of the existing architectural heritage in historic centers, typical throughout Europe (Figure 1). These constructions are the result of multiple expansion and elevation operations carried out over the centuries without a specific urban development plan to meet the demanding housing needs of the past. Masonry aggregates appear as a series of contiguous buildings, more or less effectively connected, often designed solely to withstand vertical loads, without any adherence to seismic design criteria.



*Figure 1: Masonry aggregate building, Treviso, Italy.*

The seismic vulnerability assessment of aggregate masonry buildings is a subject of significant interest and relevance, especially considering the serious economic and social consequences that have emerged following earthquakes affecting such constructions in past decades (6). Various portions of these aggregates were constructed during different periods, resulting in typological differences in the materials used. These differences are influenced by the availability of resources near the respective building sites, the construction techniques utilized, the plan-altimetric organization, and historical period.

## **2.1 The current state of the art of unreinforced masonry aggregates**

The current Italian regulation, NTC18 (11), lacks a well-defined calculation method to predict the specific behaviour of aggregate masonry buildings as a whole under seismic actions. Instead, it allows for the direct analysis of the individual structural units (US) that compose the aggregate, while also considering potential interferences with contiguous units. A structural unit denotes a portion of the aggregate that maintains continuity in both elevation and plan, characterized by a common construction process and delimited by open spaces or structurally contiguous buildings, which are at least typologically different. It is essential for these structural units to ensure the distribution of vertical loads from the upper floors to the foundation.

Specifically for masonry aggregate buildings, NTC18 suggests for two different analysis procedures based on the rigidity of floors. In the case of flexible floors, each wall of the unit could be studied separately, considering the respective vertical loads and seismic action only in the direction parallel to the wall. If there is a good connection between walls of contiguous units, it is at the discretion of the designer to assess an increase in seismic action. In the case of rigid floors, a nonlinear static analysis can be carried out on the individual unit, separately verifying each inter-story level.

In addition to studying the US as isolated, NTC18 (11) requires the consideration of the effects of unbalanced forces on the walls of adjacent structural units, such as the thrust of arches, vaults, or domes that are not absorbed by appropriate resistant elements. It is also necessary to verify the degree of connection between orthogonal walls, between adjacent units, and between floors and vertical walls. However, explicit guidelines on how to address these aspects are not provided in the code.

An essential phase in the study of masonry aggregates is the survey and identification of individual units within the aggregate. This phase is described in the ReLUIIS project (12). Reconstructing the history of the building and aggregation process, as well as the subsequent modifications over time, is crucial for correctly identifying the structural system. This approach not only holds historical validity but also has structural significance. For example, understanding which portion of the aggregate was built later in relation to others is for assessing the vulnerability of the single unit. In Figure 2, a sketch exemplifies this aspect, showing that

the new construction (C) was inserted between two existing buildings (A), utilizing the existing lateral walls and constructing only the front and back walls. Without appropriate anchoring to the existing walls, the vulnerability of the added walls is significantly high.



Figure 2: Growth mechanism of aggregates (12).

In ReLUIIS, the concept of the minimum intervention unit is introduced, which is the portion of an aggregate, consisting of one or more structural units, that if retrofitted allows the reduction of seismic vulnerability, not only for the individual unit but also for adjacent ones. This is considered crucial because a localized intervention aimed solely at improving the seismic performance of one structure could potentially worsen the vulnerability of other units within the aggregate (13).

Due to the many issues highlighted and the lack of precise guidelines, the seismic assessment of masonry aggregates is complex. Several assessment methods have been widely discussed in the literature, with the most relevant including empirical methods, heuristic methods, and analytical/mechanical methods (6). Empirical methods rely on historical data and observations from past earthquakes to assess the seismic vulnerability of masonry structures. Buildings are grouped into vulnerability classes through statistical analyses based on damage. By solely considering the building's location, its seismic assessment can be evaluated. This approach enables rapid assessment and categorization of many buildings in a short amount of time. Heuristic approaches estimate vulnerability factors primarily based on expert judgment, considering factors such as hazard and exposure of the site, along with on-site inspections by experts. The classification involves evaluating different damage grades and comparing various building types. Analytical/mechanical methods require the construction of a numerical model to investigate the behaviour of structures through simulations. Generating such models necessitates a deep understanding of the building's geometry and material properties. This process is time-consuming and can only be carried out for a limited number of buildings (14).

In addition, hybrid solutions combine the three mentioned methods, generating a multi-scale approach.

## 2.2 Behaviour of the masonry

Masonry is a composite material composed of assembled stone elements, typically connected through mortar joints. Dry masonry refers to the construction method where mortar is not used to bond the blocks. Masonry can be constructed using a wide range of materials, each of which gives unique characteristics to the structure (Figure 3). The masonry is defined as regular or irregular depending on whether it is or not the product of the repetition of a single representative volume element (RVE).



*Figure 3: Example of masonry on existing buildings.*

Masonry exhibits a distinctly nonlinear behaviour even under low tensile states, due to its inherent inability to resist tensile forces (15). When a force is applied to a masonry structure, only the compressed portions can provide a reaction, while the zones in tension can easily fracture or crack. This nonlinear behaviour implies continuous damage and a reduction in the effective resistance area as the force increases, highlighting the nonlinear response of the structure (Figure 4). The post-elastic behaviour of masonry introduces a level of complexity because it exhibits softening strength degradation with increasing deformations. Masonry fails suddenly and catastrophically once a crack initiates and propagates. This degradation makes masonry a quasi-brittle material, which is complex to numerically define and calibrate when studying this material using numerical method. This softening branch is characterized by a low tensile fracture energy: the amount of energy required to propagate a crack in the material or, in simple terms, the area under the stress-strain curve. The calibration of this property in models is a crucial step because it allows for the correct consideration of the material's brittleness and

the prediction of crack propagation through masonry structures under various loading conditions.

Masonry's mechanical behaviour has significant range of variation in mechanical properties, deriving from the heterogeneity in terms of mechanical behaviour and geometry of the materials involved. Understanding this behaviour requires careful modelling strategies and the correct selection of a constitutive model for the material. Masonry can be mechanically studied through experimental tests conducted on-site or in the laboratory (16).

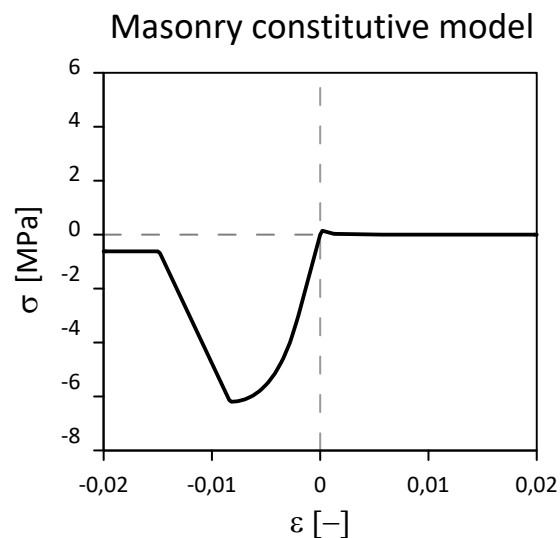


Figure 4: Masonry constitute model.

The macroscopic behaviour of masonry is determined by the properties of its constituent materials and their interaction. The properties of brick parameters can be accurately assessed through laboratory tests. Conversely, evaluating mortar properties is challenging, and the results often exhibit significant dispersion (17). On-site tests can compromise the properties of the mortar and it is complex to extract undisturbed specimens for laboratory testing.

## 2.3 Global and local failure mechanisms of URMs

The classification of response mechanisms in unreinforced masonry buildings can be conducted between mechanisms of the first and second modes, as defined by Antonio Giuffrè (18). The mechanisms of the first (or local) mode concern the movements associated with the behaviour of masonry walls outside their plane. In such cases, walls are considered to be rigid bodies, and through equilibrium conditions (rotation or sliding), the mechanisms can be assessed.



Secondary mechanisms (or global) are named as such because they are activated only when local mechanisms do not occur.

In global analyses, it is assumed that all elements composing the structure contribute to the building's resistance. In such analyses, the strengths of walls in-plane are considered, assuming a rigid connection between orthogonal walls, even though, in reality, the building may exhibit a different degree of connection. The in-plane mechanism can be associated with three main categories of crack patterns: shear cracking, sliding, and rocking failure (Figure 5). In the case of shear cracking, cracks propagate diagonally along the mortar interface or pass through bricks, depending on the relative resistance between the masonry components. In situations of low vertical compression or very low mortar cohesion and friction properties, a horizontal mortar layer can fail, creating a sliding plane. Vertical eccentric loading and shear can cause collapse due to tension developed at one corner and/or crushing at the other corner (rocking failure) (19).

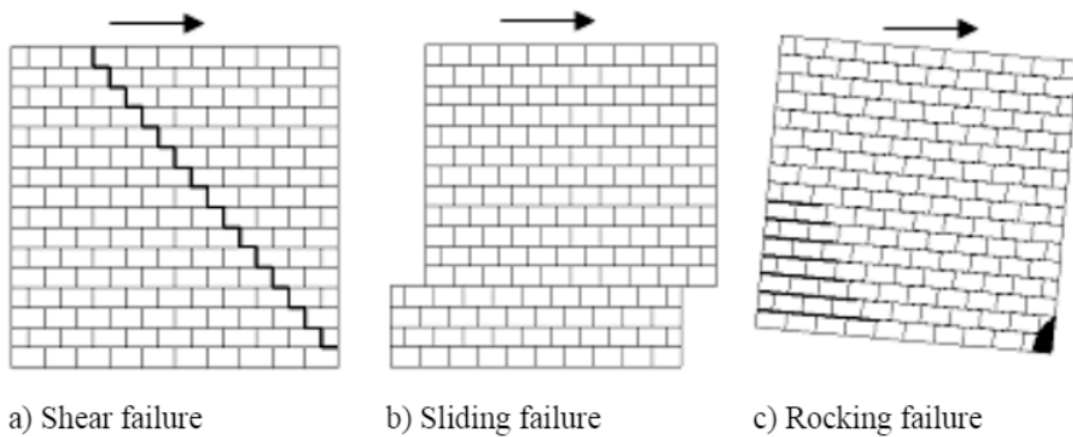


*Figure 5: In-plane failure mechanisms of masonry walls (20).*

Nonlinear static analysis is a commonly used for conducting global analysis of unreinforced masonry buildings. However, without local verifications, this method may overestimate the building's strength (1). The validity of global analysis relies on ensuring the box-like behaviour of the analysed building. An illustrative example is provided in the Figure 6, depicting a masonry structure consisting of four walls. In global analysis, the distribution of seismic action depends on the stiffness of the elements. However, in reality, the low degree of connection between orthogonal walls can significantly alter the distribution of forces among them, activating a local mechanism.

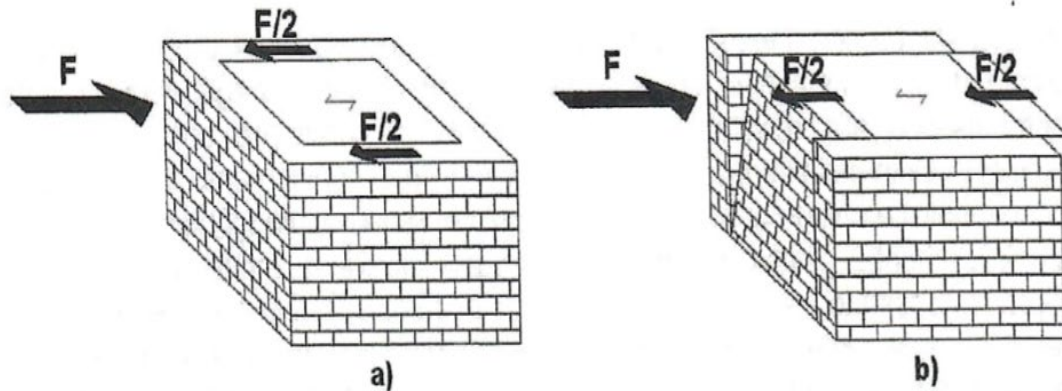


Figure 6: (a) walls rigidly connected; (b) walls not connected (21).

To analyse the structure properly, it is necessary to combine global analysis with the analysis of local mechanisms. In such analysis, factors such as the quality of connections between walls and between walls and floors, the presence of concrete curbs and chains, and the existence of thrust elements are considered. In assessing local mechanisms, it is important to consider the presence of poor-quality masonry that could lead to disintegration and compromise the monolithic nature of the structure. Additionally, the presence of a flexible floor diminishes the box-like effect of the structure, amplifying the significance of local mechanisms.

Below are described the main local mechanisms (21):

- The overturning mechanism causes a wall to rotate around its base due to the absence of proper wall-to-wall connection. It can be schematized as a wall free to rotate around a cylindrical hinge placed at the base. This mechanism can occur at various levels of the structure and involve one or more walls. The detachment of orthogonal walls can occur due to flexural (Figure 7a) or shear (Figure 7b) failure. In cases of good connection between walls, the presence of openings could facilitate crack development and lead to a portion of the wall tilting (Figure 7c). This mechanism can be mitigated by introducing metal ties.

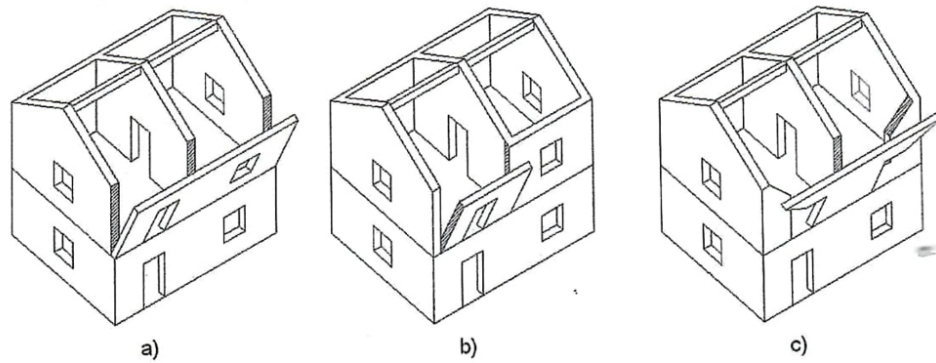


Figure 7: Overturning mechanisms (21).

- The vertical flexural mechanism generates a central cylindrical hinge, dividing the wall into two blocks that rotate at the two extremities, behaving like hinges. It can be caused by the presence of concrete curb at the base and at the roof level due to the thrust of poorly connected intermediate floors (Figure 8a), or by the rigid connection of a wall between two floor slabs and the presence of slender walls susceptible to out-of-plane flexural deformation (Figure 8b).

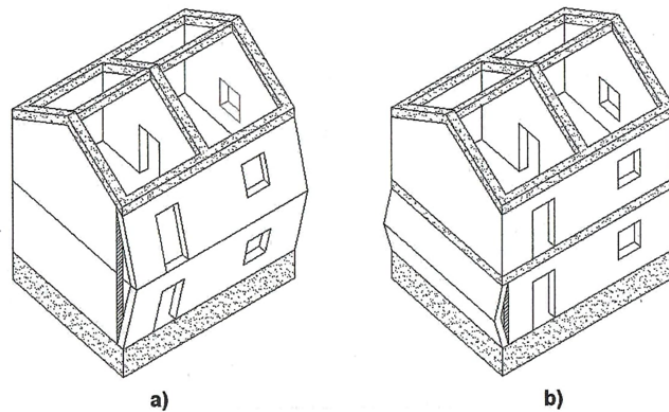


Figure 8: Vertical flexural mechanisms (21).

- The horizontal flexural mechanism occurs when the orthogonal walls are well connected, but the facade isn't well connected at the top (Figure 9). The roof system tends to push, causing a portion of the wall to rotate around oblique cylindrical hinges.

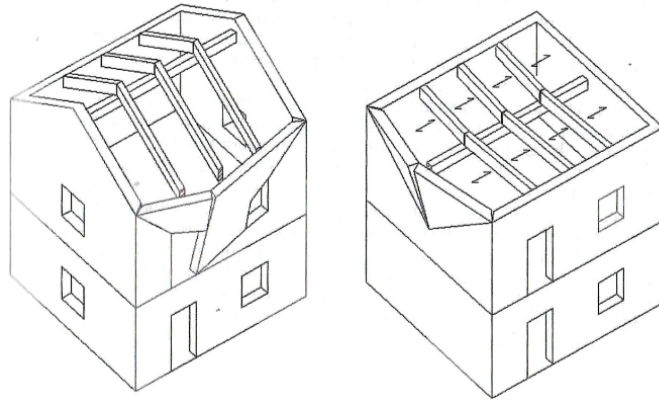


Figure 9: Horizontal flexural mechanisms (21).

- The composed overturning mechanism occurs when various local mechanisms happen simultaneously (Figure 10). It is typical when the connection between walls is strong, but the orthogonal walls are weak and prone to cracking. The openings in transversal walls become favourable points of detachment.

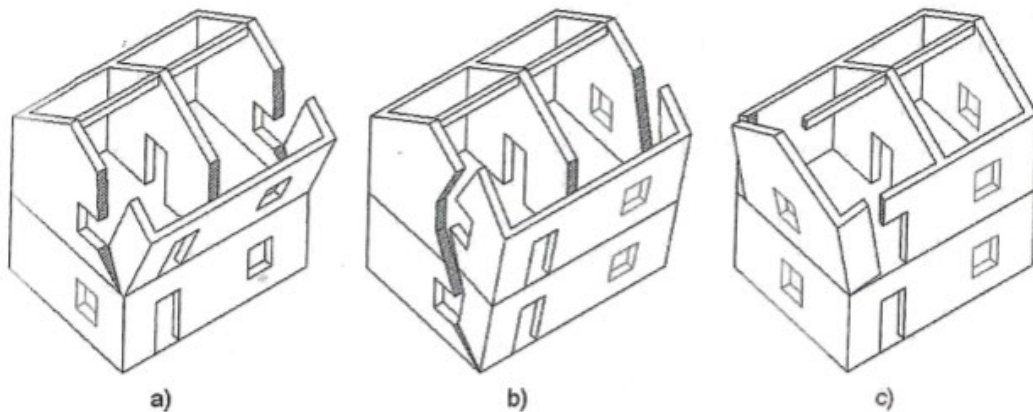


Figure 10: Composed overturning mechanisms (21).

## 2.4 The “aggregate effect”

A masonry building exhibits a different response to seismic loading when it is isolated compared to when it is part of an aggregate. The term "aggregate effect" refers to the variation in the structural behaviour of an unreinforced masonry structure caused by the presence of adjacent units (15). While numerous studies are available regarding the analysis and modelling of single unreinforced masonry buildings, limited documentation exists for aggregates. This

limitation arises from uncertainties associated with numerical model construction and the complexity of testing large-scale buildings. (7).

In the past, there was a prevailing notion that connecting different buildings would enhance their performance. However, this assumption is no longer universally accepted. In some cases, the seismic vulnerability of a unit in an aggregate building may exceed that of a freestanding one. There are studies have shown that considering a unit as part of aggregate or isolated can lead both conservative and unconservative estimates, depending on factors such as the position of each unit in the aggregate and geometrical properties of neighbouring units (13). For instance, in (22) an assessment procedure was developed that could assign also negative scores to units within aggregates, making them more vulnerable compared to the same buildings assumed to be isolated. Factors considered in this discrimination include the presence of adjacent buildings of different heights, position within the aggregate, presence of staggered floors, typological differences between units, and variations in the distribution of openings.

Observations have shown that the most vulnerable buildings are often sandwiched between shorter buildings or positioned at the corner or end of the aggregate. Units situated at the edges of aggregates generally exhibit higher vulnerability, as their displacement is not constrained by adjacent units, and they are subject to torsional effects generated by seismic action on the entire aggregate (4).

An isolated unreinforced masonry unit has a similar seismic response in the transverse or longitudinal direction, but this can change when it is part of an aggregate. In cases of aggregate buildings with a predominant direction (e.g., for row aggregates), the aggregate effect primarily influences the main direction, while its effect in the transverse direction can be disregarded (15). It makes the seismic response of the building different according to the action direction.

Two fundamental aspects that can modify the aggregate effect on individual units are the type and arrangement of floors within units and the degree of inter-unit connection. The rigidity of floors plays a crucial role in distributing loads between longitudinal walls, while the degree of inter-unit connection regulates the interference between units. These aspects are described in more detail in the following paragraphs.

## 2.4.1 Impact of different floor typologies

One of the peculiar characteristics of building aggregates is the staggered levels of floor slabs between contiguous building units, which, together with issues of poor or inadequate connections between units, can cause local collapse mechanisms. Another relevant factor to consider in masonry building modelling is the stiffness of floors and the degree of connection between walls and floors. The presence of rigid or flexible floors significantly affects the distribution of inertial forces during earthquakes (23).

According to NTC 18 (11), in the case of a concrete slab with a thickness of at least 40 mm, it is possible to assume the floor as infinitely rigid (Figure 11a). Therefore, the slab is considered to have only three degrees of freedom: two perpendicular in-plane displacements and in-plane rotation. However, when the slab is made of wood, it exhibits a finite stiffness and can deform even out of its plane (Figure 11b).

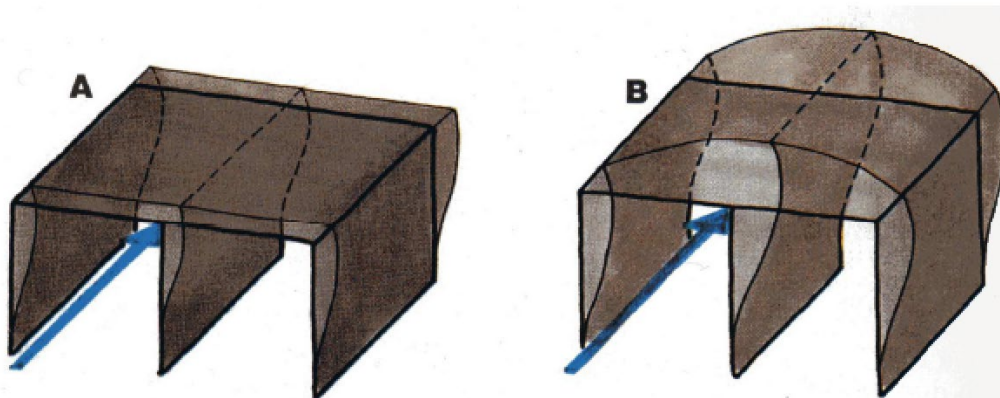


Figure 11: (a) stiff diaphragm; (b) rigid diaphragm (24).

In the case of an infinitely rigid diaphragm (Figure 12a), inertial forces are distributed to walls proportionally to their relative stiffness. To analytically evaluate the portion of inertial force taken by each wall, the slab can be represented as a beam supported by walls acting as springs with specific stiffness. The beam is assumed to be infinitely rigid, capable of translating and rotating in its plane without deformation. The inertial force can be concentrated at the mass centroid of each floor, while the resultant response of the structure is applied to the stiffness centroid. The eccentricity between the mass and stiffness centroids generates secondary effects that increase the demand.

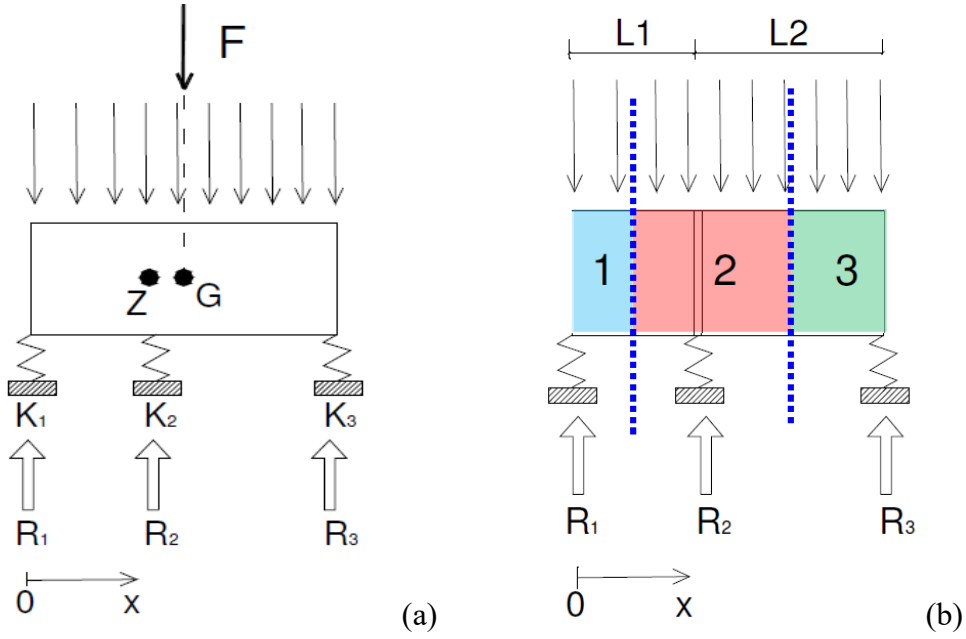


Figure 12 (a) Rigid diaphragm; (b) Flexible diaphragm.

The position of the floor barycentre is:

$$x_z = \frac{\sum_{j=1}^n k_j x_j}{\sum_{j=1}^n k_j} \quad [1]$$

The reaction of each spring can be evaluated as:

$$R_i = F \frac{k_i}{\sum_{j=1}^n k_j} + F K_i \frac{(x_i - x_z)(x_G - x_z)}{\sum k_i (x_i - x_z)^2} \quad [2]$$

Where the first term takes into consideration the translation effect, while the second term is related to rotation. In cases where the mass and the stiffness centroids coincide, the second term of equation [2] is null.

In the case of flexible floor (Figure 12b), the inertial forces are distributed among transverse walls according to the masses applied on each floor. The mass corresponding to each wall can be evaluated using the tributary area method. The reaction force of each wall in Figure 12b is:

$$R_1 = \frac{R}{L_1 + L_2} \frac{L_1}{2} \quad [3]$$

$$R_1 = \frac{R}{L_1 + L_2} \frac{L_1 + L_2}{2} \quad [4]$$

$$R_1 = \frac{R}{L_1 + L_2} \frac{L_2}{2} \quad [5]$$

## 2.4.2 Impact of Degrees of Interconnection Between Units

In historical centres, masonry aggregate buildings often result from the assembly of structures built in different periods without consistent planning. New units constructed near existing ones were typically connected using weak interlocking joints or mortar. During seismic events, the mortar interfaces are particularly vulnerable, and adjacent units can interact, causing high stress generated by units hammering against each other. Past experience has shown that interfaces between units play a crucial role in concentrating damage and activating failure mechanisms (2). Figure 13 illustrates an example of the cracks that occur at the interface between units due to a seismic event.



*Figure 13: Details of the damage occurred between structural units (2).*

The definition of the interconnection between adjacent units adds uncertainty to the assessment of unreinforced masonry aggregates. Due to limited information about the interaction of adjacent units in literature, there are no established guidelines on this topic (25). Recognizing this gap, a joint research program named “SERA AIMS-Adjacent Interacting Masonry Structures” (7) was initiated to investigate the impact of connections between units in masonry aggregates.

Shake table testing was conducted in the National Laboratory for Civil Engineering (LNEC) on a half-scale masonry aggregate building consisting of two units: one single-storey unit (Unit 1)



and one two-storey unit (Unit 2) (Figure 14). To replicate real construction sequences in city centres and prevent interlocking between units, unit 2 was constructed before the other. Unit 2 was composed of four walls, while Unit 1 had a C-shape configuration. The interconnection between the units was established using only a mortar layer, facilitating detachment during the test (Figure 15).

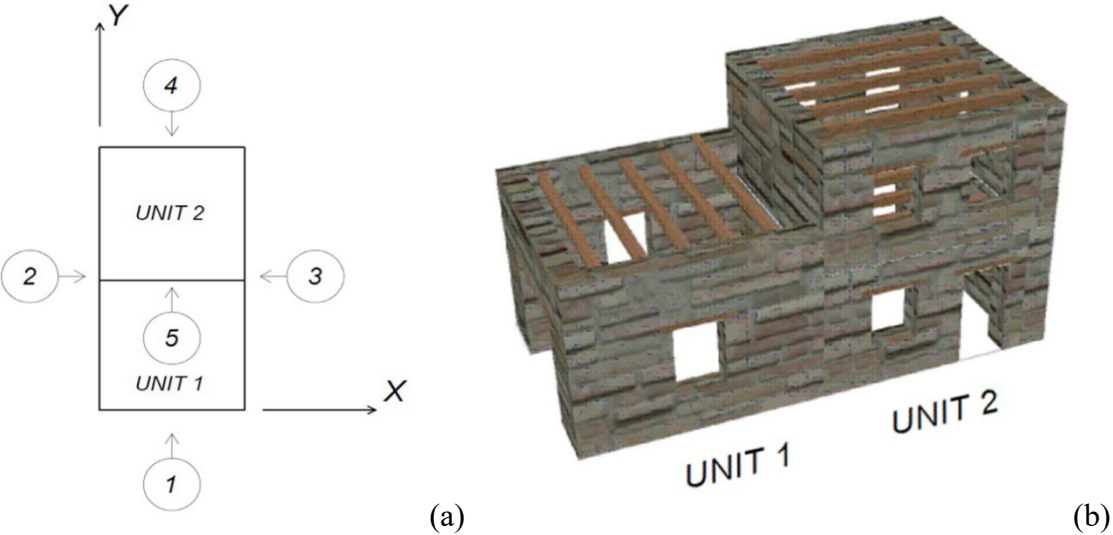


Figure 14: Plan view (a) and model (b) of masonry aggregate tested in (7).



Figure 15: Interface between units in the masonry aggregate (7).

The seismic excitation was applied in both the x and y directions. The masonry aggregate exhibited cracking and separation at the interface, both longitudinally and transversally. During the more intense cycles, the adjacent walls of the two units pounded against each other, leading to the formation of a soft-story mechanism at the second floor of Unit 2. The experimental results, regarding both structural response and crack pattern, could only be accurately replicated through numerical simulation if the connection between units is explicitly modeled.

Current approaches to dealing with masonry aggregates consider units as either fully connected or completely isolated from each other. However, assuming aggregates as perfectly connected fails to account for the reduction in strength and stiffness caused by weak interfaces (8), while considering them as isolated cannot properly capture the "aggregate effect." In (22), a row masonry aggregate was examined, revealing that modeling units as separated could lead to either an overestimation or underestimation of its seismic vulnerability. This discrepancy depends on the position of each unit within the aggregate. Specifically, units positioned at the extremities of the aggregate experience higher deformation and stress compared to intermediate units.

The objective of this research is to explore the investigation of the degree of connection between individual masonry units and their influence. Using numerical models, units will be examined as isolated, fully connected within the aggregate, and considering intermediate levels of connection between units, referred to as "semi connected," which are more representative of real-world scenarios. The goal is to evaluate how the "aggregate effect" can be influenced by the strength of the unit-to-unit connection. Furthermore, it is of interest to assess the reliability of conventional assessment methods in all cases.

### **3. Numerical modelling of masonry structures**

For centuries, masonry was the primary construction material before the era of concrete and steel. The design of masonry structures, from their origins until the late 19th century, based on the adherence to construction rules established over millennia of empirical experiences and observations. When the scientific community began studying the tension and deformation in structures, they realized that the theory of elasticity was insufficient for analyzing structures made of heterogeneous, anisotropic composite materials with nonlinear behavior and lacking tensile strength, such as masonry. The fundamental distinction between steel or concrete buildings and masonry buildings lies in their structural modeling approach. Steel or concrete buildings can typically be modeled as beam systems, whereas masonry buildings are more accurately represented as panel systems. In frames, only the bending behavior of the resistant elements needs to be considered, while for masonry panels, both the bending and shear behavior must be taken into account.

Considering modern computational capabilities, the Finite Element Method (FEM) and the Discrete Element Method (DEM) are the main model methods adopted for masonry structures analysis. Currently, the masonry modeling methods include micro-modeling, the homogenized masonry approach, and the equivalent frame method (26). The following discussion will go into the features of each of these models.

#### **3.1 FEM and DEM**

From a numerical perspective, the crucial feature of masonry is its composite nature: it is composed of stones jointed by mortar layers. Such materials can be effectively modelled using discrete element methods (DEM) or finite element methods (FEM). Discrete element models explicitly represent masonry units and joints. In the research (27), Lemos defines the DE models as numerical models which study structures as assemblies of distinct blocks (or particles) interacting along their boundaries. These models are particularly useful for assessing the behavior of structures that can be segmented into separate bodies, such as stone blocks in masonry buildings.

Discrete element models offer flexibility in representing elements with different geometries, which can be modeled as either infinitely rigid or deformable according to specific stress-strain

relationships. Each element can move independently, and the contact behavior can evolve during the analysis as deformation progresses. Mortar joints are represented as contact surfaces between the units, simulated using a set of contact points. Defined relationships govern how forces are transmitted between these points based on their relative displacements.

Discrete Element Models are particularly suited for examining failure mechanisms in masonry structures. The method allows the consideration of problem in which units are subjected to large displacements and correctly models the strong nonlinear behavior of masonry structure, also including the case of full separation between blocks. Its main drawback is that an accurate modelling of the interfaces requires many contact points, which increase the computational demand. (28)

An alternative solution is the Finite element modelling (FEM) which describes the structure as a mosaic of continuous elements connected at the edges, with nodal displacements as unknowns. Each element has its own material properties, from which relationships between nodal forces and displacements can be derived. The elements are assembled and connected to each other by nodes. By considering the external nodes and boundary conditions, the equilibrium of the structure can be described by a system of equations, the solution of which provides the nodal displacements. From the nodal displacements, the stress and the strain can be evaluated for the integration points. In (26), Lourenço explains that the FEM can be applied through three primary modeling strategies in masonry structures: detailed micro-modeling; (b) simplified micro-modeling; (c) macro-modeling.

Additionally, hybrid solutions combining FEM and DEM exist. An example involves employing the DEM to analyze masonry as distinct elements, each subdivided into finite elements according to the FEM. These elements can deform using defined functions and strain parameters. An illustrative application of this approach is presented in (20), where Pepe conducted a study on three masonry panels with different height-to-length ratios. The walls were modeled using DEM and a combination of DEM/FEM. Each panel was subjected to increasing horizontal forces until failure occurred. Figure 16 illustrates the sliding mechanism failure observed in the masonry wall with an H/L ratio of less than 1.

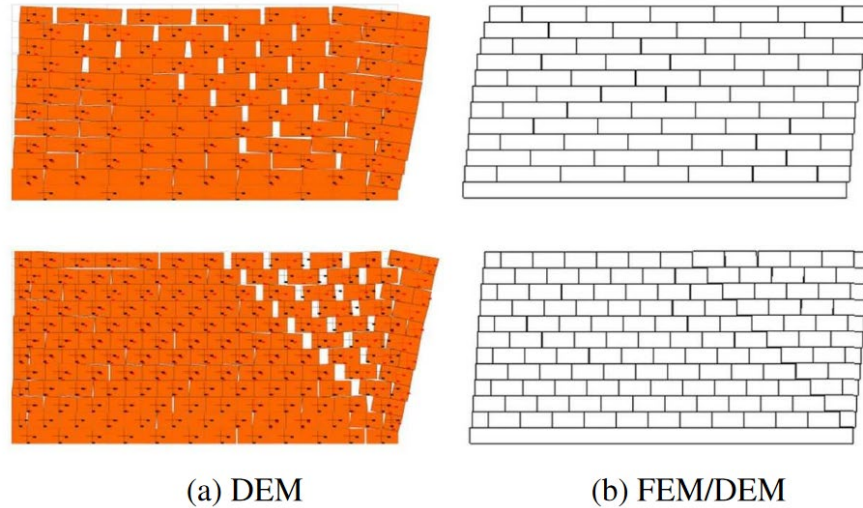


Figure 16: Collapse mechanism obtained using DEM (a) and FEM/DEM (b) (20).

### 3.2 Equivalent Frame Modelling

One of the most used techniques for schematizing masonry walls is the Equivalent Frame Modelling (EFM). This approach involves breaking down walls into a set of one-dimensional elements. According to the schematization of the equivalent frame, each wall is made up of three macro elements: piers, spandrels, and the rigid nodes. The masonry piers are the deformable vertical elements placed between two openings belonging to the same level of the building, while the spandrels are the deformable horizontal elements placed between two openings belonging to different levels. The rigid nodes are the elements that connect the piers and spandrels. In this model, 1D elements can be treated as beams, while nodes can be represented as rigid connections.

The deformations in the structure are influenced by the height and width of openings. According to the Italian rule code NTC 18(11), a method for determining the height of the masonry piers in the equivalent frame is proposed by Dolce (29) (Figure 17c), which is commonly used in practice. This method allows the computation of the flexible length of the element ( $H_{eff}$ ) based on the inter-storey height ( $D$ ) and the dimensions of openings. The definition of  $H_{eff}$  is provided by the following equation:

$$H_{eff} = h' + \frac{1}{3} D \frac{H - h'}{H'} \quad [6]$$

In the Equivalent Frame Method applied to masonry buildings, the approach assumes that nonlinear behaviour occurs primarily within the columns and spandrels. In contrast, other parts of the structure are simplified as rigid nodes, representing areas where significant deformations are not expected to occur. These assumptions align with the observed damage patterns in unreinforced masonry buildings subjected to seismic forces (30). Typically, cracks tend to concentrate in the masonry elements situated between openings, both vertically and horizontally.

In research there are examples of use of equivalent frame modelling used to approach complex subjects, such as the “aggregate effect”. Angiolilli in (2) studied the different response of a building considered as isolated or as part of an aggregate building. In the study, two existing aggregates have been modelled, one settled in Catania and one in Visso using 3D equivalent frame model. The buildings were analysed by performing non-linear static analysis and non-linear dynamic analyses. To also take local mechanisms into account, an integrated process based on floor accelerations obtained from post-processing data was used.

Equivalent frame modelling is widely used in the profession for building modelling and analysis due to lower requirements on time and computational resources. However, despite its widespread use, several limitations constrain the effectiveness of such methods. Current building regulations do not provide a comprehensive approach to precisely defining the equivalent frame in all situations, for instance, accounting for irregularities and uncertainties in existing structures. The presence of non-vertical walls or existing cracking pattern are neglected, even though they significantly influence the definition of the deformable parts inside the frame (31). Geometric relationships between pillars and beams may not conform to the frame model, or any damage could drastically alter the behaviour of the structure, yet these factors are disregarded. Another limitation of this technique is its failure to consider the transfer of tangential stress between piers and spandrels. Overlooking this aspect neglects a significant source of strength and structural integrity of masonry. Furthermore, the method primarily focuses on in-plane failures, while out-of-plane mechanisms must be verified separately using specific approaches. Local and global mechanisms can be effectively decoupled only in case of regular buildings with aligned openings (32). In case of irregular buildings, out-of-plane mechanism influence local failures and their interference should be considered.

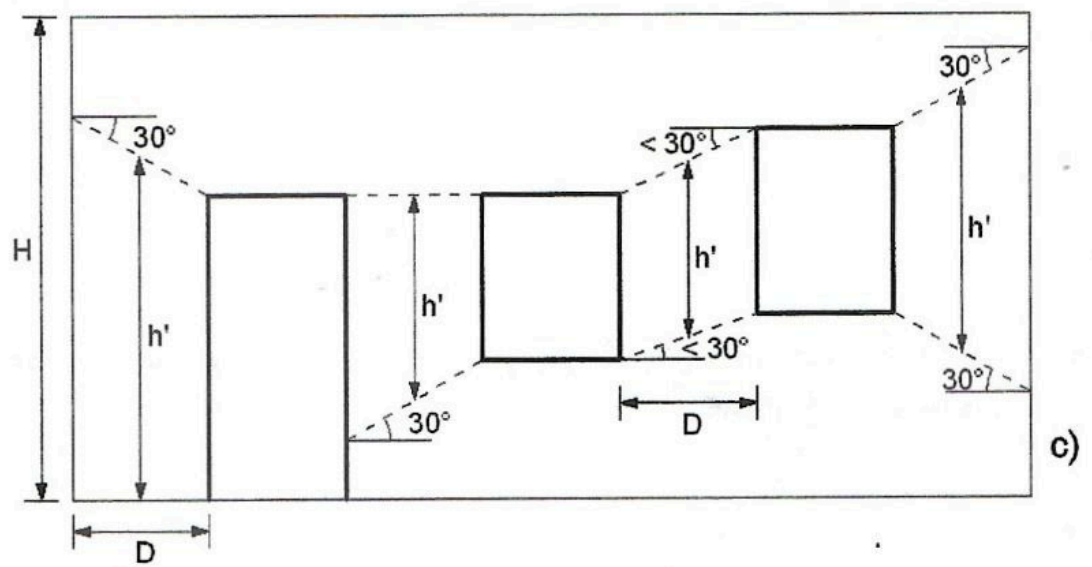
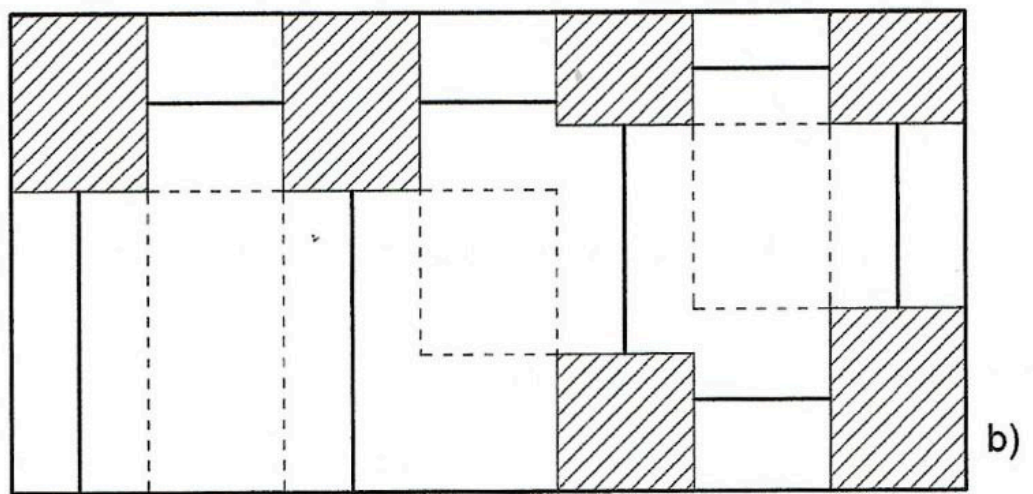
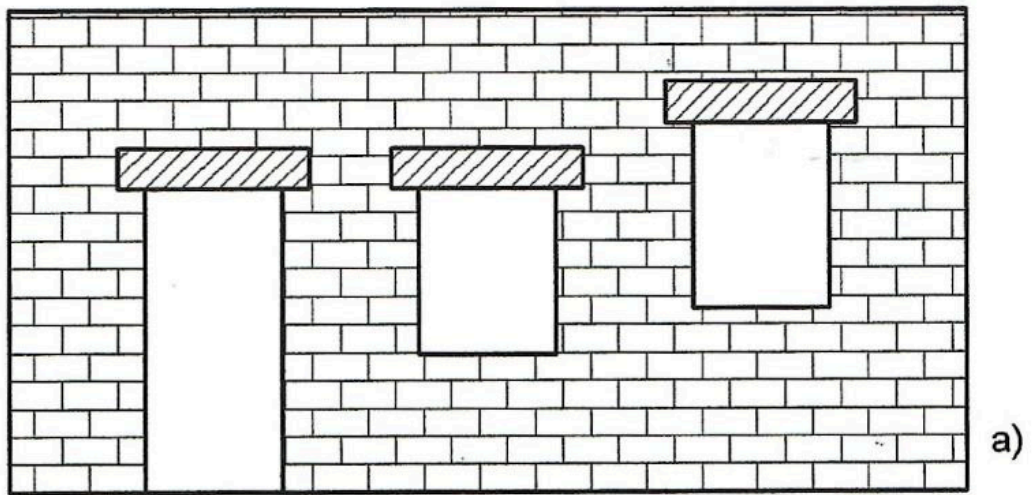


Figure 17: (a) Wall geometry; (b) schematization with infinitely rigid nodes; (c) schematization of Dolce (21).

There are examples in the literature on how to identify an appropriate equivalent frame model for masonry walls that can provide a realistic response even in the presence of irregularities (33). The complexity of the existing building makes it impossible to define the model processing in a universal way. It is of fundamental importance that any irregularities are assessed on a case-by-case basis based on the specificity of the existing building and the validity of the proposed FE model must be checked.

The research is enhancing the technique of the equivalent frame model, and some of the previously described issues are being mitigated. Vanin and Penna in (34) developed an equivalent frame model of a masonry building, which was tested on a shaking table in EUCENTRE, Pavia (Italy) (8). The building under study is a half-scale replica of a real aggregate located in Basel, Switzerland, as showed in Figure 18. The authors realized a three-dimensional equivalent frame model capable of assessing both in-plane and out-of-plane failures (Figure 19). This functionality was achieved through the utilization of a macroelement formulated in OpenSees by Vanin (35) which represents both spandrels and piers within the equivalent frame model. One significant advancement provided by this new tool is its ability to overcome the assumption of perfect connection between orthogonal walls. This modeling technique can be extended to existing historical buildings characterized by poorly connected orthogonal walls, making them vulnerable to local mechanisms.



Figure 18: (a) Example aggregate in Basel (Switzerland); (b) Laboratory tested masonry aggregate (8).



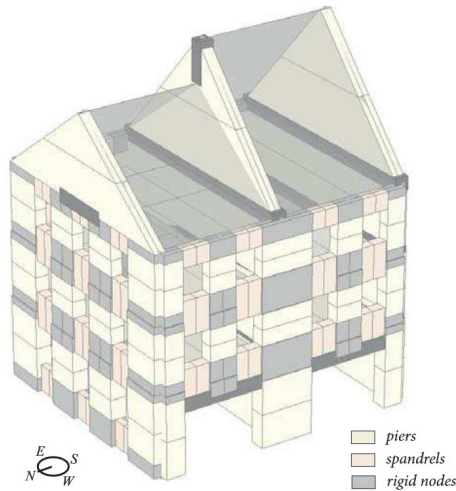


Figure 19: EFM of the aggregate building (34).

### 3.3 Micro-modelling

Micro-modelling exactly replicates the actual geometry of masonry, distinguishing between stone elements and mortar joints, that can be modelled using continuous materials with different mechanical behaviours (36). This type of modelling can be executed in a detailed or simplified manner. In the former case, the mortar-stone unit interaction can be directly considered by modelling the mortar joints with or without interface surfaces (Figure 20a). In the latter case, the interface is indirectly modelled by extending the stone elements to the midline of the mortar joints and introducing interface surfaces to which constitutive relationships are assigned (28) (Figure 20b).

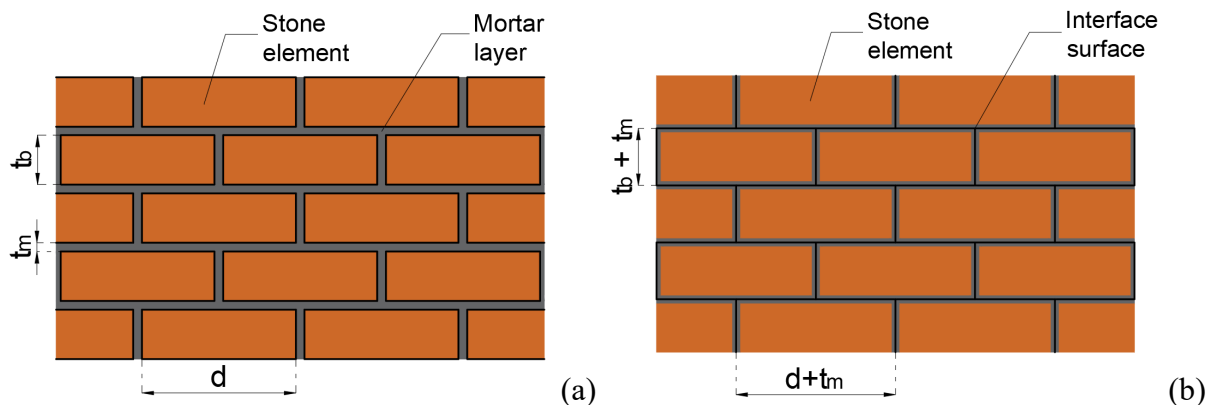


Figure 20: a) Detailed micro-modelling; b) simplified micro-modelling.

Appropriate resistance criteria must be associated depending on the modelling approach used. A micro-modelling strategy for masonry may involve assuming indefinite linear elastic

behaviour for stone elements and concentrating nonlinearity in mortar joints and interface surfaces. This necessitates considering all possible types of masonry failure through interface surfaces, introducing a discontinuity in the displacement field. The concept of finite interface elements in masonry construction was first introduced by Page in 1978 (37), and more recently, Lourenco and Rotz (36) proposed a simplified micro-modelling approach based on nonlinear finite interface elements capable of describing both the mechanical behaviour of mortar joints and penetration failure in the mid-section of generic stone elements. It is important for the numerical model to accurately represent the various failure mechanisms in masonry structures. In Figure 21, the five main failure mechanisms of masonry are showed: (a) and (b) are related to mortar, (c) to stones, while (d) and (e) are a combination of the previous failure mechanisms.

Micro-modelling techniques lead to the development of discontinuous models that, while providing more realistic results, also significantly increase computational request compared to continuous models (38). This is due to the need for a refined mesh to accurately represent small elements such as mortar layers. Analysing damage development and strength degradation requires the use of robust integration algorithms to ensure convergence. Highly sophisticated micro-modelling approaches are generally employed for simulating experimental tests or for scientific applications on structures of particular importance. In such cases, the necessary analyses involve a considerable computational load.

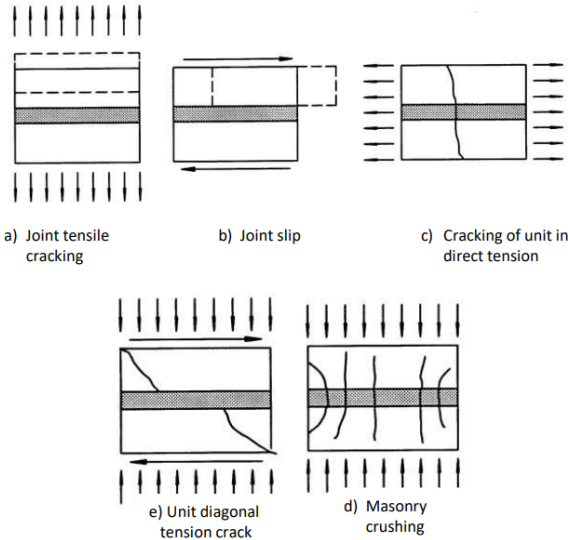


Figure 21: Failure mechanisms of masonry (16).

To assess the accuracy of micro-modeling results in relation to reality, a significant example by Petracca in (39) is noteworthy, as it involves a comparison of model outcomes with experimental data. This case was specifically chosen for its implementation in STKO,

contributing to increased confidence in the software's efficacy. Petracca replicated a masonry building experiment under static cyclic conditions based on (40)<sub>2</sub>, utilizing micro-modeling to show the complex failure mechanism. In the study both units and mortar joints have been modelled as continuum elements. An advanced damage model was implemented to reproduce the nonlinear behavior of masonry. As illustrated in the Figure 22, a distinctly favorable correspondence between the model and experimental results is apparent. The analysis was also very efficient from a numerical point of view thanks to a new constitutive model based on continuous damage in combination with the implicit-explicit mixed integration algorithm, explained in the chapter relating to OpenSees. The case study mesh has 177,000 elements, 60,000 nodes (6 DOFs per node), totalling 360,000 equations. Analysed with OpenSeesMP on a high-performance computer, the computation-heavy model was processed in under 3 hours, partitioned into 24 sub-domains.

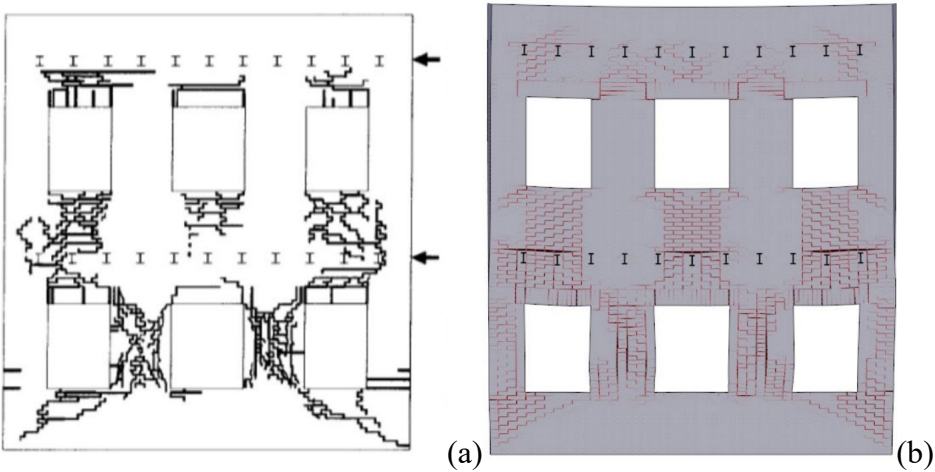


Figure 22: (a) Experimentally obtained Crack pattern (b) Model results Crack pattern (41).

### 3.4 Macro-modelling: homogenized masonry approach

Macro-modelling enables a numerical representation of masonry as a homogeneous continuum, with units, mortar joints, and their interfaces modelled as a unified material (Figure 23). This modelling technique demonstrates its effectiveness, drastically reducing both the number of unknowns in the elastoplastic equilibrium of the structure and the number of parameters required to describe the materials' behaviour. Unlike micro-modelling, where small elements like thin mortar layers need to be modelled, this technique allows for a larger mesh size. This

means that even for large models, such as representation of masonry aggregates, computationally feasible solutions can be obtained without reducing accuracy (28).

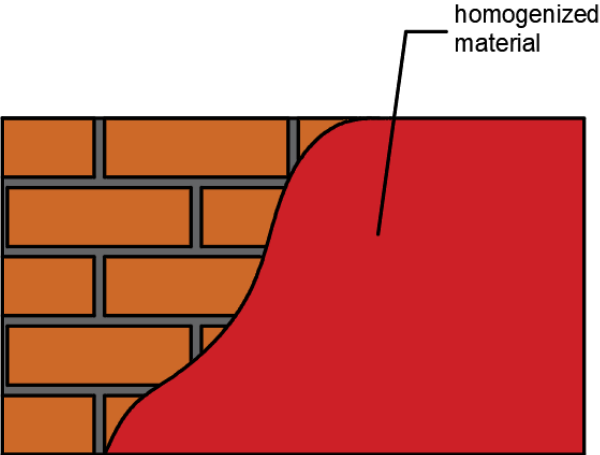


Figure 23: Homogenized masonry.

The crucial process in achieving a robust macro-model is the homogenization (Figure 24), which defines the material by deriving constitutive relations that describe average stress and strain behaviors based on the properties of individual components (26). Homogenization techniques represent a significant advancement in masonry modelling because they allow the use of standard material models developed for isotropic materials (3). This method can be applied to both regular and irregular masonry, where it is possible to extract a Representative Volume Element (RVE) that globally represents the behaviour of the entire building's characteristics. By studying the RVE, the properties of the homogenized masonry material can be extracted.

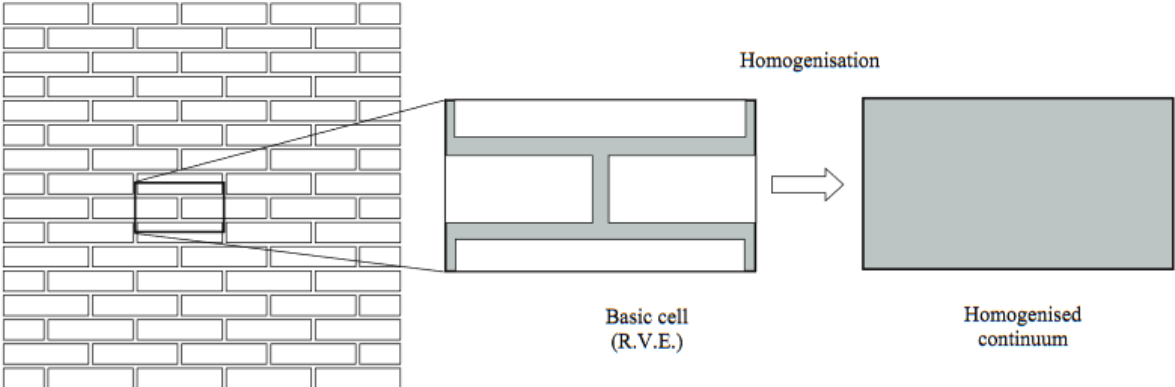


Figure 24: Homogenization technique (42).

Estimating homogenized continuum material properties can be done through either laboratory tests or numerical calibration simulations. In the laboratory, properties are determined based on

compressive strength data obtained from in-plane diagonal compression tests conducted on a portion of the masonry wall under investigation (42). Currently, there's significant focus on combining micro- and macro-modeling techniques using homogenization. The representative volume element (RVE) can also be analysed mechanically by simulating its response numerically (43). Micro-modelling techniques allow for modelling the RVE in all its components, providing a calibration of the masonry material similar to what is achieved through time-consuming laboratory experiments. However, the practical application of such numerical homogenization is limited due to the numerous parameters involved in evaluating individual units and mortar properties. The research community is actively working to overcome this limitation. For instance, in (44) it was proposed a homogenization strategy that can be done starting from available inspection results. In the study, the RVE was studied using a discrete element model and calibrated with inspection results. Applying the Drucker-Prager criteria to the RVE models, the brick masonry was homogenized. Their proposed method facilitates the characterization of masonry without necessitating any destructive testing, by relying on models that get an optimal balance between simplicity, time efficiency, and the accuracy of outputs.

The primary limitation of the homogenization technique is its inability to directly account for masonry's anisotropic properties. Within a structure, certain areas may exhibit a specific arrangement of components that make them more vulnerable to local effects, such as sliding mechanisms. Consequently, this can lead to the oversight of local phenomena. Furthermore, conventional constitutive models typically do not account for the variation of material properties with the "scale effect". Quasi-brittle materials such as masonry show changes in tensile strength and structural brittleness depending on the size scale. Therefore, it is crucial to consider the "size effect" during the homogenization process to ensure alignment between the model simulations and reality (45).

An interesting study in the literature is conducted by Lourenco (42), where the author compares the effectiveness of a homogenized masonry wall model with experimental results. This study also compares the results with previous research in which the author modeled the same wall using a micromechanical approach (46). The tests were performed on a masonry wall having a width/height ratio of one (990 x 1000 mm). The wall was initially subjected to a vertical precompression and then a horizontal load was monotonically increased under displacement control until failure (Figure 25).

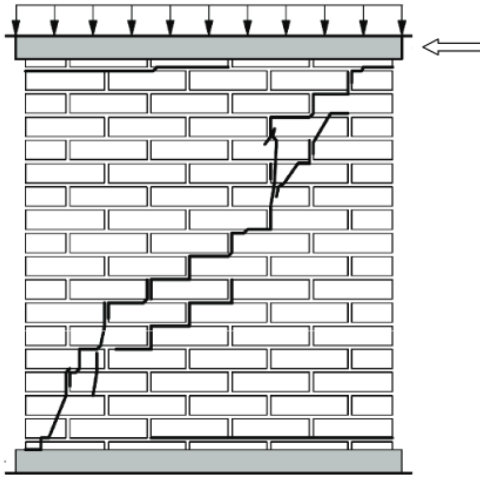


Figure 25: Experimental crack pattern of the tested wall (42).

In the study, masonry properties were assessed using the proposed micro-mechanical homogenization technique. Despite using a coarse mesh, the finite element method with the homogenization technique showed correspondence with the results derived from the more detailed micromodel and experimental results (Figure 26).

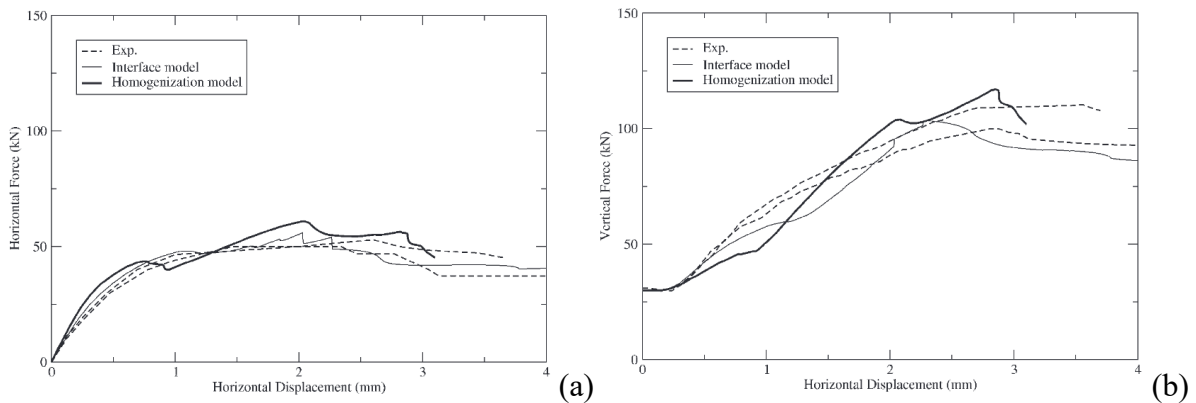


Figure 26: Comparison between experimental results, interface model and homogenization model: (a) horizontal force vs. displacement; (b) vertical force vs. displacement (42).

Another relevant use of this technique is the work carried out by Tarque in (19), who calibrated and modeled the behavior in the plane of the brick wall. The author adopted both macro-modeling and simplified micro-modeling strategies to perform pushover analysis. Both approaches show good agreement with the envelope of the experimental test.

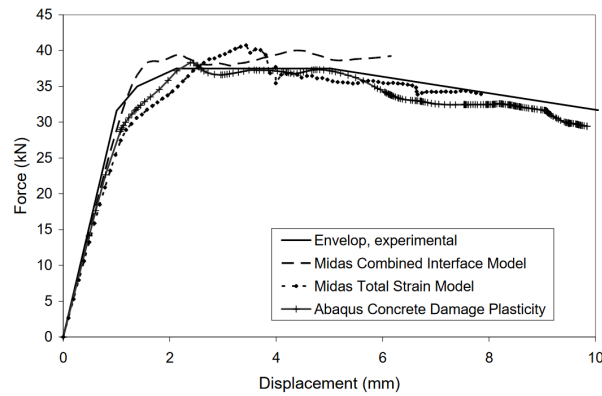


Figure 27: Pushover curves: experimental results and numerical modelling (19).

Additionally, in (19) a parametric study was conducted to observe the impact of the variation in the strength and fracture energy in the response of the model. Results showed that compressive strength or compressive fracture energy did not change the behavior significantly (Figure 28), while the change in tensile strength or tensile fracture energy had a relevant impact on the response (Figure 29).

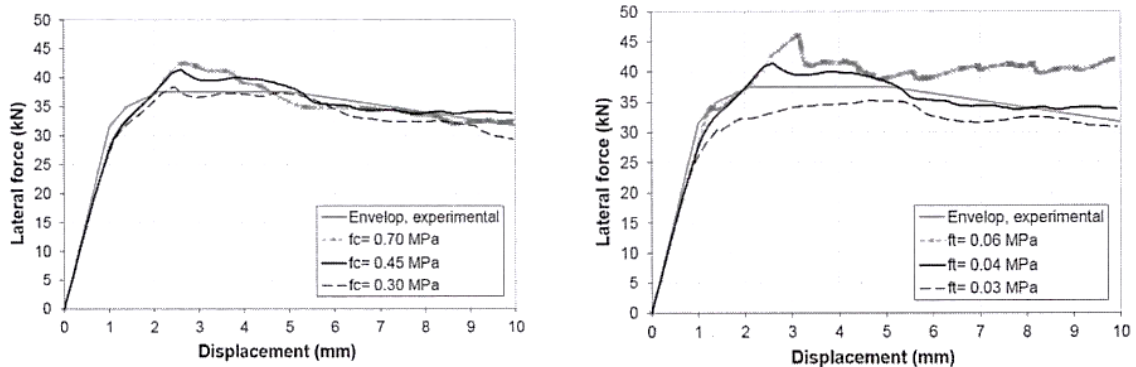


Figure 28: Parametrical study: a) influence of the compressive strength; b) influence of the tensile strength (19).

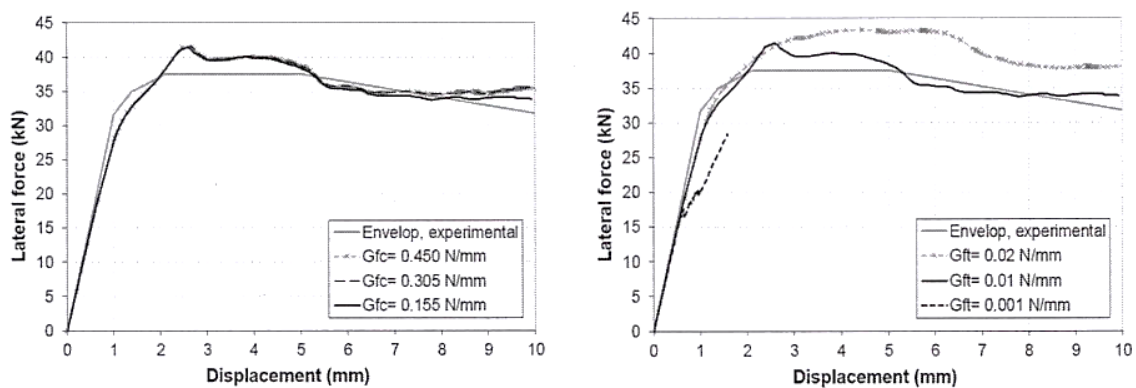
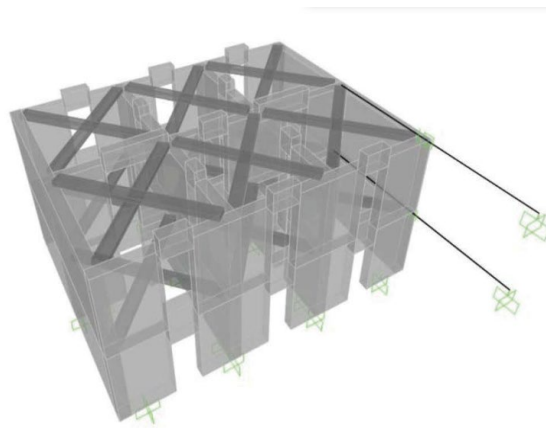


Figure 29: Parametrical study: a) influence of the compressive fracture energy; b) influence of the tensile fracture energy (19).

### 3.5 Modelling interconnections between units.

The assumptions made in modelling the interaction between units have a considerable impact on the predicted seismic response of units within an aggregate (7). However, literature lacks numerous examples of explicit modelling of unit interconnections within aggregates. In this paragraph two examples are examined.

Formisano and Massimilla in (25) proposed a simplified modelling approach to assess the seismic performance of a unit within an aggregate without analysing the entire aggregate. Their study focused on an aggregate consisting of three identical units modelled using an Equivalent Frame Model. Initially, they evaluated the seismic response of the entire aggregate assuming the units fully connected. Then, they modelled the units as separate entities, introducing appropriate boundary conditions in the form of elastoplastic links to account for the influence of adjacent units. These elastoplastic links were positioned at the floor levels, corresponding to the transverse interface walls (Figure 30).



*Figure 30: Equivalent Frame Model of the external unit (25).*

The authors proposed a procedure to assess the strength and stiffness of the elastoplastic links to model the unit directly as isolated while still considering the "aggregate effect". In the case study presented, the pushover curves of the modelled single unit with nonlinear links closely approximated the response of the same unit within the aggregate (Figure 31).



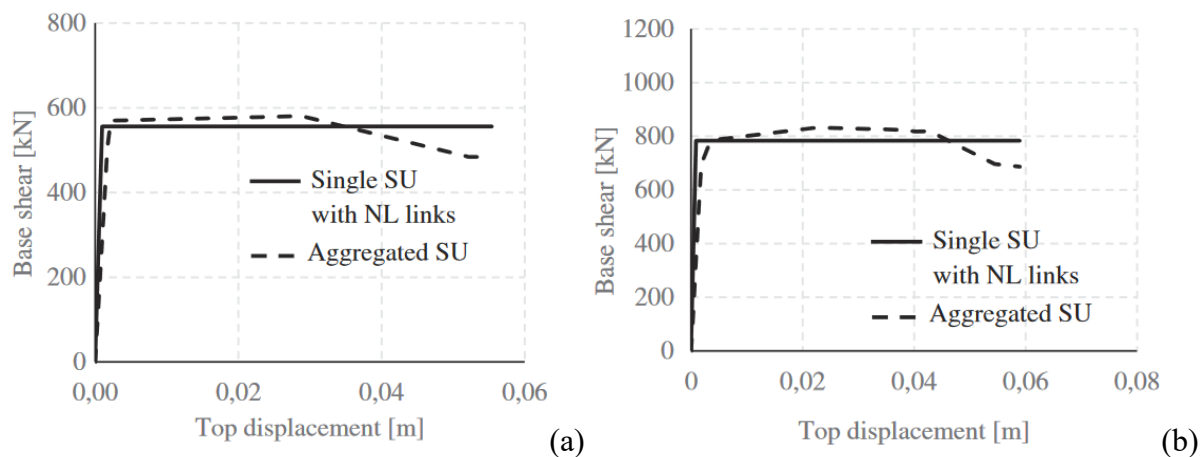


Figure 31: Pushover curves of (a) the intermediate unit and (b) external unit (25).

A highly advanced study concerning the explicit modelling of interfaces between units was conducted by Tomic in (8). This study concentrated on modelling the interaction between individual units, replicating the shake-table test performed on the half-scale two-unit masonry aggregate at the National Laboratory for Civil Engineering (LNEC) (7). In this research, the aggregate was modelled using a three-dimensional equivalent frame model (Figure 32). Each pier and spandrel within the aggregate was represented as macro-elements capable of capturing both in-plane and out-of-plane failures. All elements were developed and implemented in OpenSees.

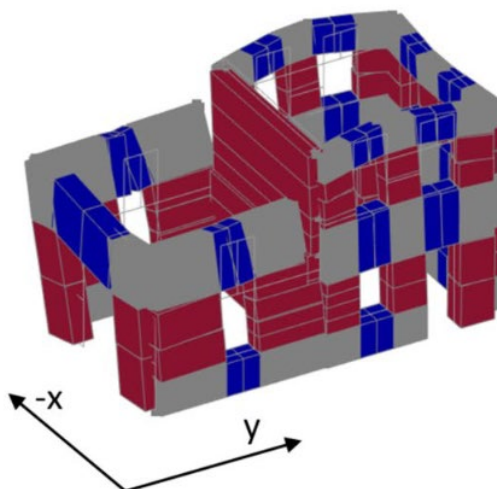


Figure 32: Equivalent Frame Model of the aggregate (8).

In order to effectively model the complex nonlinear behaviour that may occur at the interfaces between units, zero-length elements were introduced. These elements were associated with a non-dimensional material (nD), named as *CohesionFriction3d*, characterized by a Mohr-

Coulomb law in shear (in the y and z directions) and acting as a stiff axial spring in the x direction with limited tensile strength (Figure 33).

The input parameters of this nDmaterial include the uniaxial material model, fracture energy, cohesion, and friction coefficient of the interface. This newly developed material can evaluate the shear capacity as a function of the normal force across the interface and can also consider degrading cohesion over time.

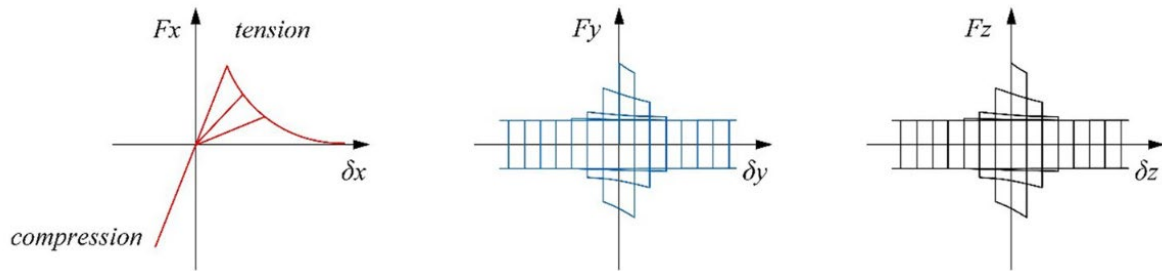


Figure 33: constitutive CohesionFriction3D model for unit-to-unit connections (8).

The authors also explored three additional approaches for modelling the connection between the two units: using three separated 1D zero-length elements for each direction, assuming the units as either fully connected, or isolated. The research demonstrates that the most detailed representation with the nD interface showed less conservative results compared to other models in terms of fragility curves (Figure 34). In conclusion, while modelling the units as either fully connected or separated may lead to conservative predictions, these approaches may not accurately predict the appropriate failure mechanism.

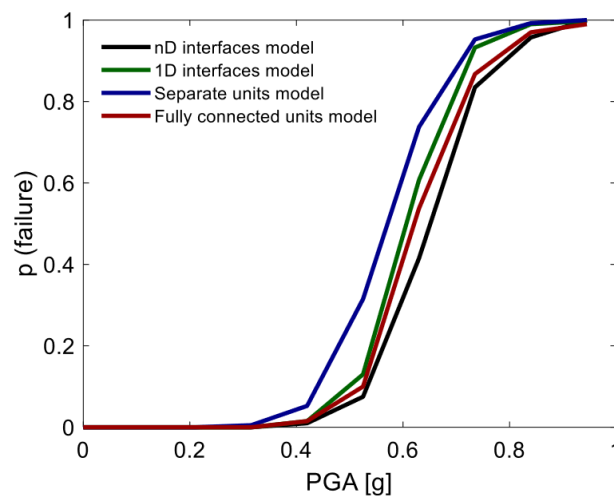


Figure 34: Comparison of seismic fragility curves for the four aggregate modelling approaches presented in (8).

# 4. Analysis and verification methods

The chapter discusses the analysis methods employed in this research, including modal analysis, nonlinear static analysis (pushover), nonlinear dynamic analysis and a quantitative seismic assessment utilizing the N2 method. Modal analysis evaluated the dynamic properties of the structures and the obtained fundamental mode of vibration was used as horizontal load profile for pushovers. Nonlinear static analyses were conducted to evaluate the longitudinal base reactions of the building respect to the displacement of a significant point, and the results were used to assess the seismic vulnerability of the structures according the N2 method. The pushover curves were compared with nonlinear dynamic analyses, which were conducted with the 2009 L'Aquila earthquake as dynamic input.

## 4.1 Modal analysis and response spectra

Modal analysis is the process of evaluating the dynamic characteristics of a structural system in terms of natural frequencies  $\omega$ , mode shapes and the amount of mobilized mass that can be associate to each mode of vibration (47).

The natural frequencies of a structural system are the frequencies at which the structure will tend to oscillate freely after an initial disturbance. In response to a specific natural frequency, the structure moves according to a pattern that is proportional to its mode shape. The dynamic characteristics of the structure are a function of its mass, stiffness, and damping properties. Modal analysis allows to describe an n-degree-of-freedom system as the superposition of N individual one-degree of freedom system, each of them characterized by its distinct natural frequency and mode shape (Figure 35). In the case of continuous systems, there will be an infinite number of natural frequencies, each corresponding to a unique mode shape (48).

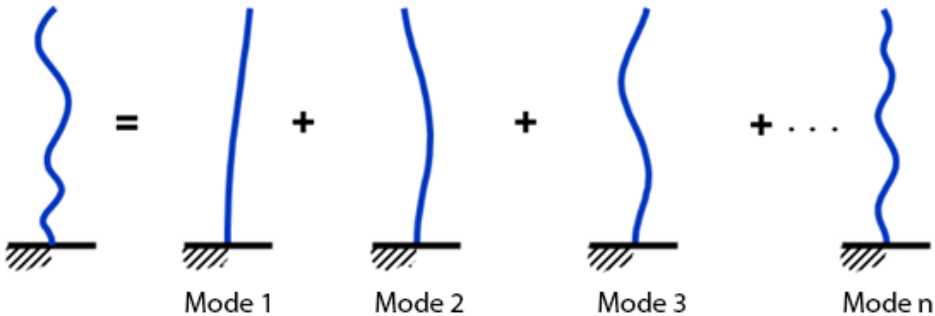


Figure 35: Modal decomposition of a n-degree of freedom system (47).

The dynamic response of a system is the linear combination of its vibration modes. The dynamic equilibrium condition for a multi-degree-of-freedom system subjected to a seismic input, written in matrix form, is formally analogous to that of the simple oscillator:

$$[M]\{\ddot{X}\} + [C]\{\dot{X}\} + K\{X\} = \{F\} \quad [ 7 ]$$

In the case where the system is damped, the system of differential equations can be decoupled into  $n$  equations each containing a single unknown function. This is possible by switching from geometric ( $x_i$ ) to modal coordinates ( $p_i$ ):

$$\ddot{p}_i + 2\zeta_i\omega_i\dot{p}_i + \omega_i^2 p_i = -\Gamma_i\ddot{u}_g \quad [ 8 ]$$

In equation [ 8 ],  $\zeta_i$  is the damping ratio,  $\omega_i$  the natural frequency (inverse of the period  $T_i$ ),  $p_i$  is the modal coordinate and  $\Gamma_i$  is the modal participation factor.  $\Gamma_i$  indicates the contribution of the individual modes to the overall motion of the structure.

$$\Gamma_i = \frac{\Phi_i^T m I}{\Phi_i^T m \Phi_i} \quad [ 9 ]$$

The decomposition of the seismic response into the contribution of individual modes is the foundation of modal analysis. The lowest frequency denoted as  $\omega_1$ , is known as the fundamental frequency. The fundamental period  $T_1$  of the structure can be defined based on the fundamental frequency as:

$$T_1 = 2\pi/\omega_1 \quad [10]$$

As the mode number increases, the participating mass gradually decreases. The fundamental mode is characterized by mobilizing the largest amount of mass. According to the Italian building code NTC2018 (11), only vibration modes with a total participating mass of at least 85% or modes with participating mass exceeding 5% individually are considered.

The solution of the equations of motion [7] provides the time history of displacements for each vibration mode. For practical purposes, designers are interested in the maximum stresses experienced by the structure during earthquakes, rather than the entire time history of the response (49). To achieve this, the designer utilizes the elastic response spectrum. This spectrum provides a graphical representation of the peak value of a response quantity as a function of the natural vibration period of the system  $T_n$ . The plotted response quantity can be pseudo-acceleration, pseudo-velocity, or pseudo-displacement.

For a one-degree-of-freedom system, the maximum seismic action  $F_e$  can be computed as a static force proportional to the maximum displacement  $u_{max}$ :

$$F_e = m \omega^2 u_{max} \quad [11]$$

Where  $\omega^2 u_{max}$  represents the pseudo-acceleration. Since free vibration motion depends only on frequency  $\omega$  and damping ratio  $\zeta$ , systems with equal values in these parameters exhibit the same maximum acceleration when subjected to identical seismic input. Consequently, the elastic spectrum corresponding to a specific seismic action can be constructed by evaluating the maximum seismic response for systems characterized by different periods.

The elastic spectra, considered by building regulations, are related to multiple earthquakes that could affect the structure. These spectra are developed by enveloping response spectra from various seismic events that are representative of the seismic characteristics of the region and local ground conditions. The technical code spectra (Figure 36), which are derived from a regularization of the previously described spectra, are described by functions of the period that are valid within a certain interval.

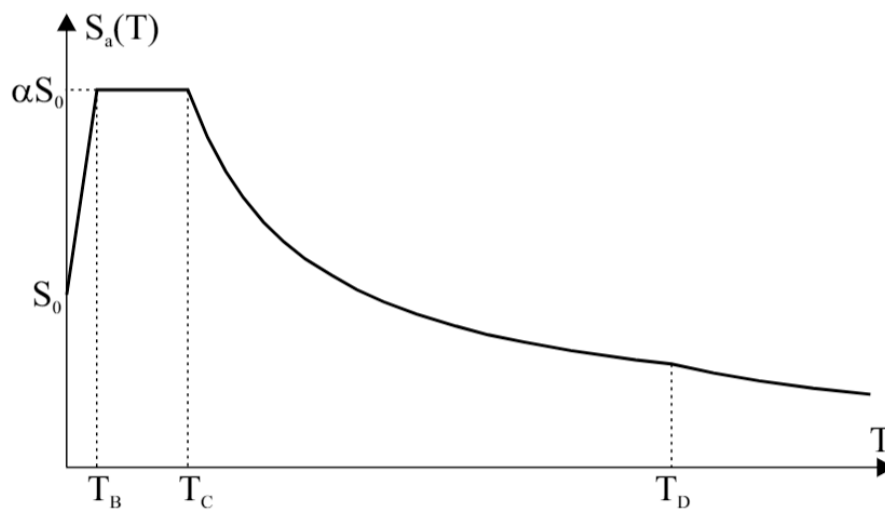


Figure 36: Technical code elastic spectrum (50).

Figure 36 illustrates an example of a technical code elastic spectrum.  $T_B$ ,  $T_C$  and  $T_D$  represent the periods that divide the domain of the functions describing the spectrum.  $S_0$  (or PGA) is the peak ground acceleration, corresponding to the acceleration experienced by an infinitely stiff system.

In the elastic spectrum, it is assumed that the structure responds to seismic action while maintaining elastic behaviour. However, considering the nonlinear behaviour of the structure

can reduce the required strength to withstand seismic events (51). The inelastic constant-ductility spectra are derived from elastic spectra and account for the effects of structural and material nonlinearity (Figure 37). It is possible to consider the dissipation of structures due to their non-linear behaviour, considering the reduction factor  $q$ :

$$q = \frac{F_e}{F_y} \quad [12]$$

Where  $F_e$  is the structure strength requested to the infinitely elastic system and  $F_y$  the yielding strength of the structure. If the system shows a certain ductility  $q$ , the inelastic response spectra can be defined as:

$$S_{ai}(\mu, T) = \frac{S_{ae}(T)}{q(\mu, T)} \quad [13]$$

The rule codes EC(52) and NTC (11) adopted the formulation of  $q$  given by (50):

$$\begin{cases} q = (\mu - 1) \frac{T}{T_c} + 1 & (T < T_c) \\ q = \mu & (T \geq T_c) \end{cases} \quad [14]$$

Where  $\mu$  is the ductility demand, defined as the ratio between the displacement demand and the yielding displacement.

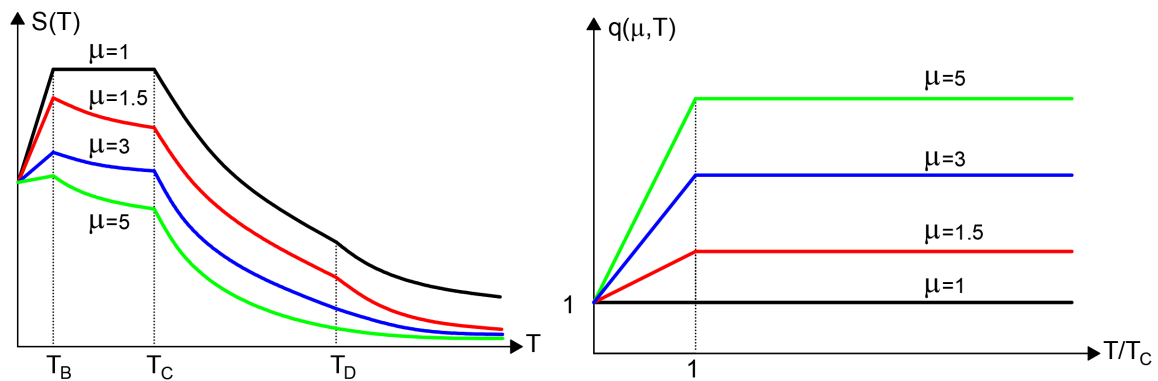


Figure 37: Inelastic constant ductility spectra.

Modal analysis was used to define the fundamental mode and the lateral force distribution applied during non-linear static analysis. The natural frequencies of the structure were used to estimate the viscous damping applied during dynamic analyses. While the response spectra were used in the seismic vulnerability assessment.

## 4.2 Nonlinear static analysis (pushover)

Nonlinear static analysis involves incrementally applying either a displacement or horizontal load and evaluating the structural response (53). This type of analysis is commonly referred to as pushover analysis. The pushover outputs are evaluated as force-displacement curves, which correlate the base reaction force of the structure with the displacement of a significant point. In displacement-controlled pushover analysis, the horizontal load applied to the structure is incrementally increased until a specific displacement target is achieved at a significant point. The applied horizontal load at each step is defined as  $P_i = \lambda_i P_0$ , where  $\lambda_i$  is the load factor of the  $i$ -th step and  $P_0$  is the horizontal load distribution. In load-controlled pushover analysis, an imposed displacement is gradually incremented at each  $i$ -th step, where the displacement  $D_i = \lambda_i D_0$ , with  $D_0$  representing the initial displacement and  $\lambda_i$  denoting the increment factor.

The response of a multi-degree-of-freedom (MDOF) structure is simplified to that of an equivalent single-degree-of-freedom (SDOF) structure with perfectly plastic elastic behaviour. This procedure is explained in the paragraph related to seismic assessment. There are various versions of pushover analysis in the literature (21): unimodal method, multimodal method, non-adaptive method, and adaptive method. In unimodal methods, the transformation from a MDOF system to a SDOF system considers only one vibration mode of the structure, generally the fundamental mode. For multimodal methods, the transformation accounts for multiple vibration modes. The eigenvectors used in unimodal and multimodal methods can either remain constant with the increase in horizontal forces (in the case of non-adaptive methods) or vary according to the current elastic characteristics of the system (in the case of adaptive methods). In non-adaptive methods, the eigenvectors are calculated at the beginning of the analysis and remain constant throughout the incremental loading path, even when, due to plasticization, the conditions of the structure are significantly different from the initial ones. Conversely, in adaptive methods, the eigenvectors are recalculated whenever there is a change in the static scheme of the structure (for example, following the plasticization of elements). Adaptive methods have the disadvantage of being much slower since the eigenvectors must be recalculated whenever there is a change in the static scheme of the structure. In this study, the non-adaptive unimodal pushover was used as it is the method required by NTC2018 (11) for the calculation of existing masonry buildings.

The most significant aspect of pushover analysis is that it is a nonlinear analysis: the stiffness matrix is a function of displacement and changes at each step of load application, necessitating

the update of the stiffness matrix during the analysis. Literature presents various numerical methods based on iterative procedures, which can account for stiffness changes, such as the forward Euler method, the modified Newton-Raphson method, or the Arch Length method, listed in order of increasing complexity (54). These algorithms achieve a solution by adopting an approximation that assumes linear behaviour between two very small (assumed infinitesimally) steps.

The modified Newton-Raphson algorithm (Figure 38) is preferred for its efficiency in updating the solution at each increment, aiming to closely approximate the exact solution based on a defined error measure known as the residual load (R). The residual load is the difference between the external load applied and the effective internal resistance mobilized by the structure due to the displacement achieved at the end of the step (55).

This algorithm achieves the solution at the new step  $\alpha + 1$  obtained through an iterative process, which starts from the result obtained in the previous step  $\alpha$ . Although R is a nonlinear function of the displacement u, it is possible to linearize the relationship between R and the displacement increment du, using the Taylor expansion:

$$R^{\alpha+1} = R^{\alpha} + \frac{dR^{\alpha}}{du} du^{\alpha+1} + h. o. t. \quad [15]$$

As we are looking for  $R^{\alpha+1} = 0$  and we can neglect higher order terms (h.o.t.), we get:

$$du^{\alpha+1} = K_T^{\alpha} R^{\alpha} \quad [16]$$

Considering that it can be demonstrated that:

$$\frac{dR}{du} = K_T^{-1} \quad [17]$$

$$u(t)^{\alpha+1} = u(t)^{\alpha} + du^{\alpha+1} \quad [18]$$



Although the symbolic notation for  $K_T^{-1}$  was used, the reversal of  $K_T$  is not performed due to its numerical expense. Instead, the linear set of equations is solved using a suitable efficient method, such as the conjugate gradient or Gauss-Jordan method.

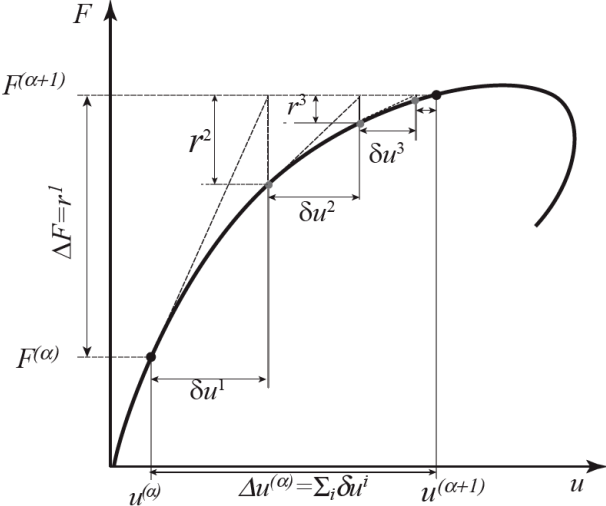


Figure 38: Newton-Raphson method illustrated (55).

The basic Newton Raphson method maintains the same stiffens  $K_T^\alpha$  for the entire loading phase without recalculating it at each iteration of the residual. The same solution is obtained but with a greater number of iterations.

The modified Newton-Raphson method is not able to correctly identify the equilibrium if the phenomenon involves buckling or softening of materials (Figure 39). To solve this problem, it is possible to use a more advanced computational technique, such as the arc length method.

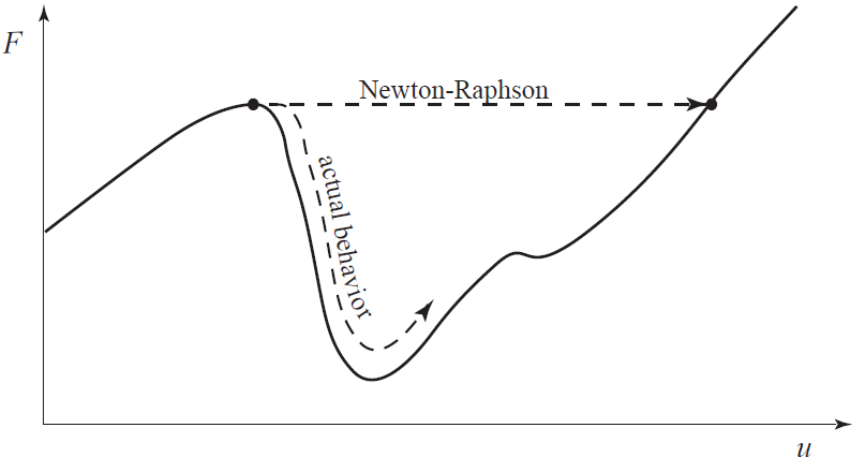


Figure 39: Newton-Raphson methods is not suitable for problems involving softening, buckling (55),

## 4.2.1 Horizontal load distribution

The capacity curve of a structure is not determined in a unique manner but depends on a series of factors, primarily the choice of the control point and the load profile used to increase the horizontal loads. Thus, selecting an appropriate load profile to accurately represent the seismic response is crucial. According to section 7.3.4.2 of the D.M. 17/01/2018 (11), there must be at least two load profiles: one proportional to static forces and one proportional to masses (Figure 40).

In the first case, the increase in loads occurs proportionally to the eigenvector of the first modal shape and remains constant until the structure collapses. In this case, the first mode of vibration is determined through modal dynamic analysis  $\Phi^T = (\Phi_1, \Phi_2, \Phi_3, \dots)$  and the force on each node is calculated using the following expression:

$$F^i = \alpha m_i \Phi_i \quad [19]$$

This method can only be adopted if the first mode of vibration includes at least a modal mass participation of 75% of the entire mass of the structure. If this requirement is not met, it would be necessary to proceed with a multimodal load profile, which is obtained by combining multiple modal shapes according to the Square Root of the Sum of the Squares (SRSS) distribution.

The load distribution proportional to masses assumes that the force  $F_i$  at each floor is equal to its mass  $m_i$ . This method is also known as "uniform" because typically, the masses of each floor of a building are equal. This approach ensures a straightforward and often conservative estimation of the force distribution, reflecting a scenario where seismic inertia affects each level of the structure uniformly. This method is particularly useful for initial seismic assessments or when detailed modal information is not available, providing a simplified effective means to approximate the seismic demand on a structure.

Typically, the capacity curve associated with a uniform distribution is characterized by a larger shear force at the base and a smaller displacement capacity compared to the curve related to a modal distribution (49). This occurs because the center of mass for the uniform distribution is located at a lower level compared to that of the modal distribution, resulting in a smaller overturning moment at the base. The current NTC18 regulations for seismic assessment

established the need to use both the uniform and the modal horizontal profile, assuming that the real solution will be in between, as depicted in Figure 40.

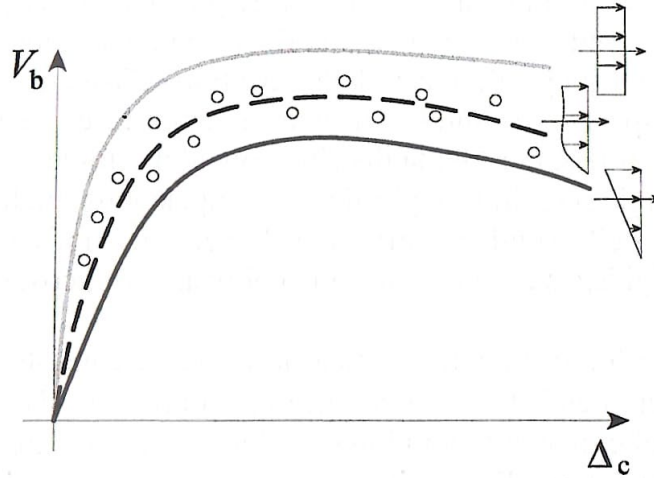


Figure 40: Capacity curves under uniform and modal horizontal load profiles, the real solution in between. (21).

### 4.3 Non-linear dynamic analysis

Nonlinear dynamic analysis represents a sophisticated approach to evaluate structural performance under seismic loads, capturing the complex interactions between inertia, damping, and stiffness that evolve in the structure during an earthquake. This method offers a rigorous solution by solving the motion equation step by step:

$$M \ddot{U} + C \dot{U} + F_{int}(U) = -MR\ddot{x}_g \quad [20]$$

In [20],  $M$  is the mass matrix,  $C$  is the damping matrix,  $F$  is the internal forces vector,  $U$ ,  $\dot{U}$ , and  $\ddot{U}$  represent the displacements, velocity, and acceleration respectively, and  $R$  is the vector related to the influence of the earthquake, proportional to the masses and to the ground acceleration. The analysis is performed respect a certain time history (accelerogram) assigned at the base of the structure (15). The computational demand of solving equation [20] at each step is high. The current computational capabilities of computers facilitate this operation through numerical integration techniques without significant difficulty. However, various modelling problems, as well as synthesis and interpretation of results, still limit the direct implementation of nonlinear dynamic analysis in standard engineering applications (15). Indeed, this methodology is the only approach that provides a reliable estimate of the seismic performance of complex structures under high-intensity design earthquakes (56), overcoming

the assumptions made in other seismic analysis. It directly solves the problem by assessing internal stresses from earthquake generated displacements.

The complexity of nonlinear dynamic analysis lies in accurately modelling the seismic input, defining the hysteretic behaviour of elements correctly and limiting the geometric uncertainties that affect seismic capacity, and demand. Seismic input can be modelled using real, artificial, or simulated signals (11). The method can be applied effectively when seismic masses are associated with the model components. All elements of interest must exhibit nonlinear behaviour and the ability to dissipate energy through damage. Additionally, the system can dissipate energy through dissipative forces generated within the structure due to relative motion between its components. Damping can be determined based on the model's masses and/or stiffness. The Rayleigh method will be discussed in the following paragraph to evaluate the system's viscous damping.

### **4.3.1 Damping: the Rayleigh method**

In nonlinear modelling, materials are characterized by employing nonlinear constitutive models, which inherently account for a portion of the energy dissipation absorbed by structures during seismic events. However, other critical sources of seismic energy dissipation, such as friction between structural components and crack openings, also play significant roles. These mechanisms can be effectively incorporated into simulations by utilizing the Rayleigh damping model (Figure 41).

The Rayleigh method, when applied to masonry structure nonlinear dynamic analysis, involves expressing damping as a linear combination of mass and stiffness matrices:

$$c = a_0 m + a_1 k \quad [21]$$

The first term represents the mass proportionality of the damping and the second the stiffness proportionality. The generalized damping of each mode can be evaluated as:

$$C_i = a_0 M_i + a_1 \omega_j^2 M_j \quad [22]$$

While the damping ratio of each mode can be computed as:

$$\zeta_i = \frac{a_0}{2} \frac{1}{\omega_i} + \frac{a_1}{2} \omega_i \quad [23]$$

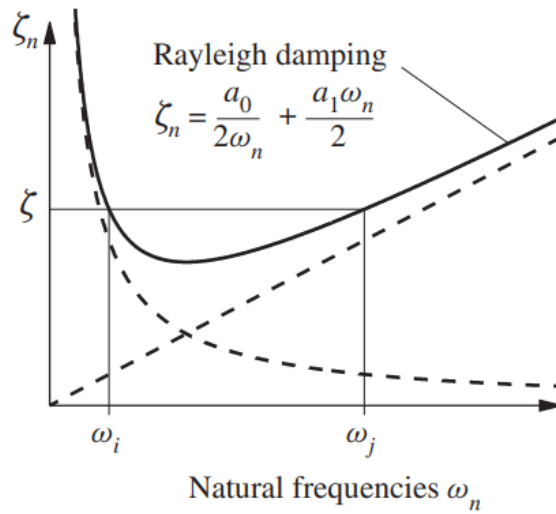


Figure 41: Rayleigh damping (51).

The coefficients  $a_0$  and  $a_1$  can be determined from specific damping ratios that belong to two different modes  $i$  and  $j$ :

$$a_0 = \zeta \frac{2\omega_i\omega_j}{\omega_i + \omega_j} \quad [24]$$

$$a_1 = \zeta \frac{2}{\omega_i + \omega_j} \quad [25]$$

## 4.4 Verification methods

The Eurocode 8 (52) and the Italian NTC 2018 (11) allow for seismic performance assessments of buildings using the N2 method (47, 54). This method enables the evaluation of seismic vulnerability through pushover analysis, even for structures with multiple degrees of freedom. The procedure involves determining the seismic capacity and demand of the building and comparing them in terms of required displacement or ductility.

### 4.4.1 Capacity assessment

From the nonlinear static analysis, the capacity curve of a Multi-Degree-of-Freedom (MDOF) system is provided. The method assumes that the structure's response is dominated by a single mode of vibration, and that the shape of this mode remains constant throughout the analysis. To obtain the equivalent Single-Degree-of-Freedom (SDOF) capacity curves, it is sufficient to divide both the base reaction and the control node displacement by the modal participation factor  $\Gamma_1$  of the fundamental mode (Figure 42: Equivalent SDOF capacity curve.), evaluated from a modal analysis using equation [ 9 ]:

$$F_{bu}^* = \frac{F_{bu}}{\Gamma_1} \quad [26]$$

$$d_u^* = \frac{d_u}{\Gamma_1} \quad [27]$$

Where  $F_u$  and  $d_u$  represent the base reaction and displacement achieved at failure, respectively. From the capacity curves, the failure of the structure can conventionally be assumed when the base reaction has a reduction of 15% compared to the maximum value achieved. Conventional failure may be anticipated by real failure in case of a local or global mechanism.  $d_u^*$  represents the maximum displacement associated with  $F_{bu}^*$ .

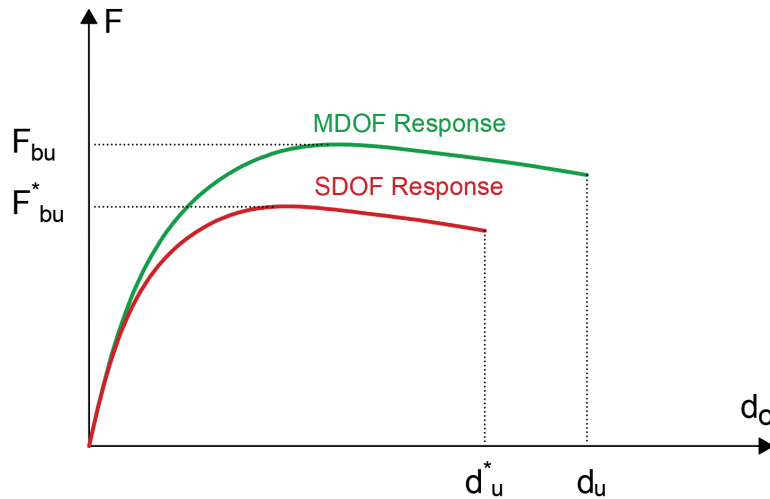


Figure 42: Equivalent SDOF capacity curve.

The obtained capacity curve is further simplified by approximating it with a bilateral elastic-perfectly plastic curve (Figure 43). The bilinearization is conducted ensuring that the areas under the two curves are equal, and an intersection point occurs at 60% of the  $F_{bu}^*$  value. This

bilinearization allows the determination of the yielding condition  $(F_y^*, d_y^*)$ , which correspond to the transition from the elastic to the plastic branch.

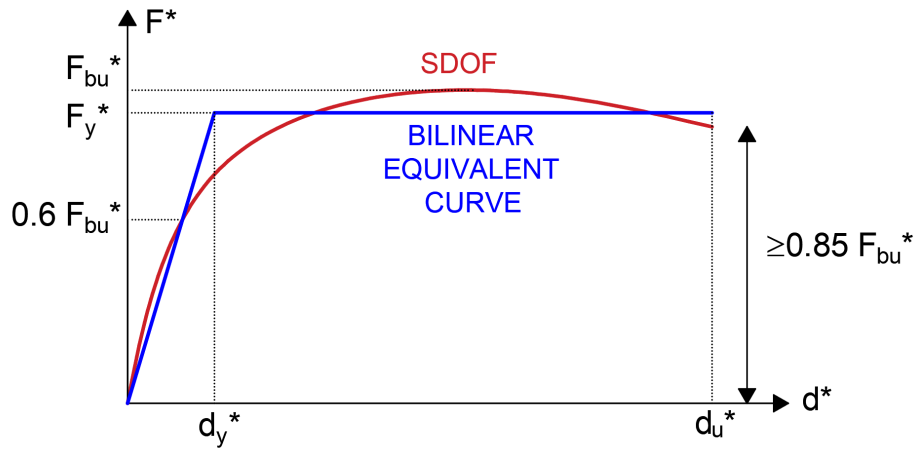


Figure 43: Bilinear equivalent capacity curve.

The ductility capacity of the system is evaluated as:

$$\mu_c = \frac{d_u^*}{d_y^*} \quad [28]$$

It is possible to dynamically identify the structure by assuming the stiffness, mass, and period of the structure as:

$$K^* = \frac{F_y^*}{d_y^*} \quad [29]$$

$$m^* = \phi_1^T M I \quad [30]$$

$$T^* = 2\pi \sqrt{\frac{m^*}{k^*}} \quad [31]$$

#### 4.4.2 Seismic demand evaluation

Once the period of the structure is known, it becomes possible to evaluate the corresponding maximum pseudo acceleration that the structure could experience if it maintains elastic behaviour (Figure 44). This assessment is conducted using the elastic response spectrum, which

must be defined in accordance with the specific seismic characteristics of the region and local ground conditions.

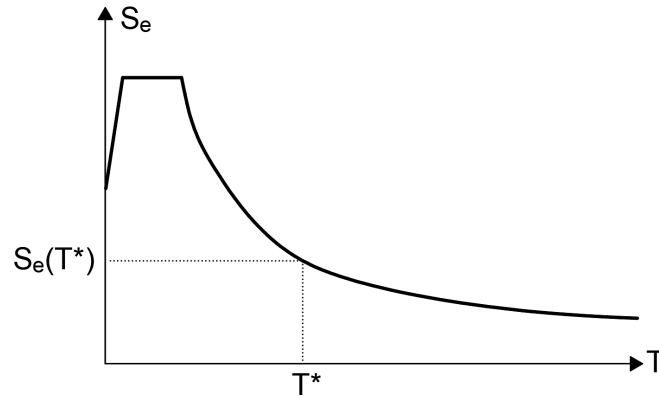


Figure 44: Elastic Spectrum.

The force  $F_E^*$  required to the elastic system and the corresponding pseudo displacement  $d_E^*$  can be evaluated as:

$$F_E^* = S_e(T^*) m^* \quad [32]$$

$$d_E^* = S_e(T^*) \frac{m^*}{k^*} \quad [33]$$

The reduction factor of the system can be evaluated as:

$$q^* = \frac{F_E^*}{F_y^*} \quad [34]$$

The ductility demand is assumed as:

$$\begin{cases} \mu_d = (q^* - 1) \frac{T_c}{T^*} + 1 & (T < T_c) \\ \mu_d = q^* & (T \geq T_c) \end{cases} \quad [35]$$

While the displacement demand is estimated as:

$$\begin{cases} d_{max}^* = \frac{d_{e,max}^*}{q^*} \left[ (q^* - 1) \frac{T_c}{T^*} + 1 \right] & (T < T_c) \\ d_{max}^* = d_{e,max}^* & (T \geq T_c) \end{cases} \quad [36]$$



### 4.4.3 Assessment criteria

The seismic assessment can be evaluated comparing the capacity and the demand in terms of displacement [38] and/or ductility [37].

$$\mu_d \leq \mu_c \quad [37]$$

$$d_{max}^* \leq d_u^* \quad [38]$$

In the NTC 2018 and EN 1998, verifications regarding seismic actions quantify the level of safety of the construction through the vulnerability index  $\xi_E$ , which is the ratio between the maximum seismic action that the structure can withstand and the maximum seismic action that would be used in the design of a new construction.

$$\xi_E = \frac{PGA_c}{PGA_d} = \frac{\tilde{d}_{e,max}^*}{d_{e,max}^*} \quad [39]$$

Where  $\tilde{d}_{e,max}^*$  and  $\tilde{q}^*$  are the maximum elastic displacement and reduction factor associated with the spectrum of the earthquake inducing the limit state of the structure

$$\begin{cases} \tilde{d}_{e,max}^* = \frac{d_u^* \tilde{q}^*}{(\tilde{q}^* - 1) \frac{T_c}{T^*} + 1} & (T^* < T_c) \\ \tilde{d}_{e,max}^* = d_u^* & (T^* \geq T_c) \end{cases} \quad [40]$$

$$\begin{cases} \tilde{q}^* = (\mu_c - 1) \frac{T^*}{T_c} + 1 & (T^* < T_c) \\ \tilde{q}^* = \mu_c & (T^* \geq T_c) \end{cases} \quad [41]$$

# **5. Numerical modelling of aggregate buildings in Opensees using STKO**

## **5.1 Introduction to OpenSees**

OpenSees is a robust software framework predominantly written in C++, designed to simulate applications in earthquake engineering using finite element methods. Developed by the Pacific Earthquake Engineering Research Center (PEER) in 1997, it is an open-source architecture, based on a collaborative community in which each user can create custom materials and elements. The framework is used for its speed, stability, and efficiency in handling large nonlinear models with multiple methods (10).

To use OpenSees features, users must compile code written in the Tcl (Tool Command Language) programming language, a dynamic language based on string operations. While becoming familiar with Tcl can be a challenge at first, it quickly turns into a powerful tool that offers flexibility in model development and rapid execution of complex analyzes without requiring mastery of complex computational procedures.

The structure of OpenSees is solid and simple. A model generator integrates components such as elements, nodes, constraints, and load models into the domain. This allows users to define geometry, assign materials to elements, specify mechanical characteristics, assign loads or constraints, and conduct both static and dynamic analyses. This iterative process, while easy to manage, allows for the creation of complex models. During analysis, the model undergoes transitions between states over time intervals, all of which can be recorded for later examination. The user needs to script the structural model and define the desired output of the results.

OpenSees requires naming and explicitly considering degrees of freedom for all nodes, a task that becomes increasingly challenging when dealing with large models with numerous nodes. Modeling directly in 2D or 3D with OpenSees can be overly laborious and tedious. A more practical and efficient approach to utilizing the OpenSees framework is via STKO (Scientific Tool Kit for OpenSees) (9). STKO simplifies the modeling process, offering a user-friendly interface and automated functionalities that alleviate the complex aspects of model creation and

manipulation. STKO provides both a pre- and post-processor for OpenSees analysis. The user, without writing any script, can define the geometry, elements, materials, specify the loading conditions or constraints and set the analysis parameters. A user-friendly graphical interface allows for quick construction of geometry in the CAD environment and addition of components via an intuitive menu. The software automatically generates TCL codes that can be analyzed in OpenSees.

The team at ASDEA, the developers of STKO, has enriched the framework with additional materials and elements, improving the computation capabilities. Additionally, STKO simplifies post-processing of OpenSees outputs and offers the flexibility of working with Python instead of Tcl, which is generally more known and powerful (58).

STKO's fundamental modeling workflow (Figure 45) follows the following steps: geometry, element properties, physical properties, conditions (loads and constraints), definitions, interactions, and analysis steps. Each of the main steps will be introduced.

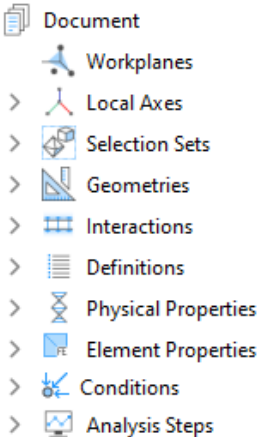


Figure 45: The STKO work tree.

### Definition of the geometry

STKO facilitates the use of various categories of geometries: nodes, faces, and volumes. These geometries can be intuitively generated in a CAD environment. Each category serves a unique purpose within the structural model. Nodes represent discrete points in space, while faces define two-dimensional surfaces, and volumes model three-dimensional regions.

OpenSees treats these three categories of geometry as distinct entities, but it is possible to establish connections between them through merging or interactions. The "*merge*" command is a functionality that allows users to combine multiple structural entities into a unified one. Interactions are tools used to connect nodes of different geometrical entities, specifying the type and degree of connection, associating specific conditions. When creating an interaction, it is necessary to define master and slave nodes, with slave nodes directly influenced by master nodes.

The geometric components can be organized into selection sets, a highly useful feature for automatically identifying by software when needed. Additionally, each component can be linked to a local reference system, distinct from the global one, providing a valuable resource for scenarios involving local settings.

## **Physical and element properties**

To each geometrical entity must be associated element and physical properties. The element property describes how the component should behave computationally. On the other hand, material properties govern the constitutive behavior of the structural elements, describing how material responds to various stress conditions. The software facilitates direct customization of material properties and provides a direct visualization of the stress-strain relationship within a material test application. This feature enables the user to evaluate the direct impact of parameter changes.

Both sets of properties are essential for accurately representing the structural behavior and performance in finite element analysis conducted using STKO. An extensive library of element and physical properties is available in the software. Some of these properties are directly derived from OpenSees, while others are developed by the ASDEA team. It is crucial to ensure coherence between the material and the type of element.

## **Conditions**

The conditions involve the association of boundary constraints, loads and masses applied to the structural model. Boundary conditions define how the structure is constrained at its boundaries,

specifying the type of constraints on the degrees of freedom (DOFs) of nodes in the model. Loading conditions describe the external forces, displacements, or other effects that act on the structure such as prestressing and temperature variation. OpenSees distinguishes masses from the self-weight of elements, so both must be explicitly associated with the model. Masses are crucial for defining inertial actions in dynamic analysis.

In OpenSees, loads and masses are directly applied to nodes by specifying specific conditions. However, STKO has introduced a feature enabling the application of forces or masses on edges or faces, which are then lumped among nodes by the software. This functionality is crucial for avoiding the necessity of adjusting loads each time the mesh size is changed.

## **Analysis Steps**

In the "analysis steps" section, the software is guided on how to set up the entire analysis process. Initially, the parameters that the software needs to record during the analysis are specified using a Recorder. Then, the conditions intended to be applied to the model are introduced. Once this setup is complete, the analyses to be performed can be defined. OpenSees offers a diverse library of available analyses and allows users to adjust their setup as required.

Additionally, STKO allows for the definition of Monitors, which can display the progression of specific parameters during the numerical simulation.

## **5.2 Numerical modelling approach**

This chapter describes the modeling strategies adopted to effectively replicate the behavior of masonry buildings using the Finite Element modeling method.

### **5.2.1 Masonry structure modelling approach**

In this research, the masonry structure was studied by performing a three-dimensional model using shell elements and employing the homogenized masonry approach for modeling.

Layered-shell elements were utilized to discretize masonry walls, as they effectively capture both bending and shear behavior (59). This is in strong contrast to 1D elements, which exclusively address flexural behavior and neglect shear effects, a limitation that is acceptable

for steel or reinforced concrete beams but unsuitable for stocky elements such as masonry panels, where the combination of shear and flexural behavior is predominant. Shell elements have multiple integration points in the direction of the shell thickness, allowing both in-plane and out-of-plane mechanisms to be considered. Compared to three-dimensional elements, these elements offer faster computations benefitting from a three-dimensional response (60).

It was decided to model the masonry structures with macro-elements based on the homogenized masonry approach. The homogenized masonry properties were introduced according to suggested values present in a previous study (see section 7.3), which were evaluated through calibration with respect to cyclic experimental tests. Since the goal was to model a large-scale aggregate building, micro-modelling was not feasible due to the excessive computational time required (26). Homogenized masonry was considered the best-suited option because it has been demonstrated to capture the critical behaviour of masonry while maintaining an optimal balance between simplicity, time efficiency, and the accuracy of results (28). Modelling the building with equivalent frames could not account for the implications of in-plane and out-of-plane failure mechanisms (32). Even with advanced strategies allowing for frame modelling including out-of-plane failures (35), defining a frame that accurately represents the structure could be challenging (31).

## **Layered shell**

The layered shell command in STKO creates the section of the multilayer shell element. It is a specialized type of section utilized to repeat composite structures by dividing them into separate layers (Figure 46). This approach allows for the accurate representation of complex composite materials and structures, taking into account the unique properties of each layer. The layered shell provides the flexibility to specify the number of layers, their thicknesses, and the types of materials associated with each layer.

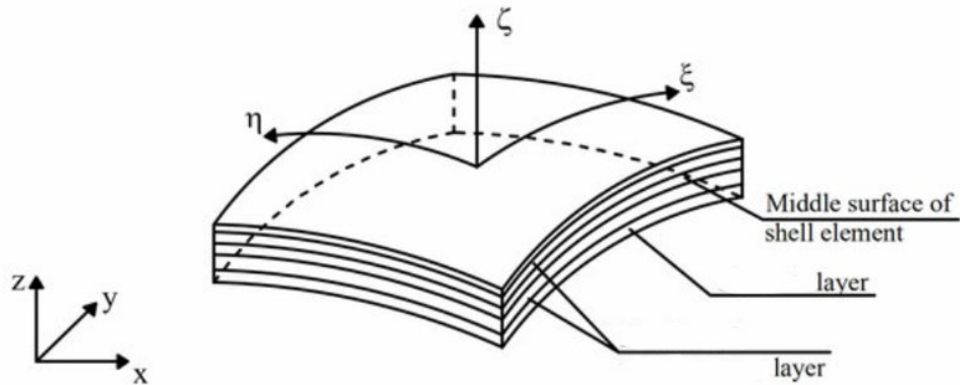


Figure 46: Layered Shell section(61).

From a numerical point of view, the Layered shell considers the axial deformation and curvature of the intermediate layer, subsequently evaluates the deformation of the other layers based on the assumption of section planarity hypothesis. The constitutive law selected for each layer leads to the evaluation of stresses at the integration points, and numerical integration is used to evaluate the internal actions.

### ***ASDShellQ4***

To the masonry geometries, the *ASDShellQ4* was associated: a versatile 4-node thick shell element designed to adeptly integrate membrane, bending, and out-of-plane shear behaviors (54). Its ability to support three-dimensional constitutive models allows the macro-element to capture both in-plane and out-of-plane failure modes. This element shows insensitivity to geometric distortion thanks to an advanced numerical membrane behavior.

The kinematics of this element can be assumed to be linear when there are no significant displacements or rotations expected relative to the overall building size and number of integration points perpendicular to the shell plane can be customized by the user (59).

This element was selected to model both masonry walls and mortar interfaces, offering accurate description of complex behaviours like non-linear stress-strain relationships, cracking, and collapse mechanisms.

## ***ASDConcrete3D***

The *ASDConcrete3D* constitutive model was employed as the physical property for homogenized masonry walls, while *DamageTC3D* was used for mortar layer interfaces between units of the aggregate. These materials are computationally efficient thanks to the implemented *IM-PLEX* and autoregularization algorithms.

*ASDConcrete3D* is a *NDmaterial* object which represents the stress-strain relationship at gauss-points of a continuum element. It is a very recently developed material that has the useful feature of withstanding multiple failure mechanisms. Based on sophisticated plastic-damage mechanics, it can describe quasi-brittle material behavior, including nonlinear stress-strain behaviors, cracking, and crushing. While specifically designed for concrete, it also can be used to describe masonry (9).

The material's computational efficiency and stability are enhanced by the implemented *IMPLEX* integration scheme and secant constitutive tensor approach (39), crucial for analysing large-scale models under diverse load conditions. By using the principles of continuum damage mechanics, the constitutive model allows for the direct extraction of the stress tensor from the total strain tensor, eliminating the need for internal iterations at the constitutive level. This crucial feature not only ensures robustness in the analysis but also facilitates an efficient process, making it particularly suitable for large-scale models. The material allows the definition of two damage indices,  $d^+$  and  $d^-$ , which separately consider failure criteria for tension and compression.

STKO offers flexibility in customizing the material properties, allowing users to control between 1 and 9 parameters. Additionally, a user-defined option enables direct definition of the stress-strain relationship by placing custom vectors.

Given the relevance of this physical property in the research, a theoretical description of how this material computationally works has been described, considering the indications given by the software manual (62).

The state of stress and deformation of the last step ( $\bar{\sigma}_n, \epsilon_n$ ) are assumed to be known and the objective is to evaluate the update of the stress tensor  $\bar{\sigma}$  when a new level of deformation  $\epsilon$  is achieved. As a trial value, it is initially assumed that the material is working in the elastic regime, and by considering the stiffness tensor  $C_0$ , the new state of stress is defined as:



$$\tilde{\sigma} = \bar{\sigma}_n + C_0: (\epsilon - \epsilon_n) \quad [42]$$

By utilizing the positive principal stresses ( $\sigma_i$ ) and their corresponding principal directions ( $p_i$ ), the stress tensor can be divided into its positive and negative components.

$$\tilde{\sigma}^+ = \sum_{i=1}^3 \langle \tilde{\sigma}_i \rangle p_i \otimes p_i \quad [43]$$

$$\tilde{\sigma}^- = \tilde{\sigma} - \tilde{\sigma}^+ \quad [44]$$

From the trial effective stress tensor, two scalar values are defined: one related to tensile ( $\tau^+$ ) and one to compressive ( $\tau^-$ ) behavior using the damage surfaces.

$$\tilde{\tau}^+ = f(\tilde{\sigma}) = H(\tilde{\sigma}_{max}) \left[ \frac{1}{1-\alpha} \left( \alpha \tilde{I}_1 + \sqrt{3\tilde{J}_2} + \beta \langle \tilde{\sigma}_{max} \rangle \right) \frac{1}{\phi} \right] \quad [45]$$

$$\tilde{\tau}^- = f(\tilde{\sigma}^-) = \left[ \frac{1}{1-\alpha} \left( \alpha \tilde{I}_1 + \sqrt{3\tilde{J}_2} + \gamma \langle -\tilde{\sigma}_{max} \rangle \right) \right] \quad [46]$$

Where:

- $\tilde{I}_1$  is the first invariant of  $\tilde{\sigma}$
- $\tilde{J}_2$  is the second invariant of the deviator of  $\tilde{\sigma}$
- $\sigma_{max}$  is the maximum principal stress.
- $\alpha = \frac{4}{33}, \beta = \frac{23}{3}, \gamma = 3, \phi = 10$

By considering the equivalent plastic strain from the previous step ( $x_{pl,n}$ ), the stress scalars  $\tau^+$  and  $\tau^-$  can be transformed into their trial total-strain counterparts:

$$\tilde{x}^\pm = \frac{\tilde{\tau}^\pm}{E} + x_{pl,n} \quad [47]$$

Plasticity and damage cannot be recovered so it is required to update the strain:

$$\tilde{x}^\pm = \begin{cases} \frac{\eta}{\eta + \Delta t} x_n^\pm + \frac{\Delta t}{(\eta + \Delta t)} \tilde{x}^\pm & , \text{if } \tilde{x}^\pm > x_n^\pm \\ x_n^\pm & , \text{otherwise} \end{cases} \quad [48]$$

To account for damage irreversibility, the model defines a damage threshold using the variables  $r^+$  and  $r^-$ , which represent the largest highest values attained by the equivalent stresses,  $\tau^+$  and  $\tau^-$ , throughout the loading history for each time step.

$$r^+(t) = \max(\max \tau^+(s); f_t) \quad s \in [0, t] \quad [49]$$

$$r^-(t) = \max(\max \tau^-(s); f_{c0}) \quad s \in [0, t] \quad [50]$$

The plastic damage and cracking variables ( $d_{pl}$  and  $d_{cr}$ ) are derived from the hardening-softening law and new effective and nominal stress are evaluated as:

$$\bar{\sigma}^+ = (1 - d_{pl}^+) \tilde{\sigma}^+ \quad [51]$$

$$\bar{\sigma}^- = (1 - d_{pl}^-) \tilde{\sigma}^- \quad [52]$$

$$\bar{\sigma} = \bar{\sigma}^+ + \bar{\sigma}^- \quad [53]$$

$$\sigma = (1 - d_{cr}^+) \bar{\sigma}^+ + (1 - d_{cr}^-) \bar{\sigma}^- \quad [54]$$

In Figure 47, evaluation of the stress procedure is illustrated: before the elastic predictor is evaluated and then reduced by plasticity and damage in the uniaxial scenario.

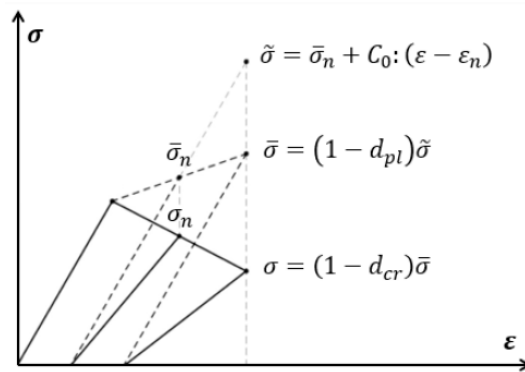


Figure 47: schematic representation of the elastic predictor followed by the plastic and damage correctors in a representative uniaxial case (62).

## DamageTC3D

DamageTC3D is the predecessor of the ASDConcrete3D (9). As well ASDConcrete3D, the speed and stability of DamageTC3D is thanks to IMPL-EX algorithm. The material also has an

autoregularization feature which allows an independence of the mesh size on the damage distribution.

The differences between them are related to the incapacity of *DamageTC3D* to withstand multiple failure mechanism. For instance, when a component fails in tension, the resistance is reduced in all directions, resulting in null compression resistance as well. This kind of mechanism describes very well the degraded mortar behavior present in existing structures (21). When the mortar achieves a failure of any kind shows a sort of disintegration and its resistance is drastically reduced for all the directions.

### ***IMPL-EX* algorithm**

The *IMPL-EX* algorithm combines the advantages of both explicit and implicit algorithms and to provide robustness to the analysis even in the presence of strong nonlinearities (63). It divides the calculation in two different calculation phases: first, the data is extrapolated explicitly, and then it is corrected implicitly.

During the global implicit stage, the trial stress tensor is computed for each element. In standard algorithms, the damage variables  $r^+$  and  $r^-$  are nonlinear functions of the trial effective stress tensor, leading to a non-linearity of the global problem. In the *IMPL-EX* algorithm, these damage variables are estimated from the previous time step using linear functions with the equation:

$$r_{n+1}^{\pm} = r_n^{\pm} + \frac{\Delta\tau_{n+1}}{\Delta\tau_n} (r_n^{\pm} - r_{n-1}^{\pm}) \quad [55]$$

The linear dependence of variables with respect to the strain allows for a more robust and rapid analysis, which can also be used for large models.

The *IMPL-EX* algorithm enhances computational efficiency in analysis, but it may produce results that are not always consistent with the desired outcomes. The explicit component of the algorithm converges towards a certain equilibrium path, which is not always guaranteed to be the exact solution. The error introduced by this approach can be minimized by incrementing the number of steps of the analysis. Therefore, it is essential for the user to always control the outputs and verify their reliability (39).

## Autoregularization tool

The autoregularization facilitates a mesh-size independent response (39). Due to material heterogeneity, structures have imperfections which behave as accumulation stress points and starting damage regions. For instance, if two elements ( $e_1$  and  $e_2$ ) are considered equal in geometry and material, and stress is equally increased on them, one of them may have larger imperfections and will reach failure earlier. However, the numerical model cannot determine which element will fail because imperfections are not considered. Furthermore, if  $e_1$  fails and exhibits softening behavior, the non-failed  $e_2$  will unload to maintain equilibrium, reaching the same stress value as  $e_1$ . This implies that the fracture energy showed by  $e_2$  (red area) will be much lower of  $e_1$ (green area), as shown in Figure 48.

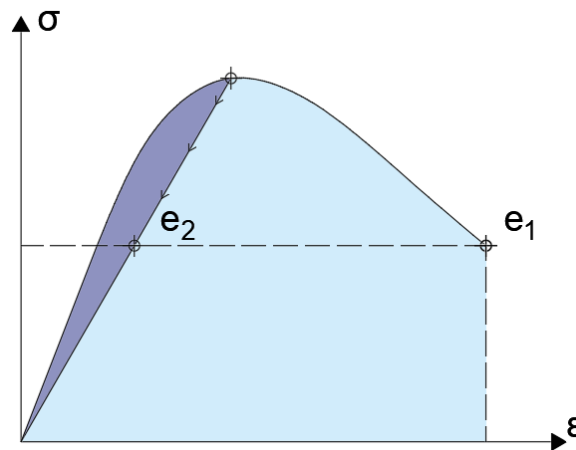


Figure 48. Energy dissipated by  $e_2$  and  $e_1$ .

The bigger the size of the elements, the more energy they will dissipate even if the fracture energy material ( $G_t$  and  $G_c$ ) is the same. So, it is intuitive that by changing the mesh these phenomena can drastically impact the material behavior. Using the autoregularization, the input fracture energy is divided by the element's characteristic length. So, it solved the model-reality mismatch that would cause a totally different result.

The evaluation of the tensile fracture energy is a fundamental aspect for modeling structures characterized by brittle materials with low tensile resistance such as mortar or masonry.

According to the FIB Model Code (64) the tensile fracture energy can be calculated as:

$$G_t = 0.073 f_{cm}^{0.18} \quad [N/mm] \quad [56]$$

Where  $f_{cm}$  is the compressive tensile strength of the masonry in MPa.

The determination of compressive fracture energy is performed using the guidelines outlined in (65).

$$G_c = 250G_t \quad [N/mm] \quad [57]$$

It's important to note that the two proposed formula [56] and [57] are originally related to concrete. Therefore, during masonry calibration, it is necessary to check its accuracy and suitability for masonry materials. The formulation provided by the rule code offers a reliable starting point.

## 5.2.2 Modelling of the slab

The floors of the masonry building can be modelled as either flexible or rigid, and this distinction significantly influences the distribution of inertial forces during earthquakes as discussed in Chapter 02. Flexible floors pose challenges in modelling realistic connections between floors and vertical walls, as well as determining how horizontal loads distribute throughout the structure. Conversely, rigid floors simplify the modelling process. In this case, horizontal loads can be applied directly to the central node of the floor, which is rigidly connected to other nodes within the floor.

In the present study, the slabs are considered infinitely rigid. Modelling a rigid diaphragm involves establishing an interaction between all nodes of the floor and associating it with a *RigidDiaphragm* condition. This condition imposes a rigid connection between all the floor nodes with respect to the floor's barycentre.

## Interactions and Rigid diaphragm

An interaction is a constraint that establish a relative relationship between DOFs of different nodes. Interactions serve as tools to connect nodes and elements within the structural model. When creating an interaction, it is necessary to define the master and slave nodes. Slave nodes are elements whose behavior is directly influenced by master nodes. To be effective, an interaction must be associated with a multipoint constraint (10). These types of constraints find application in various modeling scenarios, including Equal Degrees of Freedom (*EqualDOF*), rigid diaphragm, and rigid connection.

In the case of *EqualDOF*, it is possible to define which DOFs of the slave nodes are exactly like those of the master node. With a rigid link, the selected degrees of freedom (DOFs) in the designated nodes are constrained to move as a rigid body. *Rigid link* and *EqualDOF* show the same behavior if the master and slave nodes are at zero distance.

A rigid diaphragm constrains specific degrees of freedom of the slave nodes to move as if they are on a rigid plane with the node constrained, typically the center of gravity of the floor (Figure 49). A rigid diaphragm imposes a zero axial strain condition on the element connecting the restrained nodes and allows nodes to only translate along the x and y axes and to rotate about the z axis.

Interactions can also serve to connect various types of elements. This method proves advantageous when a more detailed mesh is necessary for a particular segment of the model, avoiding the necessity to refine the entire mesh uniformly and prevent an increasing computational demand. STKO assumes the same global mesh for all elements of the same type. The portion that requires a different mesh must be separated from the others with the assigned a global mesh. If necessary, the parts can then be reconnected using *EqualDOF*.

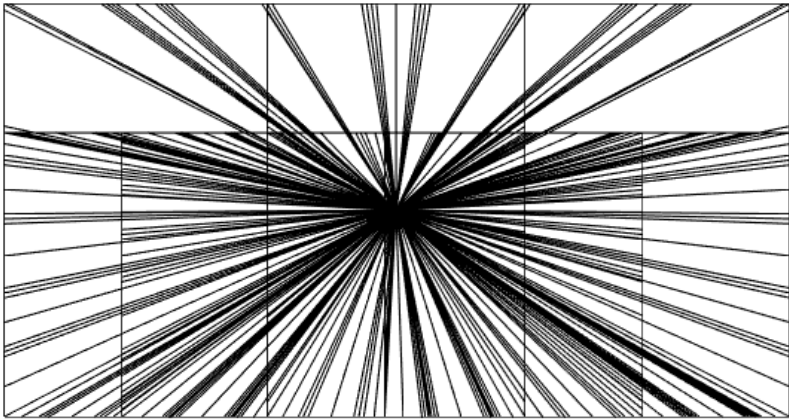


Figure 49: Rigid diaphragm example.

### 5.2.3 Modelling of the floor beams

The floor beams are modelled using elastic one-dimensional elements. The force-based numerical approach is implemented using the ForceBeamColumn element in OpenSees (10). To the beam elements are associate a linear elastic constitutive model.

To connect the beams to walls, an embedded node-to-element condition is modelled. In this approach, masonry panels are considered as master elements, while the beam's extreme nodes act as slave nodes. This interaction accounts for the connection between the beams and walls, allowing for a more accurate representation of the structural behaviour.

**Fiber section:**

In fiber section elements, the cross section of the beam can be discretized into fibers. At each fiber, a specific constitutive law can be associated to identify where fiber stresses reach the plastic limit. This method is particularly suitable for slender, flexure-dominated structures, as fiber elements primarily focus on capturing flexural behavior and may not fully account for shear failures (10).

These elements are suitable for capturing nonlinear behaviour and automatically detect the plastic limit for each fiber section. In Figure 50, an applicative example of a fiber section element is illustrated to model a reinforced concrete beam.

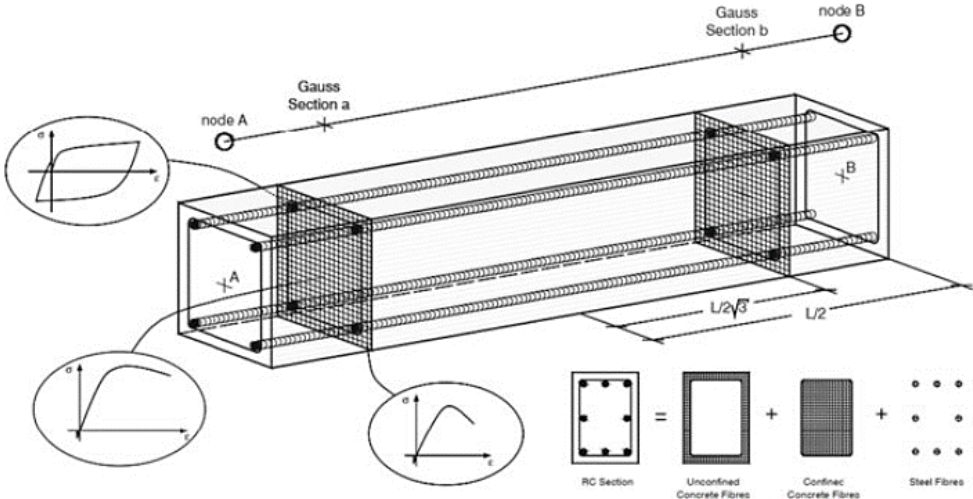


Figure 50: Fiber section element (66).

Non-linearity can be introduced with 1-D elements through either lumped or distributed plasticity (Figure 51). With lumped plasticity, plastic deformation is concentrated at specific points. While this method is computationally efficient, designers need to identify potential plastic hinge locations. This solution is more suitable for steel or reinforced concrete frames where plasticity positions are easily predictable (67).

Distributed plasticity is a more practical approach because the software can automatically handle plastic hinge development and consider axial force-bending moment interactions, despite a larger computation honor. While distributed plasticity can be considered using continuum finite element models, it is not practical for civil engineering practice due to the exaggerated computation demand (65). A way to obtain a sufficiently fast analysis is to have distributed plasticity with fiber section elements.

Two main types of elements can be used for this modeling approach: displacement-based elements (DBE) and force-based elements (FBE). DBEs are formulated in displacement fields, imposing a linear curvature distribution to approximate the nonlinear response. FBEs, starting from internal forces, solve equilibrium equations to determine deformation trends (68).

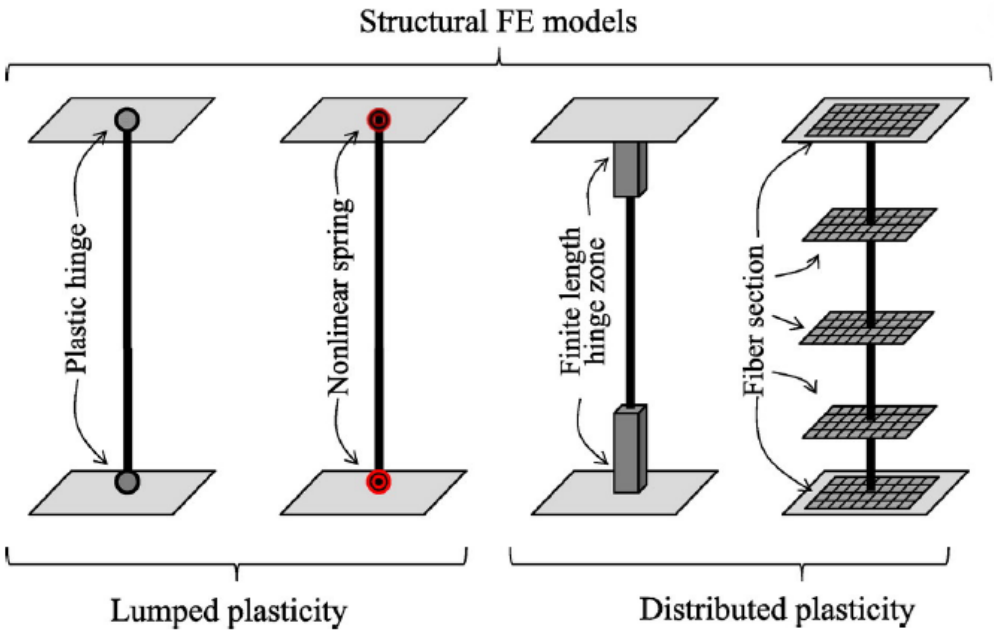


Figure 51: Lumped and distributed plasticity (69).

In the STKO software, the force-based approach is implemented by means of the *ForceBeamColumn element* (9). Although computationally more expensive respect DBEs, FBE generally improves global and local response without mesh refinement (70). The *ForceBeamColumn element* utilizes a simple linear transformation to translate beam properties from local to global coordinates, which makes the computation lighter.



## Connection beams-vertical walls

The connection between beam floor and vertical walls can be modelled through an interaction node-to-element, assuming masonry faces as master elements and beam ends as slave nodes. To this interaction is assigned *ASDEmbeddedNodeElement* condition, which is used to consider directly the degree of connection between the two components.

The *ASDEmbeddedNodeElement* establishes a connection between one constrained node and multiple retained nodes. In OpenSees, a Multi-Point constraint typically accommodates only one retained node. Therefore, this constraint was implemented as an Element (10). It enforces the constraint using the Penalty approach. This method adds large penalty parameters to the stiffness matrix to enforce constraints without altering the system size, making it suitable for any constraint type. The penalty parameters should be chosen to be effective but not too large to avoid instability. Typically, the penalty is set based on the typical stiffness magnitude of the model, increased by a factor of 8.

### 5.2.4 Modelling of the connection between orthogonal walls

The connection between orthogonal walls in masonry buildings can be modelled in two ways: either as being infinitely rigidly connected by merging the walls, or by introducing zero-length elements to accommodate a non-rigid connection.

When the walls are merged, they behave as a single element. Alternatively, different degrees of connection between orthogonal walls can be achieved by introducing interactions at the contact points of their extremities and associating them with zero-length elements. Adjusting the parameters of these zero-length elements directly affects the degree of connection between the walls.

#### **Zero length element:**

The ZeroLength element doesn't have any physical dimensions and it is used to link nodes at identical positions. As shown in the Figure 52, this element governs the interaction between restrained and constrained nodes, functioning similarly to a string (71). In STKO, multiple variations of zero-length elements are available, each with distinct properties. The *ZeroLength*

can be coupled with an *nDmaterial* property, which directly defines the force-deformation relation between nodes.

It is suitable for both 2D and 3D models, and it can determine which degrees of freedom are influenced by the introduction of the element. Additionally, it can be applied for the connection of different geometries.

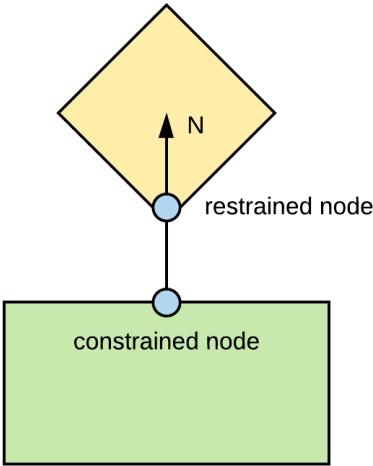


Figure 52: Zero length element structure (71).

### 5.2.5 Modelling of openings in masonry walls

Openings in masonry buildings have a lintel at the top. Lintels have the essential function of resisting the traction and bending action generated by the downward weight of the bricks placed above. Furthermore, lintels are very useful in serving to distribute the load of the wall above towards the sides of the opening, thus helping to support the weight of the structure above and increasing the resistance of the spandrels (15).

The lintel material properties are defined using *ASDConcrete3D*. Directly merging both masonry wall and lintel drastically increases the resistance of the spandrel. To avoid this overestimation, it is introduced a thin layer of mortar between the lintel and the wall (Figure 53), modelled with *ASDConcrete3D*.



Figure 53. Lintel geometry

## 5.2.6 Modelling of connection between units of the URM aggregate.

As introduced in chapter 3 of this work, the interfaces between units of an aggregate exhibit a complex behavior which depends on the tangential and normal forces developed. A possible way to accurately capture this behavior is by connecting adjacent walls considering the cohesion-friction law (7).

Traditionally, this is achieved by introducing zero-length elements to describe the interface (8). This study proposes an alternative approach consisting of modeling the connection as a mortar layer. This method allows for the use of any constitutive model to simulate the connection's behavior under tension and compression to account for both friction and cohesion, while reducing the convergence issues that zero-length elements may arise. Advantages and disadvantages of both approaches are explained below.

### Connection between units modelled with ZeroLength elements.

There are three main types of zero-length elements available in STKO to describe cohesive-friction behavior: *ZeroLengthContact3D*, *ZeroLengthContactASDimplex*, and *ZeroLength*.

The *ZeroLengthContact3D* element can describe both cohesion and friction making it ideal for modeling Mohr-Coulomb behavior at interfaces. However, it exhibits considerable instability, working effectively only for small-scale models, and limits the use of shell elements, which are fundamental for the adopted approach. This element uses as input the friction coefficient and the cohesion as a constant, neglecting the possible degradation (71).

On the other hand, utilizing a *ZeroLengthContactASDimplex* element simplifies and accelerates model execution, even in complex models. It offers the flexibility to assume an arbitrary

orientation in space and can handle models with curved surface contacts or distributed contacts along edges and surfaces. Despite these advantages, it does not consider cohesion.

To have cohesion-friction behavior, a hybrid approach can be adopted, using two zero-length elements simultaneously at the interfaces: a *ZeroLengthContactASDimplex* element manages friction, while a general *ZeroLength* element, associated with elastoplastic material properties, acts as an equivalent for cohesion. While this method offers computational efficiency, it does have a limitation: the *nDmaterial* associated with the zero-length element cannot differentiate between compression and tension behavior. As a result, this method is suitable only for scenarios where loads are applied monotonically in a single direction, and where it's known in advance whether the interface will be under compression or tensile stress. This limitation makes it unsuitable for dynamic or cyclic analyses, where loads are applied from different directions, and the interface must respond to both compression and tension.

### **Connection between units modelled with the introduction of an interface layer of mortar.**

Introducing a layer of mortar between units not only simplifies the modelling process but also allows for a representation of interconnection described by a cohesion-friction law, which varies between compression and tensile actions while also considering degradation. This mortar layer is modelled using shell elements, maintaining the same thickness as the masonry walls it connects. To account for the mortar's limited ability to resist multiple direction failures, it is associated with the material model *DamageTC3D*, and its behaviour is then characterized with a friction-cohesion law.

This approach eliminates the computational challenges that could arise from using zero-length elements and allows direct consideration of any constitutive model available in OpenSees, facilitating significant modifications to material behaviour.

Considering that the interface layer is very thin, and to ensure reasonable results while maintaining low computational costs, a separate mesh is created for the masonry wall and the mortar interface. Since STKO assumes a uniform mesh for all elements of the same geometrical entity, masonry walls and mortar layers are modelled with different geometrical entities (9), with a smaller mesh size applied to the interface compared to the one used for masonry walls.

The connection between the mortar layer and the masonry wall is established by introducing an *EqualDOF* interaction, which constrains all internal degrees of freedom except rotation around the axis perpendicular to the wall. Master nodes are designated as edges with the largest mesh size, while slave nodes are edges with the smallest size (Figure 54).

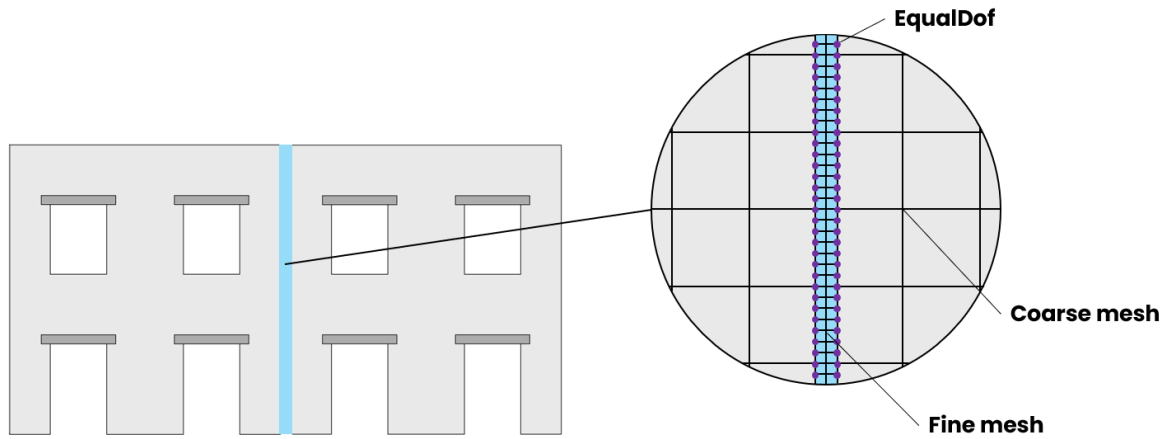


Figure 54: *EqualDOF* interaction between mortar layer and masonry wall.

The proposed solution preserves the connection between mortar and masonry walls while significantly reducing computational demands compared to using a single global mesh.

### 5.2.7 Modelling Choices Summary

The modelling strategy for the aggregate building employed a homogenized masonry approach, utilizing layered 2D shell elements. Specifically, *ASDShellQ4* was chosen as the 2D-shell element to represent the masonry walls, coupled with *ASDConcrete3D*. A thin layer of mortar was introduced between the lintel and the wall to accurately describe their behaviour and prevent over-resistance. All components, including the mortar layer, were modelled as shell elements alongside *ASDConcrete3D*.

The orthogonal walls of each unit were merged to establish rigid connections. Slabs were modelled as rigid diaphragms, with the barycentre of each floor serving as the master node. *ForceBeamColumn* elements were utilized for modelling floor beams, exhibiting perfectly elastic behaviour.

To address non-rigid interfaces between units, a mortar layer was introduced between the longitudinal walls of adjacent units, modelled as *ASDShellQ4* with *DamageTC3D*. The connection of the mortar with the walls was facilitated by introducing an *EqualDOF* condition.

The behaviour of the mortar was characterized using a friction-cohesion model, the details of which will be expanded upon in Chapter 06.

In the Figure 55, the adopted modeling choices are depicted.

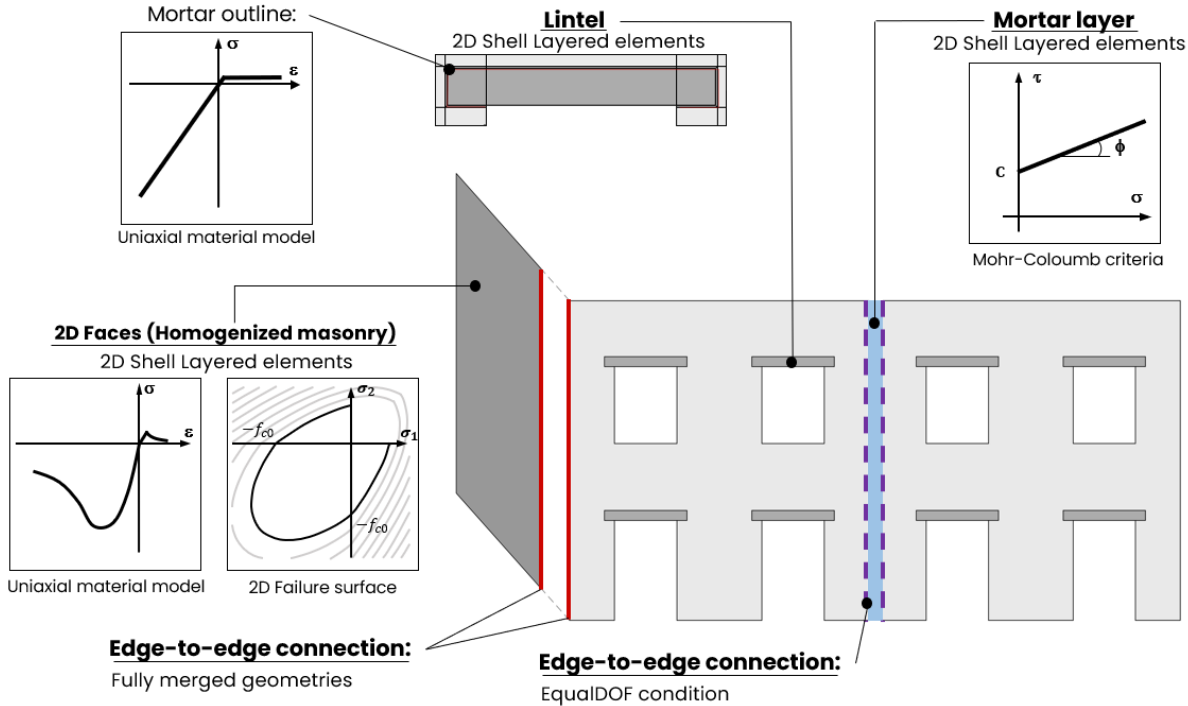


Figure 55: Modelling choices summary.

## 6. Characterization of the mortar connection

This section presents an investigation into the interface between units of an aggregate. The interface has been modelled by introducing a thin mortar layer, represented as a shell element with *DamageTC3D* as its material property. The properties of the introduced material were related to cohesion and friction, which are commonly used to determine the failure condition according to the Mohr-Coulomb law.

To characterize the mortars, a numerical model was constructed with a mortar layer sandwiched between two highly rigid blocks. The system was subjected to vertical stress, while horizontal forces were applied to the upper block. This setup facilitated the evaluation of the maximum tangential resistance of the mortar relative to the applied vertical load. Tests were conducted using four different types of mortar and at various levels of vertical stress, ensuring a comprehensive understanding of its performance under diverse axial load conditions.

### 6.1 Mohr-Coulomb law

The Mohr-Coulomb law is a failure criterion that describes the relationship between shear strength and normal stress applied to a certain body. Originally applied in soil mechanics, it has been extended to describe the behaviour of joined solids, such as masonry bricks and mortar. (72).

According to the Mohr-Coulomb Law, the shear stress ( $\tau$ ) along a potential failure plane within a material is a linear function of the normal stress ( $\sigma_n$ ) acting on that plane, as described by the equation:

$$\tau = C + \sigma_n \tan(\phi) \quad [58]$$

Where  $\tau$  is the shear stress,  $\sigma_n$  is the normal stress,  $C$  the shear strength of the material in the absence of normal stress,  $\phi$  is the angle of internal friction. In [58],  $\tan(\phi)$  can be denoted as  $\mu$ , which describes the material's resistance to shearing when under compression.

In analogy with soil mechanics,  $C$  can be defined as cohesion, representing the intercept on the shear stress axis, while  $\mu$  describes the slope of the failure envelope on a Mohr's diagram (Figure 56).

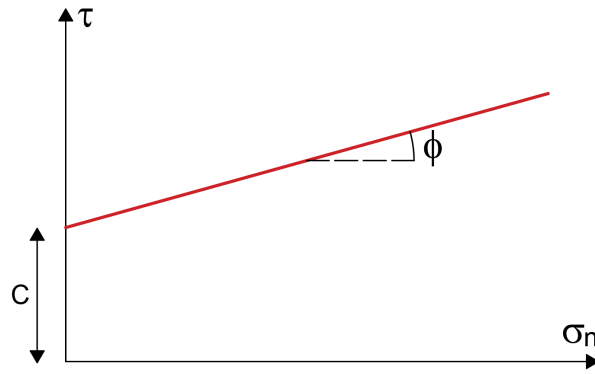


Figure 56: Mohr-Coulomb failure criteria.

## 6.2 Material properties of the different mortars considered

In this study, four types of mortars were utilized. The mortar's properties have been evaluated based on its compressive strength ( $f_{cp}$ ). Considering that the assumed compressive strength of the masonry is  $f_{cp} = 6.2 \text{ MPa}$  (further elaborated in chapter 6.3), mortars with lower compressive resistance were selected. Each type of mortar was assigned a specific name, which was used consistently throughout the document. Table 1 presents the properties of the four mortars considered.

Table 1: Properties of the considered mortar types.

Mortar denomination	m <sub>1</sub>	m <sub>3</sub>	m <sub>4</sub>	m <sub>6</sub>
<b>F<sub>cp</sub> [MPa]</b>	1.00	3.06	4.59	6.12
<b>f<sub>c0</sub> [MPa]</b>	0.70	2.14	3.21	4.28
<b>f<sub>cr</sub> [MPa]</b>	0.10	0.31	0.46	0.61
<b>E<sub>m</sub> [MPa]</b>	100	306	459	612
<b>E<sub>ms</sub> [MPa]</b>	50	153	230	306
<b>ε<sub>b</sub> [-]</b>	0.02	0.02	0.02	0.02
<b>f<sub>tm</sub> [MPa]</b>	0.04	0.11	0.16	0.21
<b>G<sub>t</sub> [N/mm]</b>	0.07	0.09	0.10	0.10
<b>G<sub>c</sub> [N/mm]</b>	18.25	22.32	24.01	25.29
<b>ν [-]</b>	0.15	0.15	0.15	0.15



The properties of the mortars were evaluated in relationship with their compressive strength  $f_{cp}$ . The elastic Young's moduli of the mortars were evaluated according to the empirical equation proposed by Kaushik et al. (73):

$$E_m = 100 f_{cp} \quad [59]$$

The secant elastic moduli at the peak strengths of the mortars  $E_m^s$  are evaluated as:

$$E_m^s = 0.5 E_m \quad [60]$$

From  $E_m^s$  it was evaluated the peak strains  $\varepsilon_b$ , that is:

$$\varepsilon_b = \frac{f_{cp}}{E_m^s} \quad [61]$$

By (73), the tensile strengths of the mortars  $f_{tm}$  are evaluated as:

$$f_{tm} = 0.035 f_{cp} \quad [62]$$

The fracture energy in tension  $G_t$  and in compression  $G_c$  were evaluated according the Fib Model Code (64):

$$G_t = 0.073 f_c^{0.18} \quad [63]$$

$$G_c = 250 G_t \quad [64]$$

The compressive elastic limits  $f_{co}$  and the compressive residual strengths  $f_{cr}$  of the mortars were assumed as:

$$f_{co} = 0,70 f_{cp} \quad [65]$$

$$f_{cr} = 0.10 f_{cp} \quad [66]$$

### 6.3 Model definition

The characterization of the various types of mortar was conducted through numerical simulations in STKO. A model was created consisting of three shell elements with identical dimensions, stacked on top of each other and merged (Figure 57). The shells, modelled with

*ASDShellQ4*, were characterized by a base size of 200 mm and a height of 30 mm. Furthermore, each shell was composed of 5 layers, each measuring 40 mm in thickness.



Figure 57: Mortar characterization model.

To the two external shell elements, a rigid-elastic material was associated with each layer, described in STKO using the *ElasticIsotropic* material with properties outlined in Table 2. The internal layer of mortar behaviour was described by the *DamageTC3D*, as well it is done in the interfaces between the units of the aggregate (chapter 7).

Table 2: Elastic material properties.

E [MPa]	210000
$\nu$ [-]	0.1

The bottom block was fixed at the base, while an *EqualDOF* condition was applied to the top part of the upper stiff block to restrict relative vertical displacement of the nodes, simulating perfect distribution of the vertical load on the element. On the upper block, a vertical *EdgeForce* and a horizontal force were applied, causing the block to move in the positive x-direction (Figure 58). The test was conducted under displacement control, with a horizontal displacement

target of 0.5 mm. The node located at the right extremity of the upper edge was utilized as the control node. The longitudinal reaction was recorded at the base of the lower block.

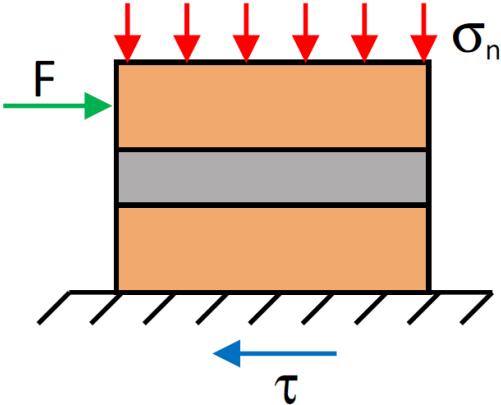


Figure 58: Mortar characterization test set-up.

It should be noted that STKO does not integrate the action across the thickness of shell elements. Therefore, the applied *EdgeForces* must be multiplied by the thickness of the shell elements, in this case 200 mm. It was assumed that, since the two external shell elements have negligible deformability compared to the central mortar shell, the entire reaction at the base can be attributed to the behaviour of the mortar. The tangential stress  $\tau$  of the mortar is defined dividing the base reaction for the base area.

The test has been repeated for the four mortar types ( $m_1$ ,  $m_3$ ,  $m_4$  and  $m_6$ ) considering different level of normal stress  $\sigma_n$  application. The designated levels of normal stress are illustrated in Table 3. A smaller range of normal stress was adopted for  $m_1$  case since it is unlikely that its compression strength is reached.

Table 3: Levels of normal stress applied to different types of mortar.

Mortar	$\sigma_n$ [MPa]					
$m_1$	0.0	0.1	0.2	0.3	0.4	0.5
$m_3, m_4, m_6$	0.0	0.2	0.4	0.6	0.8	1

The tangential stress of the mortar was plotted against the displacement of the control node for each case. In Figure 59 the results obtained for the four mortar types are collected.

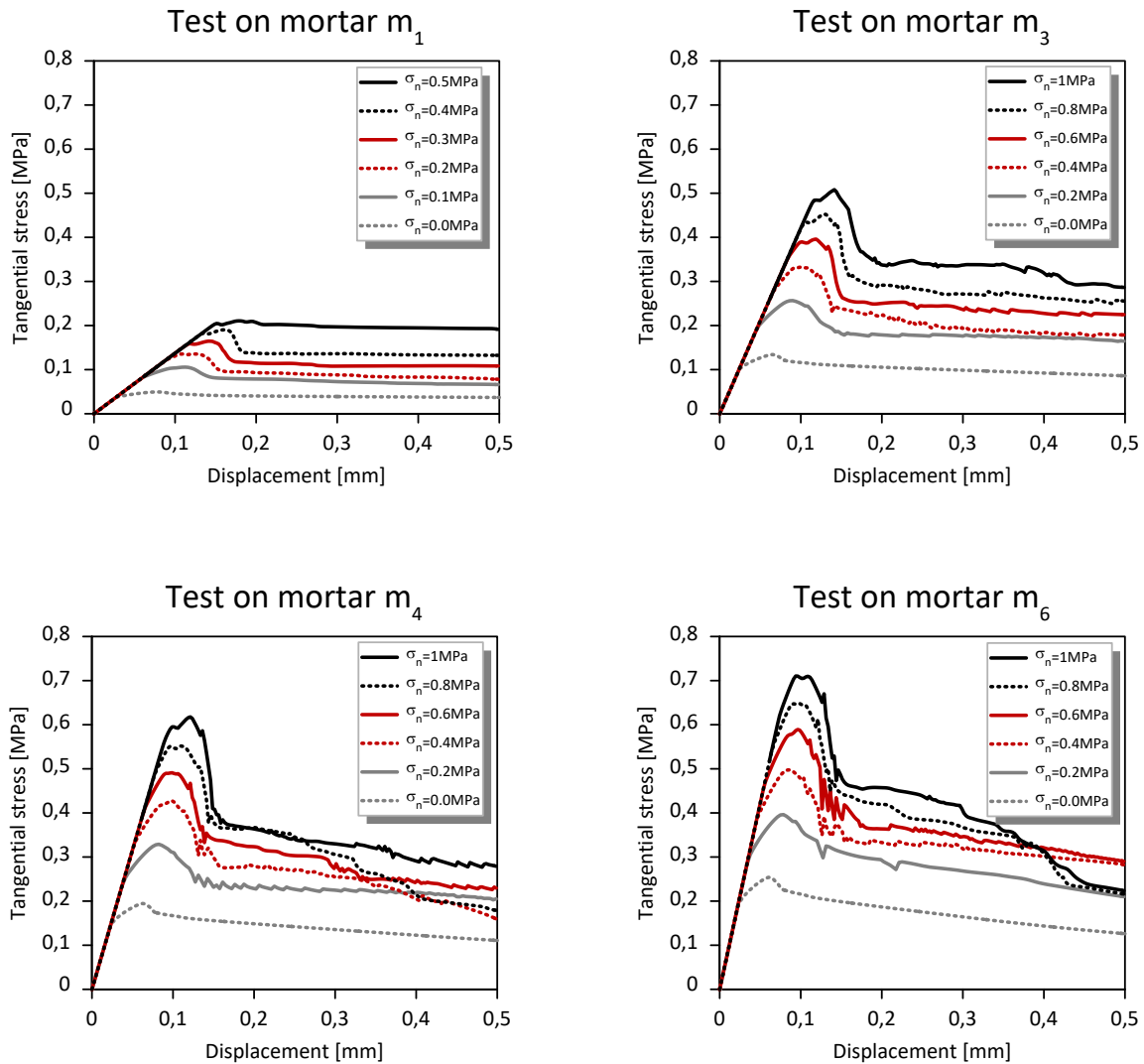


Figure 59: Results of Mortar Test.

The shear strength of mortars increases if a higher normal stress is applied to the mortar layer. As the vertical stress increases, the material's behavior becomes increasingly brittle. A mortar with higher mechanical properties, such as  $m_6$  compared to  $m_1$ , enhances the maximum shear strength of the material but it results in a more brittle behavior.

## 6.4 Mortar characterization.

Utilizing data from previous analyses, for each type of mortar under consideration, the maximum tangential stress exhibited by the mortar was plotted against the corresponding

vertical pressure applied during the respective test (Figure 60). The linear regression describes the failure domain of the mortar in a Mohr-Coulomb diagram.

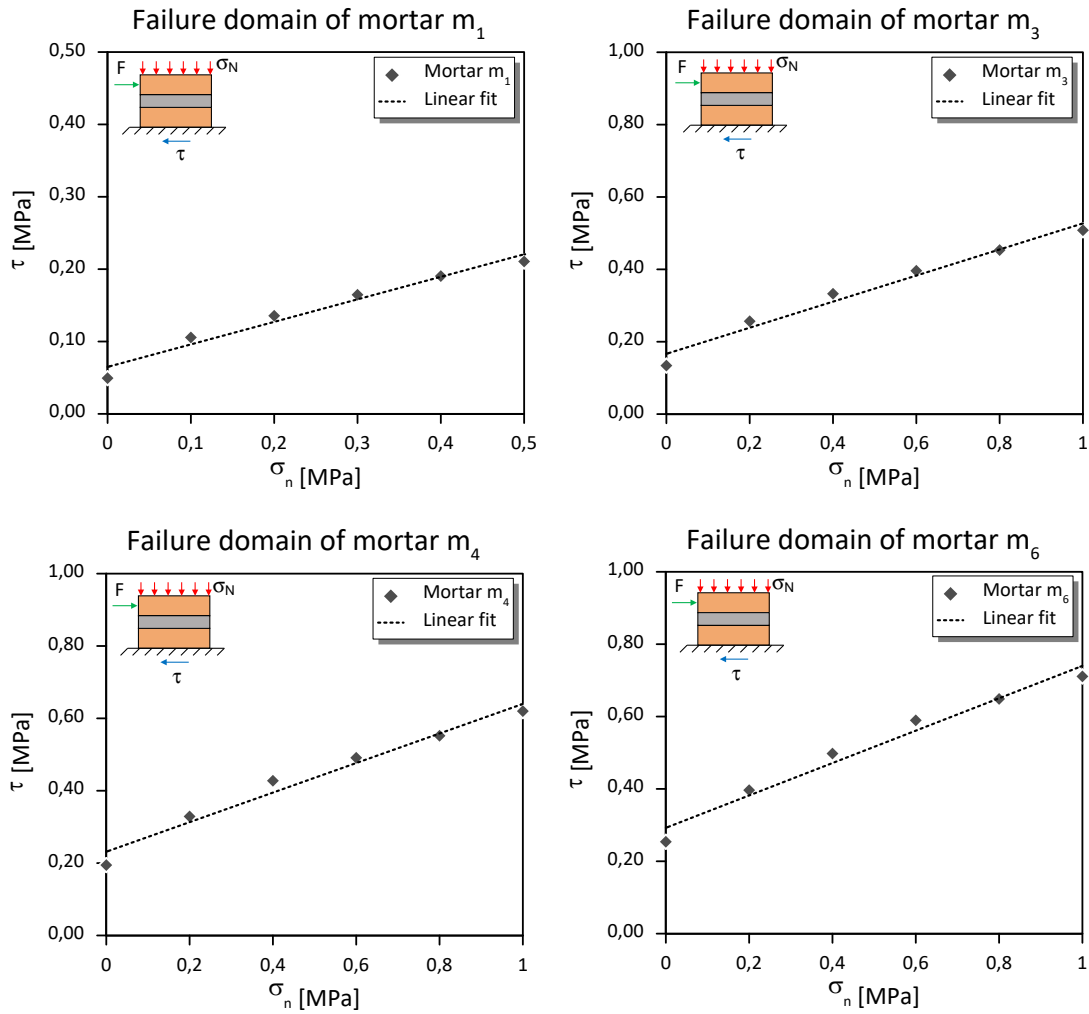


Figure 60: Mortar Failure Conditions.

Based on the results presented in Figure 60, the types of mortars can be characterized according to the Mohr-Coulomb law, with their cohesion ( $C$ ) and friction ( $\mu$ ) properties. The cohesion ( $C$ ) represents the intercept on the shear stress axis, while the friction ( $\mu$ ) corresponds to the slope of the envelop line (72). The summarized results are collected in Table 4.

Table 4: Friction and cohesion characterization of the mortars.

Mortar	$\mu$ [-]	$C$ [MPa]
m <sub>1</sub>	0.311	0.065
m <sub>3</sub>	0.361	0.167
m <sub>4</sub>	0.409	0.231
m <sub>6</sub>	0.448	0.292

Table 4 indicates that as the resistance properties of the mortar increase, both cohesion and friction also increase. This rise in both cohesion and friction can be linked to the higher compressive strength of the material, which derived in higher tensile strength and fracture energy based on the formulation proposed. Both cohesion and friction angle increase directly proportionally to tensile strength of the material. Mortar  $m_1$  exhibits the lowest mechanical properties, as evidenced by its lower values of friction angle and cohesion compared to other types of mortar. Conversely, mortar  $m_6$  demonstrates superior mechanical properties, with the highest levels of friction and cohesion. Meanwhile, mortars  $m_3$  and  $m_4$  occupy intermediate positions, with  $m_3$  exhibiting lower parameters than  $m_4$ .

The mortar characterized in this chapter serves as the material for the intermediate layer between the longitudinal walls of adjacent units, effectively simulating a non-rigid connection of units within the aggregate. Through a parametric analysis, utilizing the four distinct types of mortar, the study focuses on evaluating varying degrees of connection among the aggregate units.

# 7. Description of the aggregate case study

The primary objective of this study is to investigate the "aggregate effect" within masonry buildings by examining the various types of connections between the units and their impact on overall structural behaviour. The "aggregate effect" is a very complex subject because there are a multitude of parameters that can influence a building's performance (2). To maintain focus on the core task of this work, it was decided to work on an URM aggregate composed of 3 units geometrically similar. This decision was done to avoid the influence that dissimilar geometries and materials can have in the global response.

The units composing the aggregate were examined with different levels of interconnection: infinitely rigidly connected, isolated, and with an intermediate level of connection. The intermediate solution, referred to as "semi-connected," was implemented by introducing a thin layer of 3 cm between the longitudinal walls of adjacent units. At the interface layer, the four types of mortars introduced in Chapter 6 were considered in the parametric study:  $m_1$ ,  $m_3$ ,  $m_4$ , and  $m_6$

## 7.1 Geometry

The building is composed by 3 units, having each one 3 storeys. Each unit has a size of 8 m x 12.6 m x 11.2 m in respectively longitudinal, transverse, and vertical direction. Figure 61 depicts the geometry of the front and back wall of the aggregate.

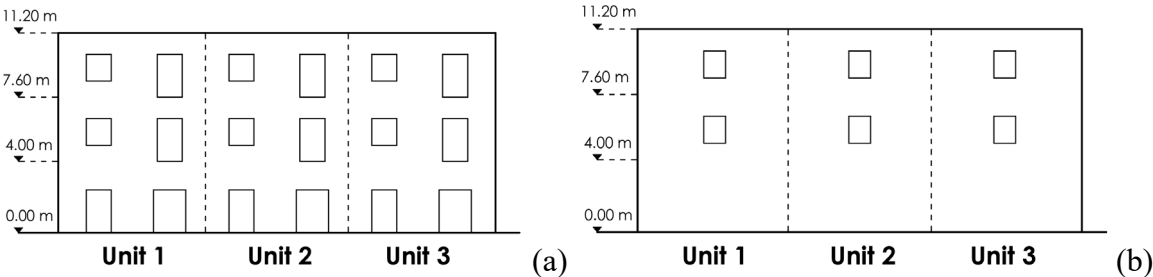


Figure 61: Reference aggregate's geometry: (a) Front wall; (b) Back wall.

By looking the building from the Figure 62, the units have been named as "unit 1" the unit on the left, "unit 2" the central one and "unit 3" the one on the right. The X-axis corresponds to the longitudinal direction of the building, which is aligned with the longer side. The Y-axis

represents the transversal direction, perpendicular to the longitudinal direction. Finally, the Z-axis denotes the vertical direction, pointing upwards from the ground.

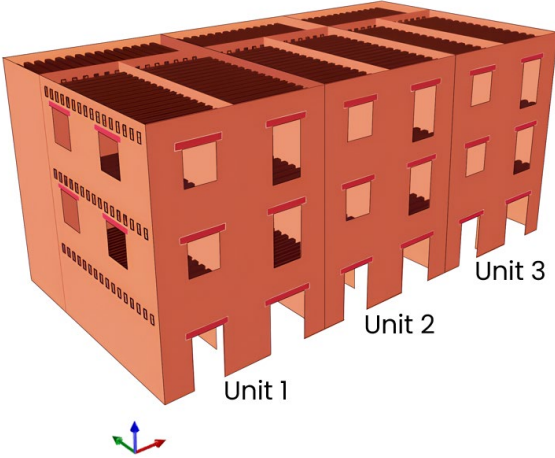


Figure 62: Units in the aggregate.

In the longitudinal direction, the aggregate has 3 walls which have been called "front wall", "central wall" and "back wall" (Figure 63, Figure 64, Figure 65). The back wall has openings placed symmetrically while the others do not. The front wall is the one with the greatest number of openings.

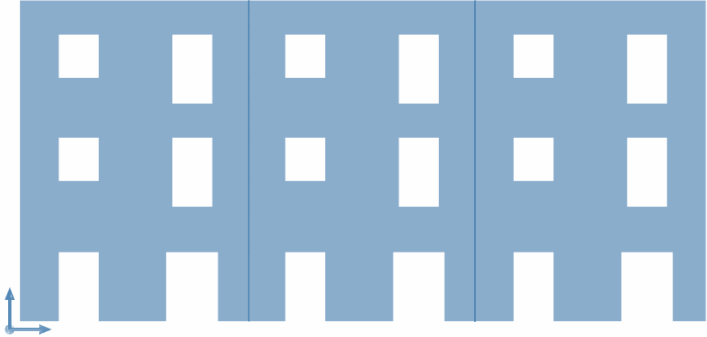


Figure 63: Front wall.

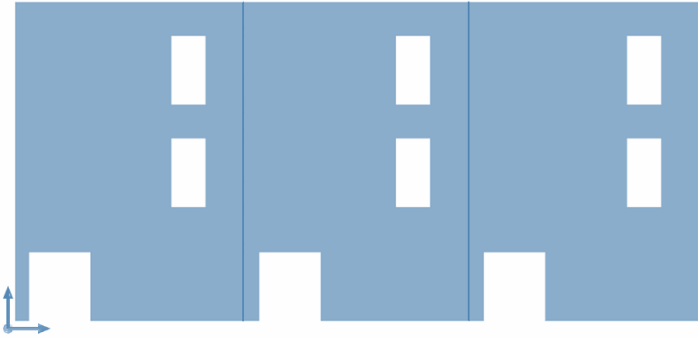


Figure 64: Middle wall.



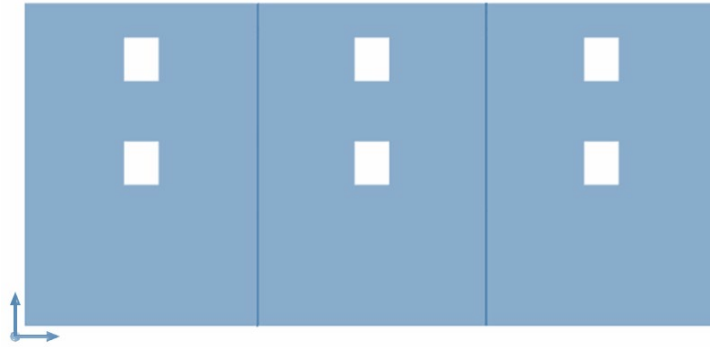


Figure 65: Back wall.

In the transverse direction, the external walls of the aggregate and the internal wall of each unit have openings, while the interface walls between each unit are completely closed, as shown in Figure 66.

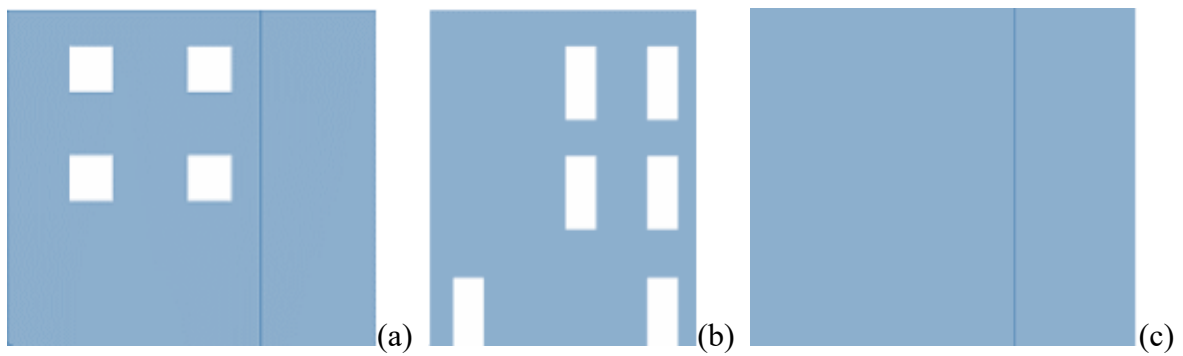


Figure 66: a) External walls; b) internal walls; c) U1-U2 and U2-U3 shared walls.

The floor beams were arranged in accordance with the orientation of the floor slab showed in Figure 67.

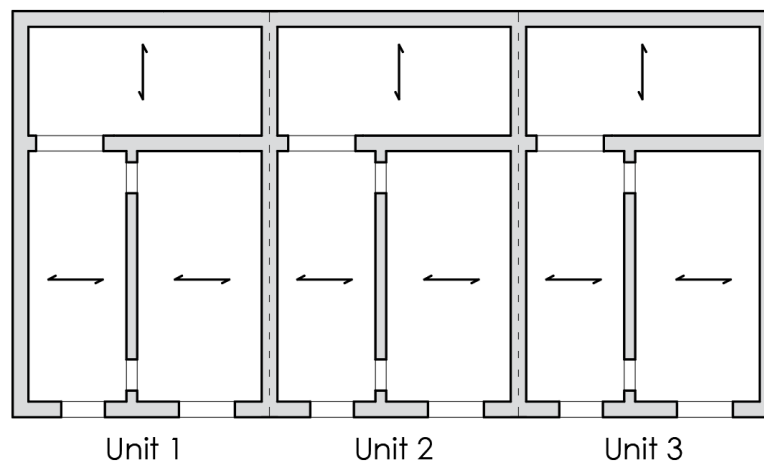


Figure 67: orientation of slabs.

Between the front and intermediate walls, the beams were placed longitudinally at each floor and were assumed to be embedded into each transverse wall. Only on the third floor, between the back and middle walls, the beams are arranged transversely. In this space, at the first and second floor the presence of the room staircase is assumed. All external and internal walls between the units have a thickness of 50 cm on the first 2 floors and 40 cm on the highest one, while the other walls have a thickness of 35 cm on the first floor and 30 cm on the other two floors. Additional details on the dimensions of the building are provided in the appendix A.

## 7.2 Numerical models

Three different numerical models have been realized to consider the different degree of connection between the units of the aggregate.

The scenario where units are connected infinitely rigidly is referred to as "Fully-Connected," often abbreviated as "FC" in charts. In this configuration, the three units are merged, with adjacent units sharing the same wall at their interface (Figure 68a). This model is characterized by a rigid diaphragm, which constrains all the nodes of the three merged units at the level of each floor (Figure 68b).

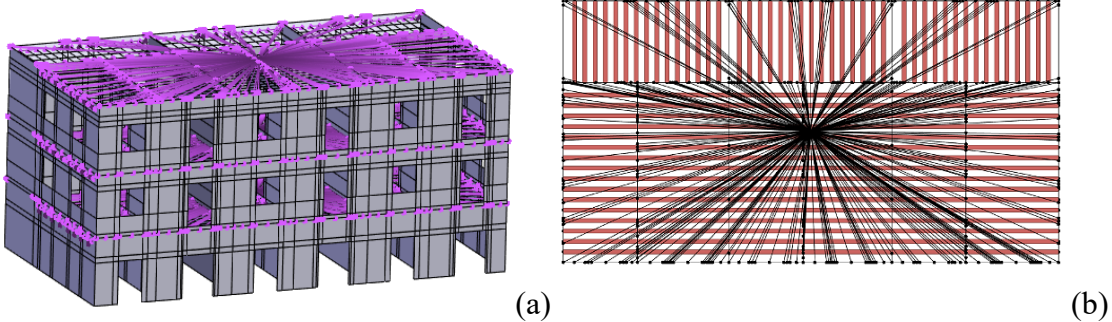


Figure 68: (a) Fully-Connected aggregate (b) Rigid diaphragm.

The units have also been modelled separately to analyse their behaviour as isolated from other units. Each unit features four external walls and a rigid diaphragm at each floor (Figure 69). Specifically, in the Fully-Connected case, there is only one interface wall between the units, while in the isolated case this wall is considered for both adjacent units.

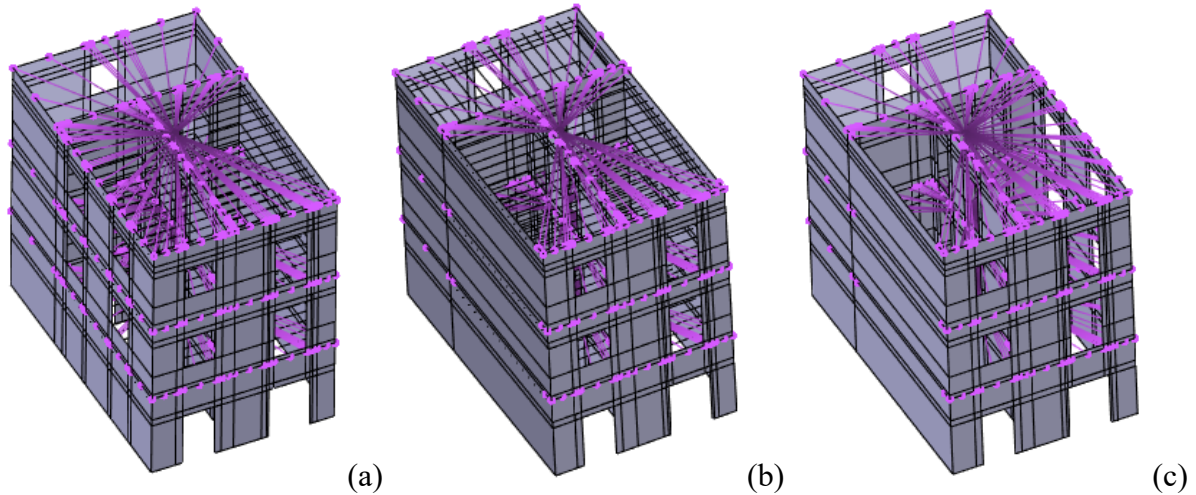


Figure 69: isolated units: (a) unit 1; (b) unit 2; (c) unit 3.

To assess the non-rigid connection between units, a distinct model was constructed. The three units were individually modelled as the isolated case but interconnected by introducing a mortar layer at their interfaces (Figure 70a). This model was termed "Semi-Connected" and was frequently abbreviated as "SC" in charts. For each floor, there are individual rigid diaphragms dedicated to each unit (Figure 70b). The mortar layer, with a thickness of 3 mm, was applied only between the longitudinal walls of the adjacent units. To account for varying degrees of non-rigid connection between units, four different types of mortar were used at the interface layers, whose properties have been explored in Chapter 6.

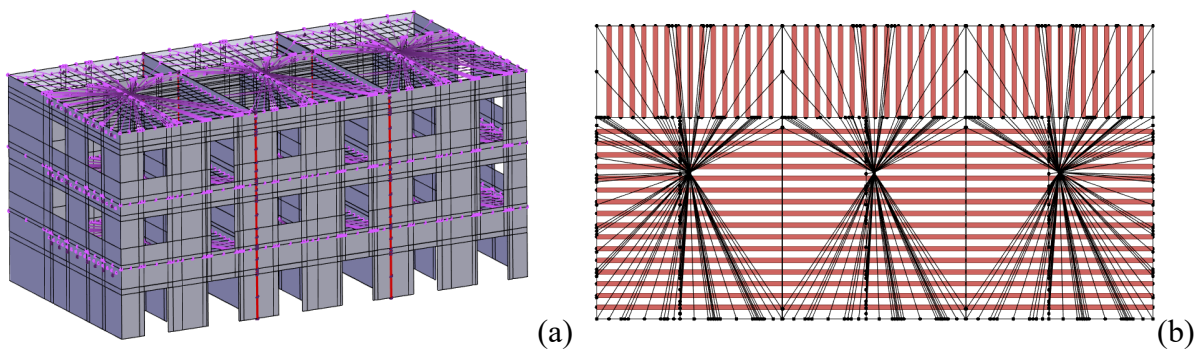


Figure 70: Semi-Connected aggregate.

In this case, between the units there are no connecting longitudinal beams. The connection is done exclusively by the mortar layers. The layer of mortar, which was characterized by a finer mesh compared to the masonry walls, was connected to the units using an *EqualDOF* interaction. The decision to avoid associating both the *EqualDOF* and the *RigidDiaphragm* to the same nodes was made due to the limitation of the default constraint handler of the modal analysis, which is unable to consider more than one interaction simultaneously.

### 7.3 Masonry material properties calibration

The masonry material properties utilized in this work were derived from the calibration performed in the study "Seismic response of different masonry building aggregate configurations by a refined FE Model" (74). The study investigated the beneficial impact of the aggregate effect in URM units by creating a model in STKO based on the homogenized masonry technique. Masonry calibration was conducted numerically to replicate experimental tests performed on an existing masonry building analysed at the University of Pavia (75).

The experiment was conducted on a two-story rectangular masonry building, as depicted in the Figure 71, with dimensions of 6.4 meters in height, 6 meters in length, and 4.4 meters in width. Each wall of the building had a thickness of 250 mm.

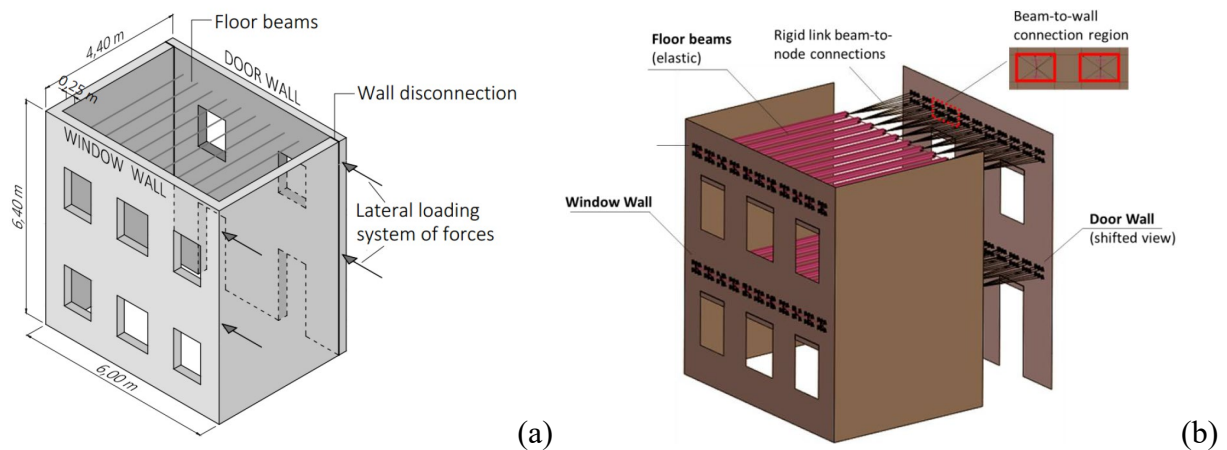


Figure 71: (a) Experimental cyclic test; (b) 3D numerical model (74).

The Door Wall was connected to the Window Wall through transversal floor beams made of steel, designed to simulate a realistic flexible floor. The building was analyzed under a series of cyclic test runs using a uniform load profile derived from previous dynamic tests on a twin building. The results of the test are reported in figure 72.

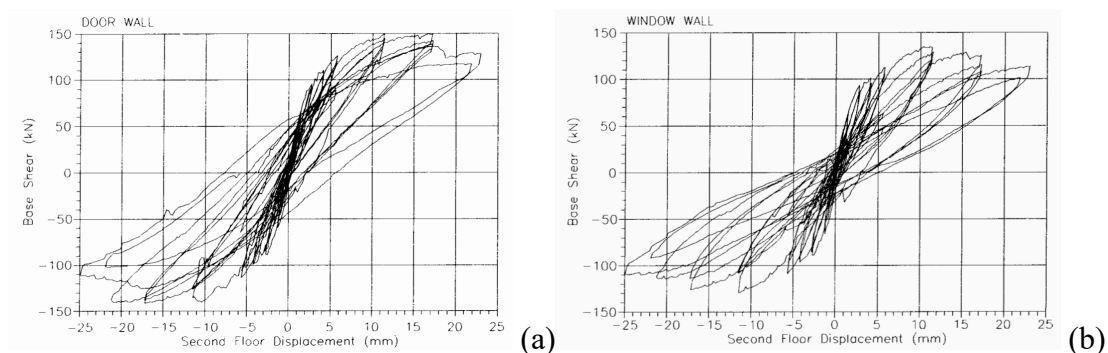


Figure 72: Results from experimental test: a) Door Wall; b) Window Wall (75).

The authors of (74) replicated the masonry building in STKO, constructing a 3D model that utilizes a homogenized masonry approach through layered 2D shell elements. The masonry walls were modeled using the *ASDShellQ4* element and the *ASDConcrete3D* constitutive model, consistent with this study.

The numerical test consisted in conducting two pushover analyses using a displacement control: one pushing the front wall and another on pushing the back wall. The calibration process, particularly concerning the tensile strength and fracture energy, was a complex procedure, as it required meticulous control over crack propagation. Figure 73 shows the comparison between the envelope of the experimental cyclic test and the results obtained from the pushover analyses for both walls.

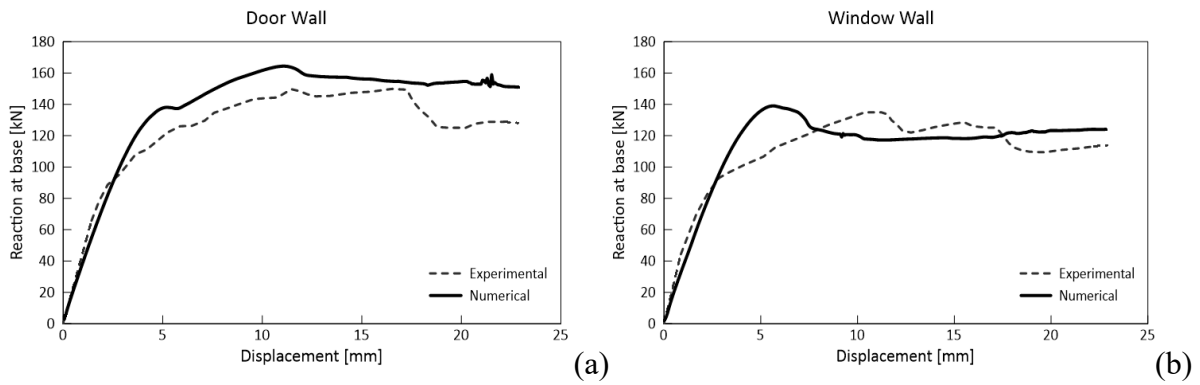


Figure 73: Experimental and numerical curves: (a) Door Wall; (b) Window Wall (74).

The parameters obtained from the calibration of the masonry, which are presented in Table 5. The material parameters of the present study are taken from the suggested in (74), as the current modelling approach is consistent with the study. These parameters are reported in Table 5.

Table 5: masonry physical properties calibration from study (74).

$f_t$	$f_{cp}$	$G_t$	$G_c$	$E$	$\nu$
[MPa]	[MPa]	[J/m <sup>2</sup> ]	[J/m <sup>2</sup> ]	[MPa]	[-]
0.15	6.2	70	14000	1490	0.2

Figure 74 displays the constitutive model of masonry.

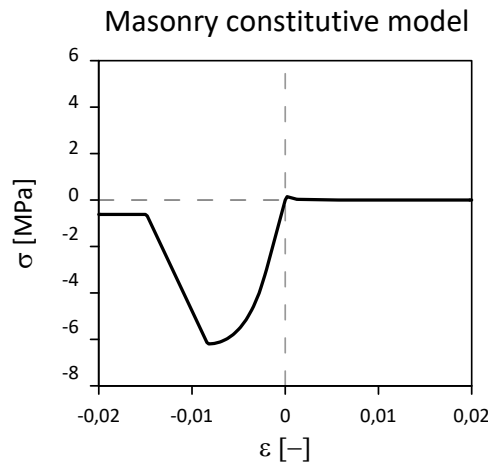


Figure 74: Masonry constitutive model used in this study.

## 7.4 Material properties

In this research, the same parameters of masonry shown in Table 5 were assumed. The assumed material properties of the masonry can be associated with the classes of "Squared block masonry" outlined in Table C8.5.1 of the circular of the NTC (76).

Table 6: Masonry categories according to Tab C8.5.1 of NTC2018 (76).

**Tabella C8.5.1** -Valori di riferimento dei parametri meccanici della muratura, da usarsi nei criteri di resistenza di seguito specificati (comportamento a tempi brevi), e peso specifico medio per diverse tipologie di muratura. I valori si riferiscono a:  $f$  = resistenza media a compressione,  $\tau_0$  = resistenza media a taglio in assenza di tensioni normali (con riferimento alla formula riportata, a proposito dei modelli di capacità, nel §C8.7.1.3),  $f_{v0}$  = resistenza media a taglio in assenza di tensioni normali (con riferimento alla formula riportata, a proposito dei modelli di capacità, nel §C8.7.1.3),  $E$  = valore medio del modulo di elasticità normale,  $G$  = valore medio del modulo di elasticità tangenziale,  $w$  = peso specifico medio.

Tipologia di muratura	$f$	$\tau_0$	$f_{v0}$	$E$	$G$	$w$
	(N/mm <sup>2</sup> )	(N/mm <sup>2</sup> )	(N/mm <sup>2</sup> )	(N/mm <sup>2</sup> )	(N/mm <sup>2</sup> )	(kN/m <sup>3</sup> )
	min-max	min-max		min-max	min-max	
Muratura in pietrame disordinata (ciottoli, pietre erratiche e irregolari)	1,0-2,0	0,018-0,032	-	690-1050	230-350	19
Muratura a conci sbozzati, con paramenti di spessore disomogeneo (*)	2,0	0,035-0,051	-	1020-1440	340-480	20
Muratura in pietre a spacco con buona tessitura	2,6-3,8	0,056-0,074	-	1500-1980	500-660	21
Muratura irregolare di pietra tenera (tufo, calcarenite, ecc.)	1,4-2,2	0,028-0,042	-	900-1260	300-420	13 ÷ 16(**)
Muratura a conci regolari di pietra tenera (tufo, calcarenite, ecc.) (**)	2,0-3,2	0,04-0,08	0,10-0,19	1200-1620	400-500	
Muratura a blocchi lapidei squadriati	5,8-8,2	0,09-0,12	0,18-0,28	2400-3300	800-1100	22
Muratura in mattoni pieni e malta di calce (***)	2,6-4,3	0,05-0,13	0,13-0,27	1200-1800	400-600	18
Muratura in mattoni semipieni con malta cementizia (es.: doppio UNI foratura ≤40%)	5,0-8,0	0,08-0,17	0,20-0,36	3500-5600	875-1400	15

(\*) Nella muratura a conci sbozzati i valori di resistenza tabellati si possono incrementare se si riscontra la sistematica presenza di zeppe profonde in pietra che migliorano i contatti e aumentano l'ammorsamento tra gli elementi lapidei; in assenza di valutazioni più precise, si utilizzi un coefficiente pari a 1,2.

(\*\*) Data la varietà litologica della pietra tenera, il peso specifico è molto variabile ma può essere facilmente stimato con prove dirette. Nel caso di muratura a conci regolari di pietra tenera, in presenza di una caratterizzazione diretta della resistenza a compressione degli elementi costituenti, la resistenza a compressione  $f_{pu}$  può essere valutata attraverso le indicazioni del § 11.10 delle NTC.

(\*\*\*) Nella muratura a mattoni pieni è opportuno ridurre i valori tabellati nel caso di giunti con spessore superiore a 13 mm; in assenza di valutazioni più precise, si utilizzi un coefficiente riduttivo pari a 0,7 per le resistenze e 0,8 per i moduli elastici.

As described in chapter 6, four different typologies of interface mortar in between the units were considered, whose properties were described in Table 1. The four mortars have been modelled with *DamageTC3D*.

The floor beams were assumed to be made of wood with dimensions of 40 cm x 20 cm. They were considered to exhibit elastic behaviour, and their properties are provided in Table 7. Additionally, Table 8 describes the embedded condition settings of the connections between walls and beams.

Table 7. Wood physical properties.

E [MPa]	10000
G [MPa]	300

Table 8: Embedded settings

Penalty factor	5e+07
Constrain rotations	Yes

Lintel material properties were chosen assuming a unique solid brick, as generally observed for historical constructions (15). Material properties are reported in Table 9.

Table 9: Lintel physical properties.

$f_t$	$f_{cp}$	$G_t$	$G_c$	$E$	$\nu$
[MPa]	[MPa]	[J/m <sup>2</sup> ]	[J/m <sup>2</sup> ]	[MPa]	[-]
1.6	16	120	30000	9600	0.2

In the study, the mortar surrounding lintels was defined differently from the mortar used as an interface between units. Specifically, the mortar around the lintel needed to behave purely elastically under compression and have no strength under tension to capture the sliding of the lintel. To achieve this specific behaviour, a customized constitutive model was introduced using the user-defined settings available for the *ASDConcrete3D* model, described in Table 10.

Table 10. User-defined mortar parameters.

Elasticity	$E$ [MPa]	1490
	$\nu$ [-]	0.2
Tension	$T_e$	[0 ; $6.71141 \cdot 10^{-7}$ ; 1]
	$T_s$	[0 ; 0,001 ; 0,001]
	$T_d$	[1 ; 1 ; 1]
Compression	$C_e$	[0 ; 1]
	$C_s$	[0 ; 1490]
	$C_d$	[1 ; 1]

Figure 75 displays the constitutive model of the mortar used as interface for lintels.

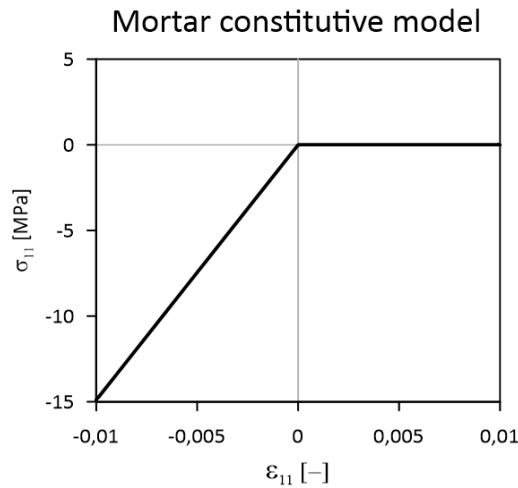


Figure 75: Mortar constitutive model.

## 7.5 Loads, masses and conditions

Vertical loads were considered by accounting for the weight and applied loads on floor slabs, stairs, and walls. Loads were applied to the beams as *EdgeForce* and to the walls as *FaceForce*. STKO automatically converted these distributed forces into nodal loads.

The load definitions were selected to align with typical loads for buildings of this type. Each floor beam was loaded by an *EdgeForce* of  $2.5 \text{ kN/m}$ . The self-weight of masonry walls was computed as the specific weight of  $\gamma_m = 17 \text{ kN/m}^3$  multiplied by the thickness of the walls.



In stair areas, although the stairs were not modelled, an extra load of  $4 \text{ kN/m}^2$  due to stair usage, along with the weight of the stairs themselves, was included. These loads were applied as *EdgeForces* at the edges of transversal walls, both at the beginning and end of the staircase.

All vertical loads were also considered as masses for dynamic analysis. Since OpenSees distinguishes between masses and loads, self-weight loads of elements were applied independently of the mass (10). Masses were applied as *FaceMass* for the walls and *EdgeMass* for the edges.

The base of all the walls of the aggregate has been completely fixed: all degrees of freedom of both rotation and displacement have been constrained using the *fix* condition in STKO.

## 7.6 Analysis settings

In this section, the analyses carried out are explained, focusing on the computational settings. Three analyses were conducted: modal analysis, non-linear static analysis, and dynamic analysis. Each analysis was carried out separately, following a preliminary vertical analysis.

### Vertical analysis

In the vertical analysis, vertical loads and self-weight loads are applied. Loads were applied linearly for each step. The vertical analysis approach was consistent in all model analyses and was performed in all simulations as the first analysis. The following describes the differences between the methods used for single-processor and multiprocessor setups.

In OpenSees, all degrees of freedom are numbered, and the *DOF\_Numberer* rennumbers them to ensure sparsity in the global stiffness matrix, reducing computational costs (10). For single processor analysis, the *reverse Cuthill-McKee (RCM)* algorithm was used, while for parallel analysis, the *parallel reverse Cuthill-McKee* algorithm.

The system solver, necessary for solving the differential equations, converts them into a linear system of equations. *UmfPack* is used for uniprocessor analysis, while *Mumps* is employed for parallel processors. Because of the complexity of the problem and the need to handle nonlinear equation systems, the Krylov-Newton method was adopted.

To ensure result reliability, a convergence test was performed using the norm displacement increment test with a tolerance of 0.0001. A Load Control integrator with a time series definition was used to regulate load increments over time. A linear time series definition was associated with the vertical analysis, incrementing the load factor linearly at each time step. The time step required in OpenSees is provided by STKO as:

$$timestep(dt) = duration/numIncr \quad [67]$$

Where duration is related to the total analysis and *numIncr* is the number of increments required. In static analysis using Load Control with a linear time series, the timestep can indeed be considered as the load multiplier (9).

After the first vertical analysis, a *wipeAnalysis* deletes all numerical configuration obtained from previous analyses.

## **Modal analysis**

In the modal analysis, the examination focused on the first 10 eigenmodes of each model, evaluating the respective vibration frequency, mode trend, and participation mass factors. A custom code facilitated the direct extraction of floor mass and the fundamental vibration mode.

For modal analysis in STKO, the analysis restricted to a single-processor setup. This requirement implies vertical analysis also cannot use multiprocessing.

The *genBandArpack* solver employed for eigen analysis doesn't offer any customization for the constraint and numbering options and the default options must be adopted. This restriction can affect the validity of model, necessitating to check for any computational issues. For instance, the default constraint handler couldn't model *RigidDiaphragm* and *EqualDOF* conditions applied to same nodes.

## **Pushover analysis**

The Pushover analysis benefited from parallel processing to significantly reduce computation time. The analysis was conducted under displacement control, with a target displacement of 35

mm. An adaptive time step improved analysis convergence, automatically reducing the step if the convergence isn't achieved.

The application of Pushover analyses varied depending on the type of model under study. For isolated units, the control node was assumed to be the barycentre of the third floor, while for Fully-Connected units, it was the barycentre of the central unit on the third floor. In both cases, this control node is the master node of the rigid diaphragm which connects all other points on the floor.

In the case of semi-connected units, there are three rigid diaphragms on the third floor, one for each unit. This case was critical due to the possibility of mortar failure and subsequent detachment of units. In this scenario, placing the control node at the barycentre of certain unit during analysis can lead to convergence issues with the other two units. For instance, during a positive pushover with the control node applied to the barycentre of the aggregate, which coincides with the second unit, unit 2 pushes toward unit 3 and pulls unit 1 through the mortar connection. Among the three units, Unit 3 experiences greater displacement and is the first to reach failure. Once unit 3 fails, unit 2 can continue to move only if unit 3 deforms further. However, Unit 3's deformation may become unsustainable and cause convergence issues. This behaviour is inherent to the pushover analysis. As soon as units become disconnected, since the control node is geometrically connected to the central unit, two things occur: i) the leeward unit (for a positive pushover, unit 3) will have a reduced stiffness due to the higher damage induced by the aggregate effect and therefore the displacement reached will be much higher; and ii) the windward unit (for a positive pushover, unit 1) will unload. In terms of displacement, this means that the leeward unit will have a greater displacement than the control node for a same time step and, therefore, the reaction measured in that unit is not representative, exhibiting an "apparent" ductility. Therefore, considering only unit 2 barycentre as the control node would not be representative of the behaviour of the other two units. Moreover, this exaggerated displacement of the unit causes severe damage, which lead to convergence issues.

To surpass the issue, it was decided to conduct additional analyses by considering as control node the barycentre of the third floor of each unit, one at a time, as shown in Figure 76. When studying the base reaction of a specific unit, the control node is positioned in the centre of gravity of the third floor of that unit. This necessitated conducting three pushovers in the positive direction and three in the negative direction for each type of mortar considered.

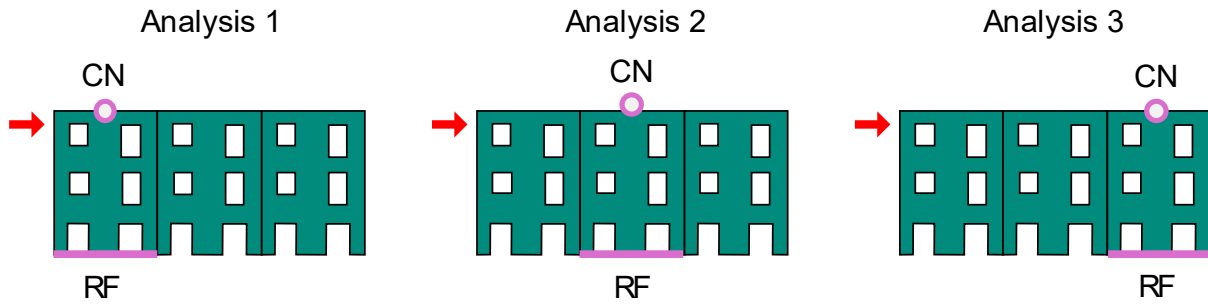


Figure 76: Control node position for each analysis.

As discussed in the chapter 4, the distribution of the horizontal loads in the nonlinear static analysis influences the dynamic response of the building. Considering that in this work the first mode of vibration predominantly mobilized mass in the x-direction, the modal distribution of horizontal loads was assumed the most appropriate.

Similar to the vertical analysis, *Parallel Reverse Cuthill-McKee* and *Mumps* were used as numberer and system solver respectively. Convergence was assessed using the *Krylov-Newton* method as solution algorithm. The *Norm-Increment Displacement* criterion, with a tolerance of 0.0001 and a maximum of 30 iterations for Fully-Connected and isolated cases. While for the “Semi-Connected” case, the number of iterations was occasionally increased to 100 to advance the analysis as much as possible. The penalty method, with penalty factors of  $10^{14}$ , was used as the constraint handler. Furthermore, a parallel displacement increment test was employed for the integrator to enhance efficiency.

## Non-linear dynamic analysis

The dynamic analysis is a transient analysis necessitating the application of masses to model components to account for inertial forces. The analysis evaluates the actual inertial forces induced by ground acceleration corresponding to a real earthquake event by solving the equation of motion. The ground motion data utilized for this purpose was the accelerogram (Figure 77) recorded by the L’Aquila – V. Aterno – Colle Grilli station in 2009, specifically in the North-South direction.

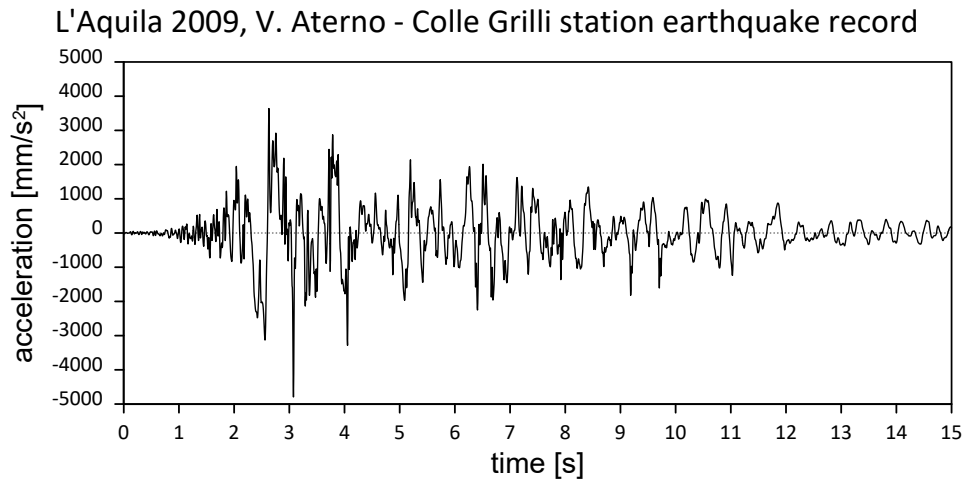


Figure 77: Earthquake record of the L'Aquila earthquake at the Aterno-Colle Grilli station in 2009.

The *TRBDF2* (Trapezoidal Rule-Backward Differentiation Formula 2) method, an advancement over the Newmark method, was employed as the integrator to transition from one step to the next in the analysis. Initially, *TRBDF2* utilizes the trapezoidal rule to approximate the area under the curve of the function. Subsequently, it employs the backward differentiation formula to enhance solution accuracy by estimating derivatives at the current time step using information from previous time steps (77).

The damping was introduced using Rayleigh method. The damping estimation was given by considering a damping ratio of 0.03 and the range of frequencies between the first and fifth mode.

The analyses were conducted employing an adaptive time step considering 3000 steps on a total duration of 15 seconds, which ensured a step duration of 0.005 s (coinciding with the sampling rate of the signal). The analysis settings were retained consistent with those established for the nonlinear static analysis.

## 7.7 Mesh architecture

The model was constructed using a global mesh size of 350 mm, chosen to achieve a balance between result accuracy and computational resources. This coarse mesh was acceptable thanks to the use of *ASDConcrete3D*, which is insensitive to mesh size variations. For the mortar layers, which are very thin, a finer mesh of 15 mm was employed. The mesh was refined to 300 mm in the case of Semi-Connected models.

During the analysis, 8 processors were utilized for the Fully-Connected model, 14 for the Semi-Connected models and 3 for the Isolated Units models, each handling approximately 5000 partition elements (Figure 78, Figure 79 and Figure 80).

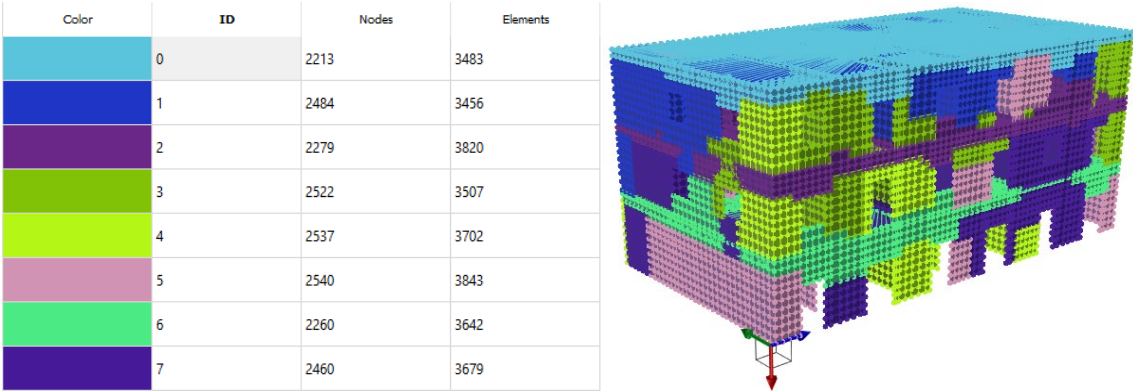


Figure 78: Fully-Connected Model Partitioning.

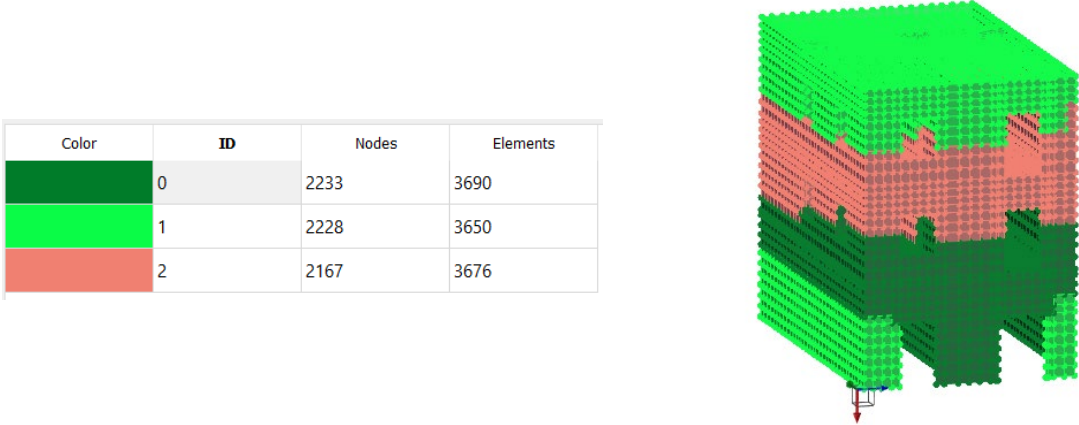
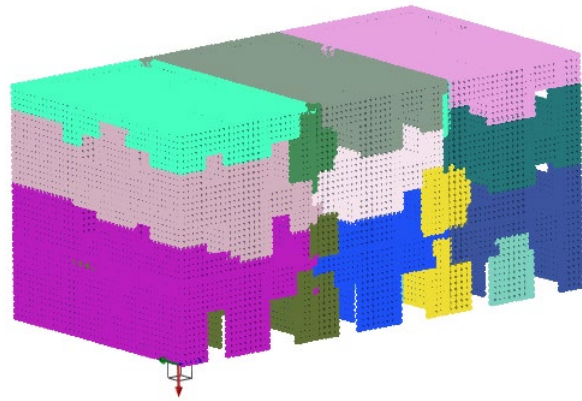


Figure 79: Isolated Model Partitioning.

Color	ID	Nodes	Elements
	0	2815	4924
	1	2967	4932
	2	3231	4960
	3	3007	4848
	4	3262	5054
	5	2778	4929
	6	3334	5111
	7	3296	5272
	8	3238	5209
	9	2740	4908
	10	3147	5216
	11	3273	5381
	12	3183	5104
	13	3062	5222



*Figure 80: Semi-Connected Model Partitioning.*

With a computer with average computational capabilities, it was possible to conduct most of the analysis simulations for each case in less than an hour and a half. For dynamic analysis, a high-performance workstation was utilized to reduce the computation time to under six hours.

## 8. Analysis and verification results

The units within the aggregate were analysed using modal, nonlinear static, and nonlinear dynamic analyses. Seismic vulnerability was evaluated with the N2 method. The analyses were carried out considering the units as isolated, rigidly connected, and with a mortar layer at the interface, employing mortars  $m_1$ ,  $m_3$ ,  $m_4$ , and  $m_6$ .

### 8.1 Eigenvalue analysis results

Modal analysis was conducted to study the models, extracting their dynamic properties including vibration modes, frequencies, and modal participation factors. Table 11 presents the period and modal participation ratios in the x and y directions for the first 5 vibration modes of the aggregate when modelled as Fully-Connected, as well as for each unit studied in isolation. Meanwhile, Table 12 displays the corresponding data for the Semi-Connected cases.

Table 11: Dynamic properties of the Fully-Connected aggregate and units modelled as isolated.

Fully Connected				Isolated units								
Mode				Unit 1			Unit 2			Unit 3		
	T	MX	MY	T	MX	MY	T	MX	MY	T	MX	MY
	[s]	[%]	[%]	[s]	[%]	[%]	[s]	[%]	[%]	[s]	[%]	[%]
1	0.164	66.34	0.53	0.196	70.69	0.002	0.199	71.27	0.00	0.195	70.77	0.03
2	0.152	0.64	72.24	0.141	0.00	70.76	0.138	0.01	72.57	0.142	0.14	70.01
3	0.119	9.33	0.05	0.109	1.31	0.20	0.109	1.16	0.06	0.109	1.31	1.03
4	0.075	0.001	0.06	0.073	13.76	0.24	0.074	15.54	0.07	0.074	4.37	1.61
5	0.074	0.003	0.006	0.072	0.04	0.003	0.068	0.01	0.01	0.074	0.53	0.00

Table 12: Dynamic properties of the Semi-Connected aggregate.

Mode	SC - $m_1$			SC - $m_3$			SC - $m_4$			SC - $m_6$		
	T	M <sub>X</sub>	M <sub>Y</sub>	T	M <sub>X</sub>	M <sub>Y</sub>	T	M <sub>X</sub>	M <sub>Y</sub>	T	M <sub>X</sub>	M <sub>Y</sub>
	[s]	[%]	[%]	[s]	[%]	[%]	[s]	[%]	[%]	[s]	[%]	[%]
1	0.176	67.22	1.68	0.172	69.27	0.12	0.172	69.27	0.12	0.169	69.18	0.06
2	0.140	2.93	67.96	0.139	0.24	71.00	0.139	0.24	71.00	0.139	0.15	71.10
3	0.121	5.82	1.53	0.121	6.57	0.18	0.121	6.57	0.18	0.120	6.75	0.16
4	0.0755	0.02	0.08	0.0755	0.001	0.032	0.0755	0.001	0.032	0.0755	0.001	0.030
5	0.0751	0.25	0.28	0.0751	0.008	0.007	0.0751	0.008	0.007	0.0751	0.007	0.006



In all instances, the fundamental mode predominantly manifests in the x-direction, the second mode in the y-direction, and the third mode around the z-axis. Table 13, Table 14 and 15 display the first three modal shapes of the models.

Table 13: First 3 modal shapes of the Fully-Connected aggregate.

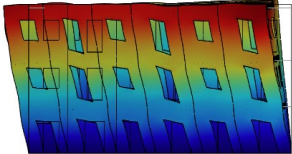
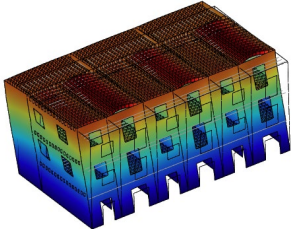
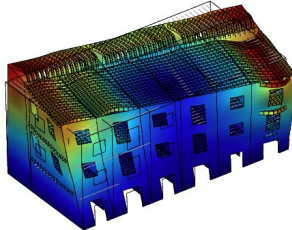
	1 <sup>ST</sup> mode	2 <sup>ND</sup> mode	3 <sup>RD</sup> mode
Fully Connected			

Table 14: First 3 modal shapes of the isolated units.

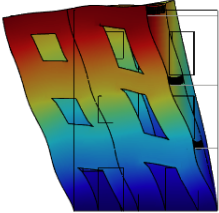
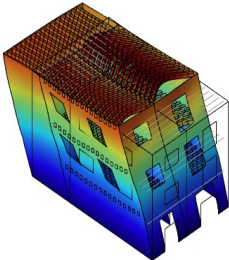
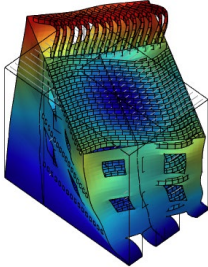
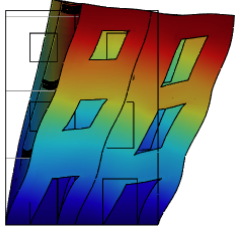
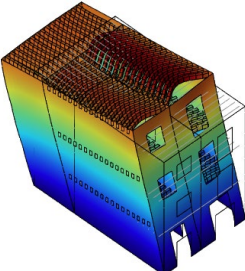
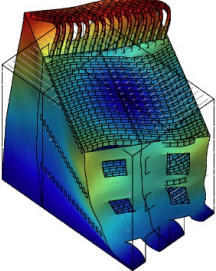
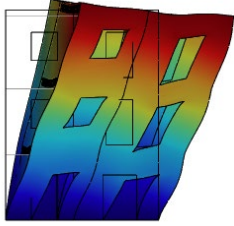
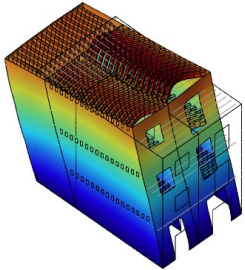
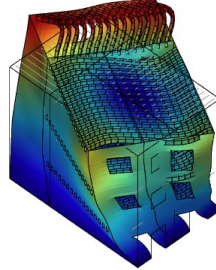
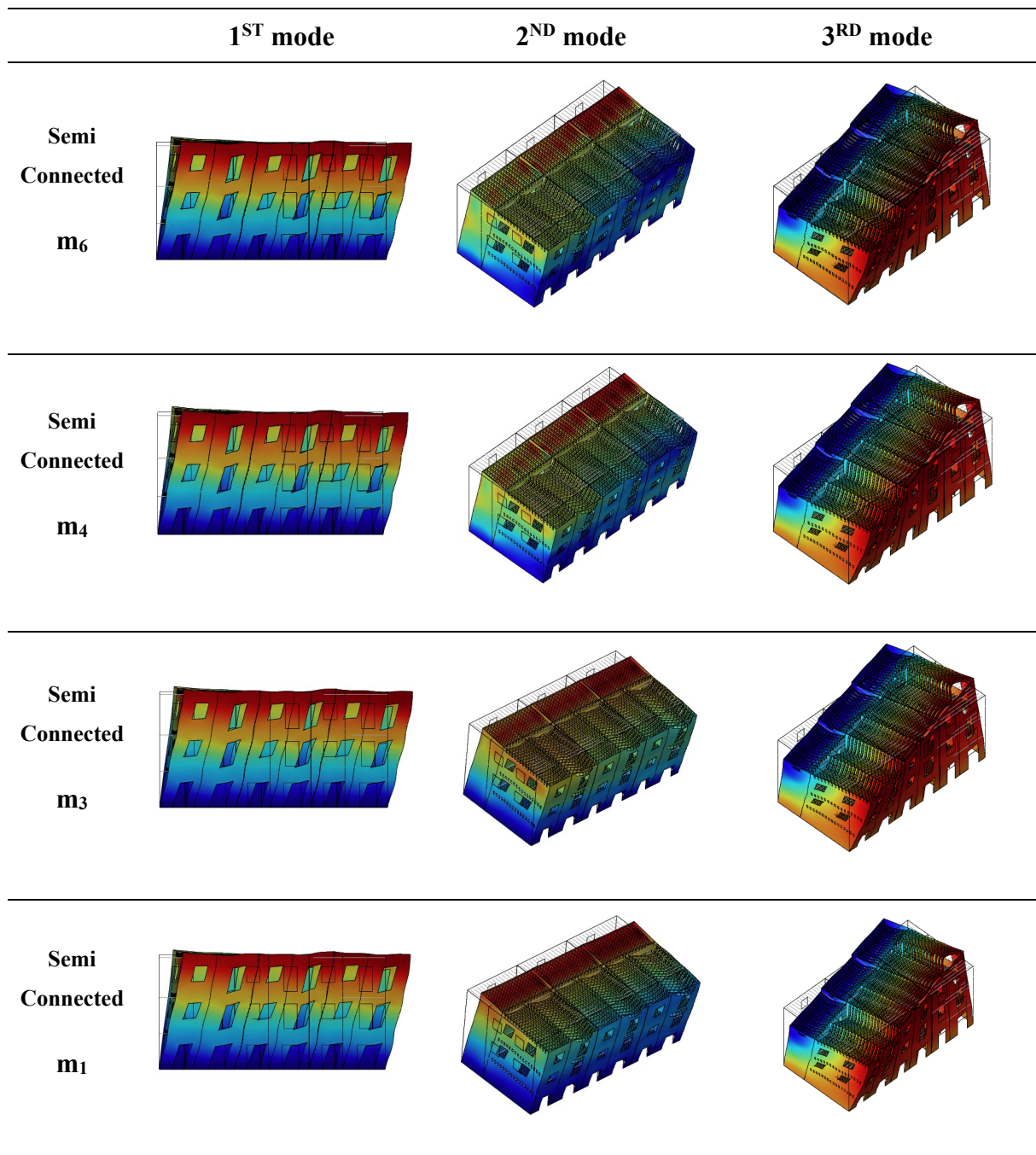
	1 <sup>ST</sup> mode	2 <sup>ND</sup> mode	3 <sup>RD</sup> mode
Isolated Unit 1			
Isolated Unit 2			
Isolated Unit 3			

Table 15: First 3 modal shapes of the Semi-Connected aggregate.



The first three modes of vibration clearly appear distinctly from each other, showing the aggregate's tendency to exhibit a box-like behavior, thanks to the presence of the rigid diaphragm at each floor. This characteristic persists even in the semi-connected case, where units are connected by mortar layers.

The displacements of the barycenter of the three floors were derived from the fundamental mode of vibration. Subsequently, these displacements were employed as the trend for the

horizontal loads applied in the pushover analyses in their respective cases. Each component of the fundamental eigen vector was multiplied by the mass of the corresponding floor, and the resultant force vector was normalized. This procedure is showed in Table 16, 17 and 18.

Table 16: Lateral force distribution in Fully-Connected aggregate.

	Floor	$\phi_i$	Norm. $\phi_i$	Mass [ton]	Force [kN]	Norm. Force
<b>FC</b>	3	3.557	1.000	348	347.67	0.996
	2	2.593	0.729	479	348.99	1.000
	1	1.304	0.367	728	266.83	0.765

Table 17: Lateral force distribution in Isolated units.

	Floor	$\phi_i$	Norm. $\phi_i$	Mass [ton]	Force [kN]	Norm. Force
<b>Unit 1</b>	3	6.428	1.000	128	127.74	1.000
	2	4.404	0.685	184	126.00	0.986
	1	2.094	0.326	277	90.39	0.708
<b>Unit 2</b>	3	6.376	1.000	128	128.45	0.986
	2	4.392	0.689	189	130.30	1.000
	1	2.100	0.329	279	91.93	0.706
<b>Unit 3</b>	3	6.392	1.000	128	128.26	0.997
	2	4.389	0.687	187	128.69	1.000
	1	2.083	0.326	276	89.88	0.698

Table 18: Lateral force distribution in Semi-Connected aggregate.

	Floor	$\phi_i$	Norm. $\phi_i$	Mass [ton]	Force [kN]	Norm. Force
<b>SC-m<sub>6</sub></b>	3	3.392	1.000	384	384.14	0.940
	2	2.500	0.737	555	408.72	1.000
	1	1.264	0.372	824	306.87	0.751
<b>SC-m<sub>4</sub></b>	3	3.397	1.000	384	384.14	0.940
	2	2.502	0.737	555	408.57	1.000
	1	1.264	0.372	824	306.68	0.751
<b>SC-m<sub>3</sub></b>	3	3.383	1.000	384	384.14	0.944
	2	2.483	0.734	555	407.11	1.000
	1	1.252	0.370	824	304.91	0.749
<b>SC-m<sub>1</sub></b>	3	3.370	1.000	384	384.14	0.948
	2	2.463	0.731	555	405.39	1.000
	1	1.239	0.368	824	302.94	0.747

The force trends were used in the pushover analysis for both positive and negative directions.

## **8.2 Non-linear static analysis results**

### **8.2.1 Pushovers in positive direction**

The pushover analyses were conducted using a displacement control, applying the modal distribution of force determined in the previous paragraph 8.1. The results of the nonlinear static analyses in the positive direction for the Fully-Connected, Semi-Connected, and isolated units are presented in Figure 81. In all cases, the base reactions of the walls in the longitudinal direction of each unit and of the entire aggregate were evaluated.

In the Fully Connected case, the control node was assumed to be the barycentre of the third floor, and only one analysis was conducted in the positive direction, evaluating each unit's reaction. Similarly, for isolated units, the control node was placed on the barycentre of the third floor and the aggregate reaction was considered as the summation of the reactions of the individual units. No issues were showed in achieving the target displacement of 35 mm for the fully connected and isolated cases due to the absence of boundary conditions.

In the scenario involving Semi-Connected units, pushover loads were applied to all units, with each floor bearing one-third of the load distributed to the barycentre of the entire aggregate. In this case, it was not possible to detect the reaction of all the units considering a unique position of the control node due to the issues explained in section 7.6 Analysis settings. The unit with the control node applied on the third-floor experienced different displacement compared to the other two units. Three analyses were performed for the positive direction, with each case involving the control node specifically applied to the unit which the base reaction is evaluated. The aggregate reaction was evaluated relative to the case where the control node was applied to the third floor of the central unit.

For some curves, achieving the target displacement of 35 mm for the control node was not possible. Convergency problems were absent in the case of fully connected or isolated units or when studying the reaction of Unit 3 for the Semi-Connected condition, where there were no boundary conditions. However, in the Semi-Connected case, units 1 and 2 exhibited instability because their displacement is strongly influenced by the presence of adjacent units on the right side. The unit pushed by the one with the control node undergoes notable deformation and may potentially fail. Once the failure of the pushed unit is achieved, to increase the displacement of the unit with the control node, the pushed unit must deform significantly, potentially causing convergence problems. Therefore, the curves related to the reaction of units 2 and 1 couldn't

achieve the target displacement of 35 mm. The analyses were advanced to achieve at least a real or conventional failure of the unit.

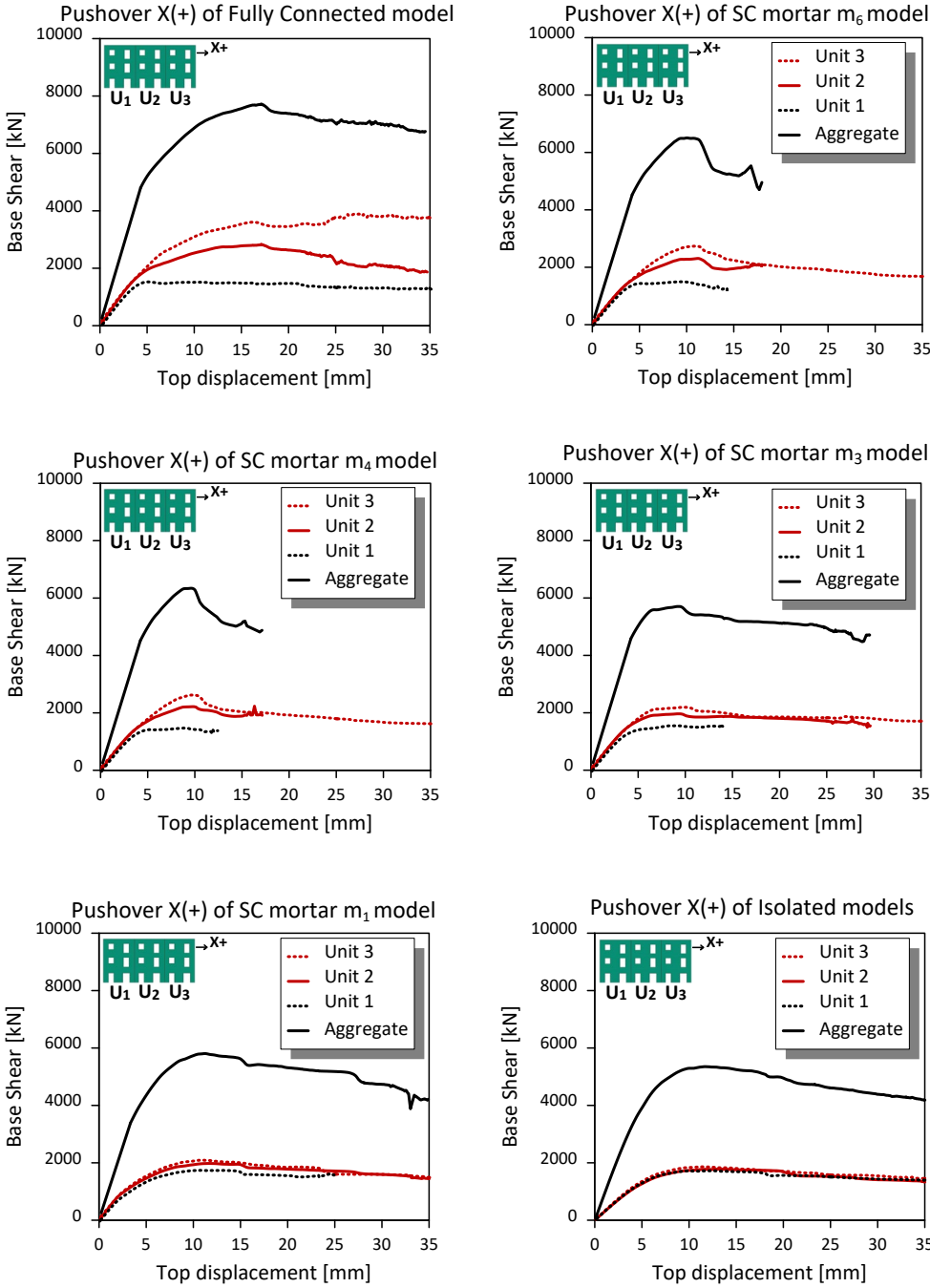


Figure 81: Pushover curves in positive direction.

From the curves evaluated for the positive direction push, it is evident that the higher the degree of connection between units is, the greater the difference in reaction taken by each unit. In the case of isolated units, each unit shows to have almost equivalent reactions, as evidenced by the overlapping curves in Figure 81. For Fully Connected units, Unit 3 exhibits higher resistance, bearing a greater load compared to Unit 1.

The base reaction distribution between the two external units in the case of Semi-Connected units is intermediate between the two aforementioned cases. Considering the weakest mortar ( $m_1$ ), the difference in reaction between units tends to vary slightly. However, when a stronger mortar is assumed at the interface, such as the  $m_6$  case, the asymmetry of the load distribution between the two external units becomes more significant.

It can be concluded that the degree of connection between units plays a crucial role in determining the distribution of stress between the units. When the vertical connection between units exists, in the case of positive push, Unit 3 is subjected to compression, while Unit 1 experiences decompression, reducing its reaction. A simplified static scheme of the problem (Figure 82) illustrates the moment imposed at the base of the building. This results in various vertical compensatory reactions at the base ( $R_{1M}$  and  $R_{3M}$ ), which further compress or decompress each unit based on its position relative to the aggregate and the direction of the horizontal force.

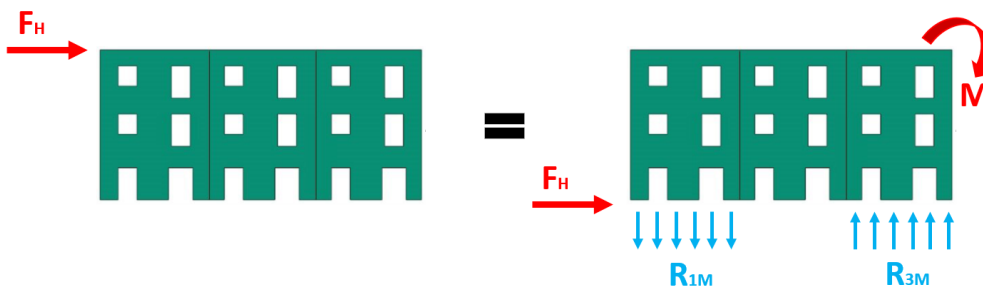


Figure 82: Repartition of loads related to the aggregate-effect.

The Semi-Connected curves of units 2 and 3 illustrate that increasing the resistance of the mortar interface leads to a higher resistance. However, their trends show brittleness, with resistance softening after reaching its peak. Notably, a higher resistance of the mortar corresponds to a more evident softening branch.

Figure 83 illustrates the distribution of base reactions among longitudinal walls for each unit during pushover analysis in the positive direction. The presence of rigid diaphragms facilitates an effective distribution of reactions between these walls. As expected, forces are distributed according to each wall stiffness, causing the Front Wall (most flexible due to the presence of openings) to bear less loads compared to the other two walls. Conversely, the back wall being stiffer supports a greater load. In Semi-Connected cases, the back wall is particularly affected by the aggregate effect, leading to a significant reduction in its load-bearing capacity when the mortar interface fails.

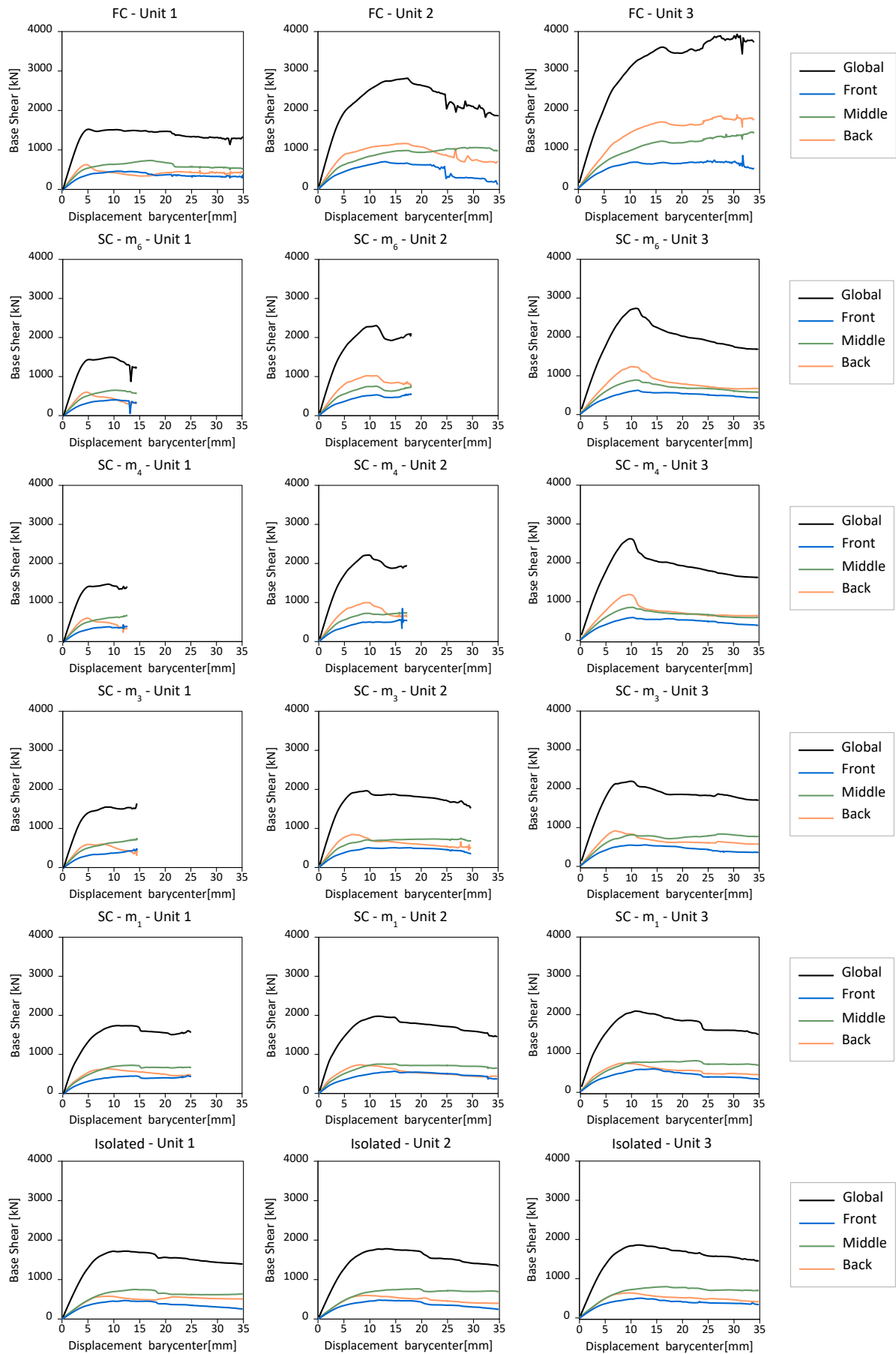


Figure 83: Reaction forces measured in longitudinal walls in the X(+) direction with respect to the displacement of the barycenter of the unit.

These results exhibit the role of the rigid diaphragm in transversally connecting the longitudinal walls and securing load transference, while the mortar plays a crucial role in transferring loads longitudinally between units and, therefore, the development of the aggregate effect.

### **8.2.2 Pushovers in negative direction**

Similarly to the positive directions, the nonlinear static analysis was also repeated for the negative direction. The same considerations made for the placement of the control node for the positive push can be applied here. The Fully Connected and isolated units case were analysed considering as control node the barycentre of the third floor. While for Semi-Connected models, the control node was placed on the barycentre of the third floor of the unit of interest.

For the Fully Connected case, isolated units, and Unit 1 in the Semi-Connected model, the analyses achieved the target displacement of 35 mm. In the Semi-Connected case, units 2 and 3 exhibited instability due to the presence of an adjacent unit acting as a boundary condition on the left side. For instance, when the control node is on Unit 2, it pushes Unit 1, subjecting it to high deformation and potential failure. Further displacements of the control node on Unit 2 are only possible if Unit 1 undergoes significant deformation, causing convergence problems. Attempts were made to achieve conventional or real failure for all the curves. In some cases, it was necessary to increase the number of iterations in each step of analysis.

Figure 84 presents the capacity curves for each case, comparing the reaction of the entire aggregate with that of the individual units in each graph. The pushover in the negative direction generates compression in Unit 1 and decompression in Unit 3 when the connection between units is present. In the case of a fully connected aggregate, Unit 1 shows higher resistance compared to the other two units, thanks to the confinement provided by the aggregate effect. The difference in reactions between units decreases when considering a weaker degree of connection between them. In the case of isolated units, all three units show similar resistance.

The Semi-connected cases demonstrate higher resistance when a stronger mortar is used, and the post-peak behaviour exhibits softening, except for Unit 3, which experiences decompression. By increasing the connection between units, the curves become more brittle and show a more evident softening branch.



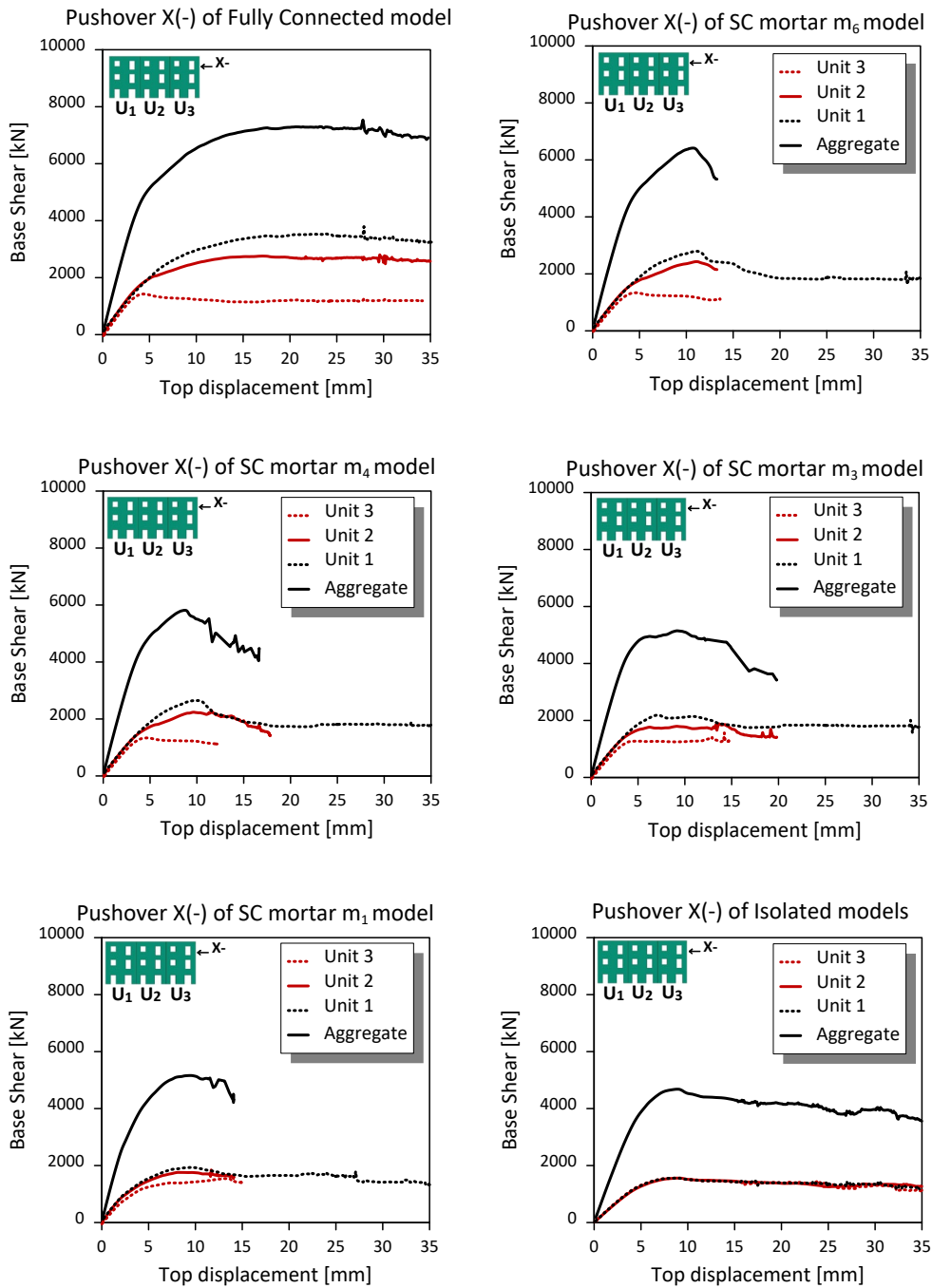


Figure 84: Pushover curves in the negative direction.

Figure 85 illustrates the distribution of base reactions along longitudinal walls during pushover analysis in the negative direction. Similar to the positive direction, the back wall exhibits larger reactions and experiences greater increments due to the aggregate effect compared to the other two walls. Conversely, the front wall demonstrates the lowest resistance, while the middle wall exhibits an intermediate reaction level between the two. The presence of rigid diaphragms facilitates an effective distribution of reactions between these walls.

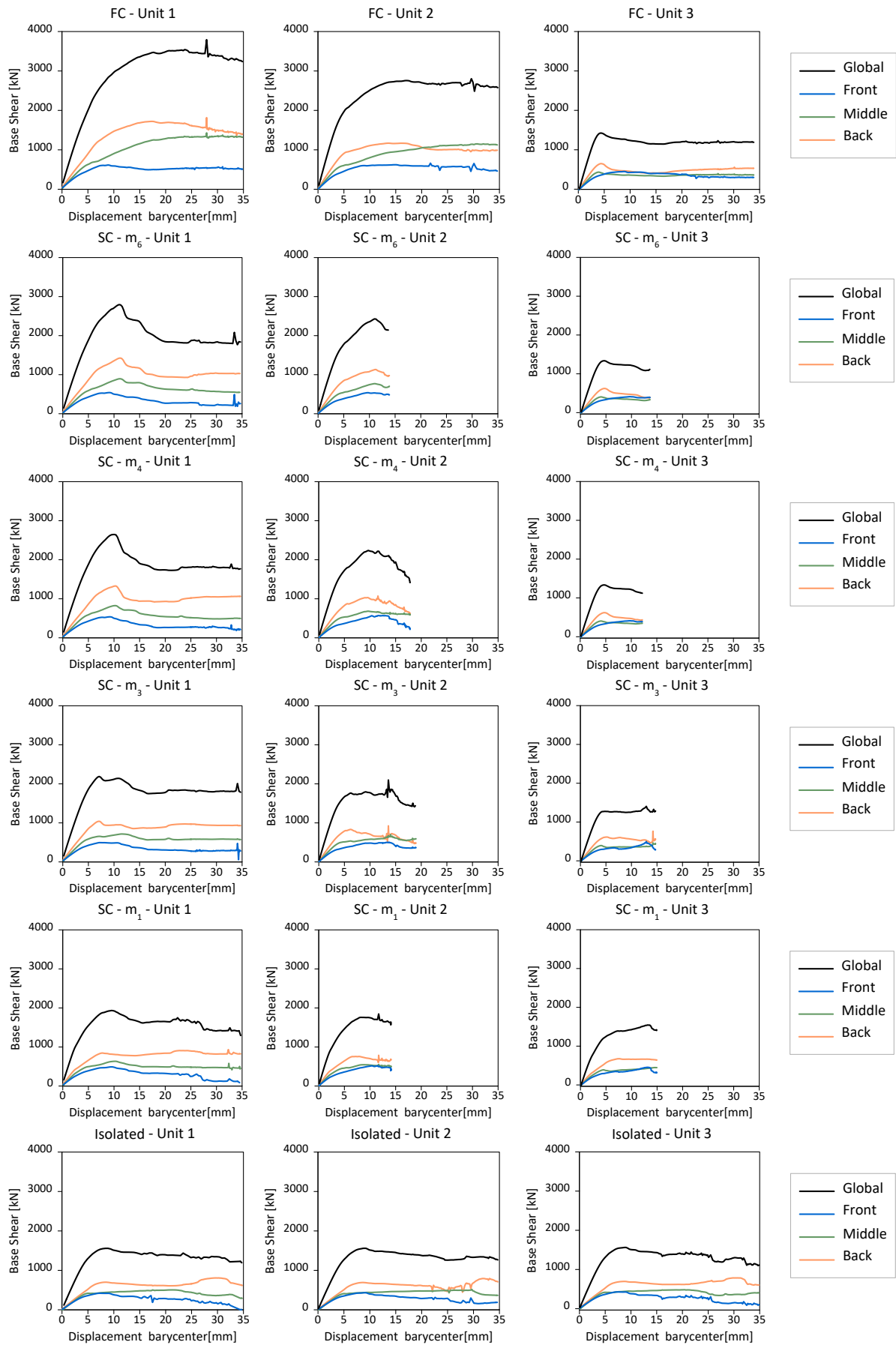


Figure 85: Reaction forces measured in longitudinal walls in the X(-) direction with respect to the displacement of the barycenter of the unit.

### 8.2.3 Damage Analysis

A comprehensive analysis of the damage incurred by each unit is presented in Figure 86, 87, 88 and 89. In the case of the Fully Connected model, the damage assessment is related to the analysis step at which the first unit experiences failure. For all other models, the crack patterns correspond to either conventional or real failure conditions. Conventional failure refers to when the pushover curve exhibits a 15% reduction in maximum resistance, while real failure is characterized by specific mechanisms that prevent the structure from withstanding further loads. The crack patterns depicted are directly associated with principal section deformations, showing only the cracks caused by tensile fractures.

The presence of rigid diaphragms facilitates crack distribution throughout the longitudinal walls. The front wall, exhibiting the highest number of openings, is typically the first to suffer damage among the longitudinal walls. When damage occurs to this front wall, its stiffness decreases, and the presence of rigid diaphragms at every floor helps redistribute the forces to the longitudinal walls, showcasing a larger spread of the damage in all walls.

In all crack patterns, the detachment of the back wall from the base is evident. This phenomenon is the primary cause of the resistance reduction observed in the back wall, as depicted in Figure 83 and Figure 85.

In the Fully Connected model, the perfectly rigid connections between units facilitate their collaboration, allowing cracks to propagate across adjacent units. Positive direction pushovers commonly lead to failure due to the activation of a second-floor mechanism. However, this mechanism does not extend to the base, resulting in a not evident reduction in pushover curves. While, in negative direction pushovers, damage predominantly concentrates on the first floor, leading to the collapse of base columns.

The distinct collapse mechanisms observed in positive and negative-direction pushovers can be attributed to the asymmetry of openings, which leads to different structural responses depending on the direction of the applied horizontal force.

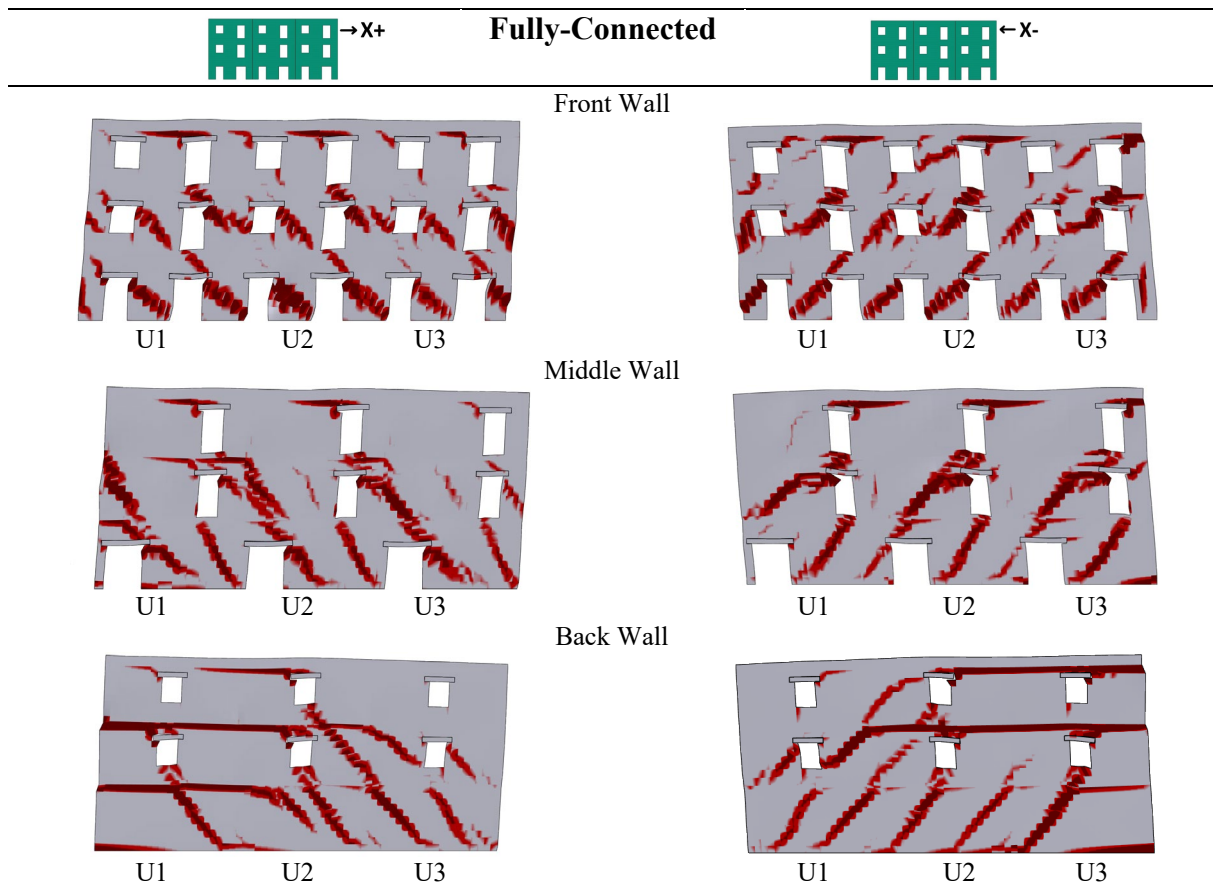


*Figure 86: Crack patterns related to the failure of the Fully Connected model in pushovers.*

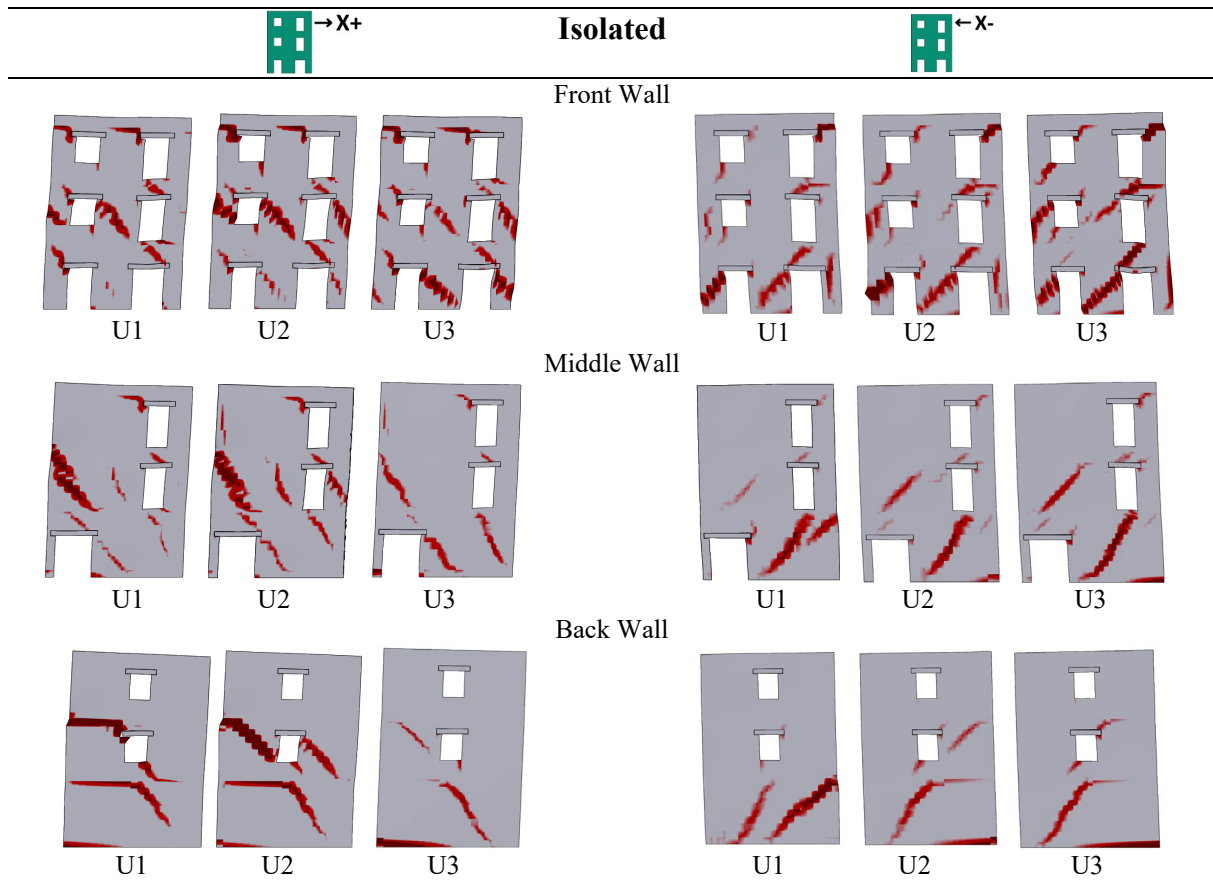


*Figure 87: Crack patterns related to the failure of the Isolated model in pushovers.*

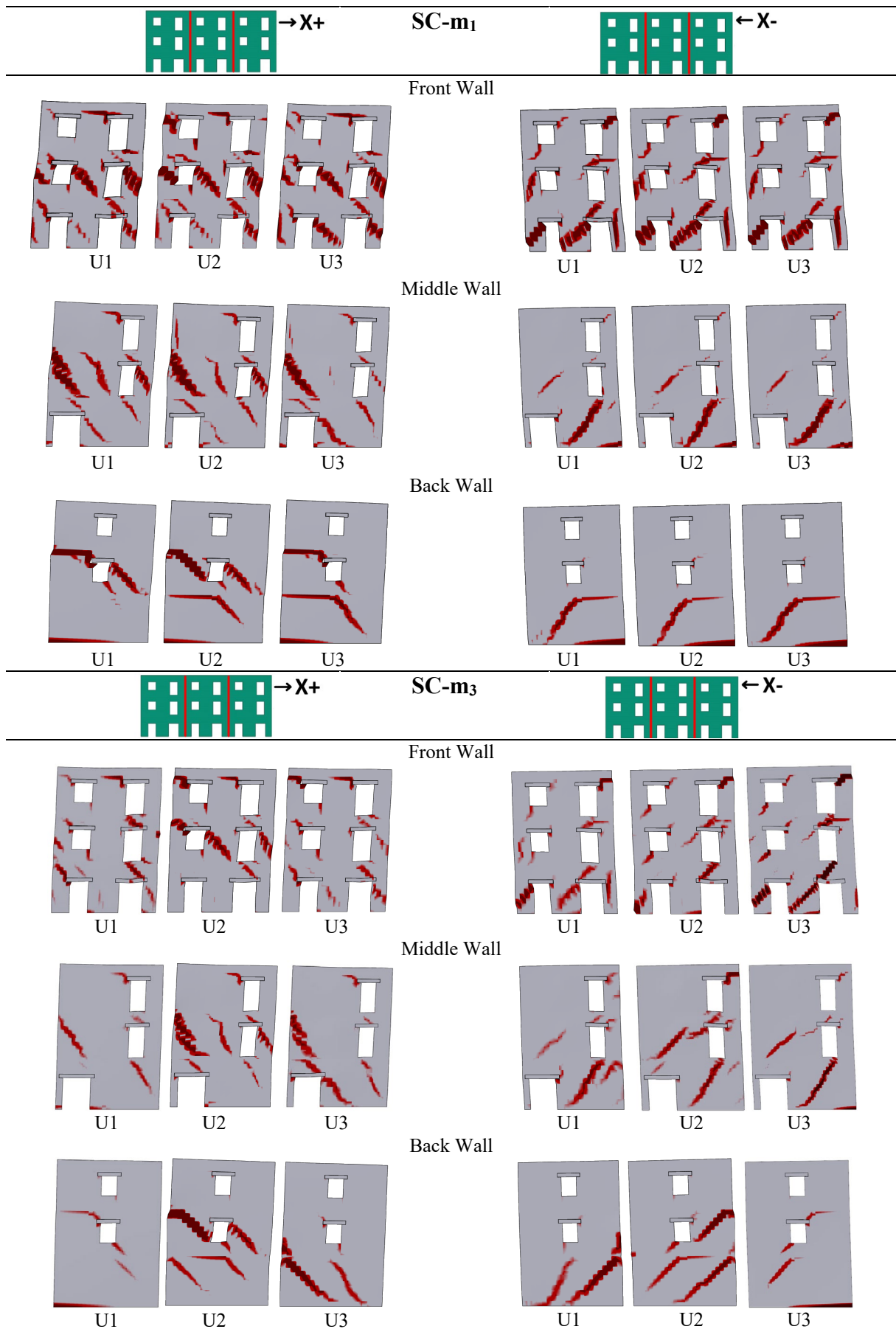


Figure 88: Crack patterns related to the failure of the Semi-Connected  $m_1$  and  $m_3$  models in pushovers.

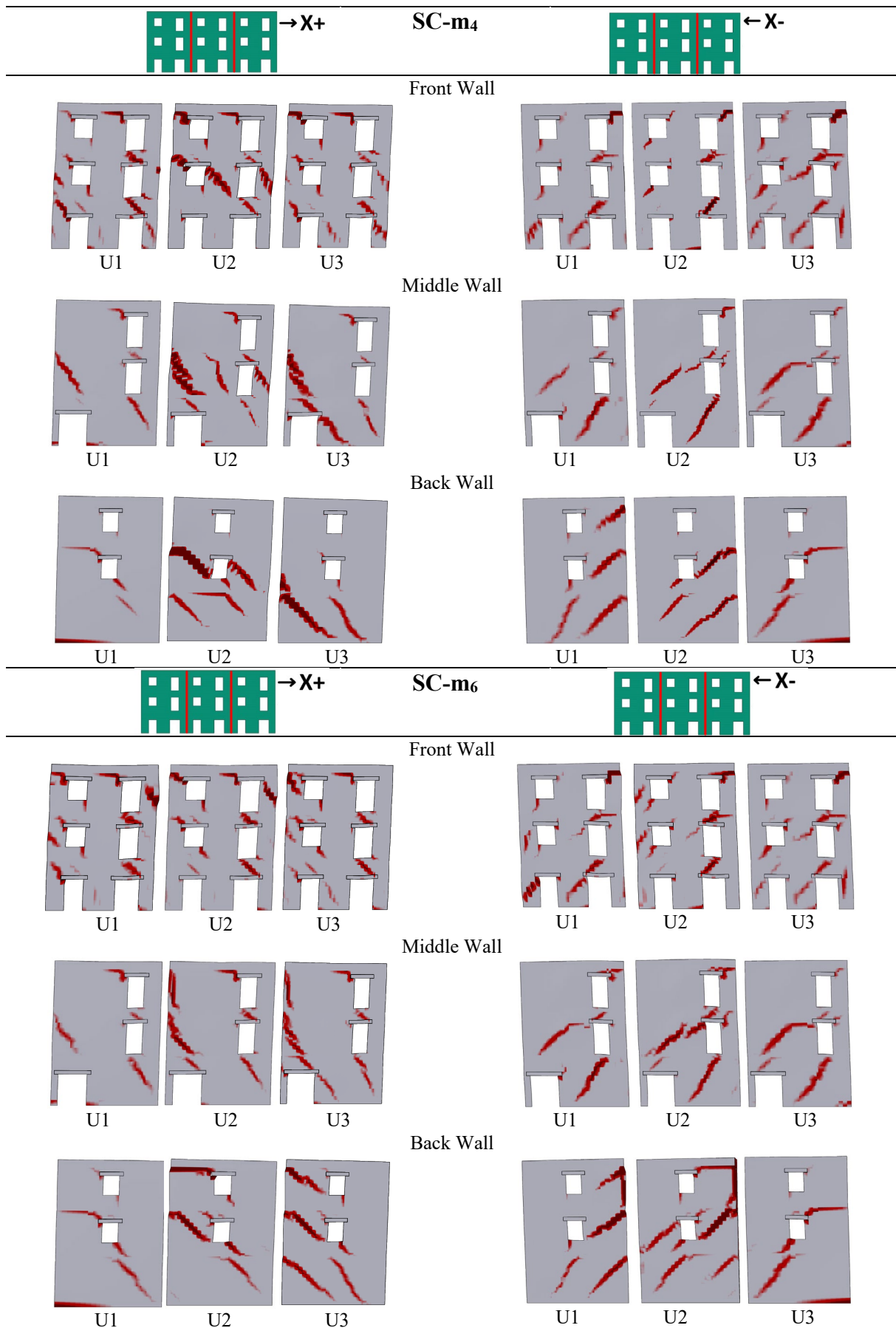


Figure 89: Crack patterns related to the failure of the Semi-Connected  $m_4$  and  $m_6$  models in pushovers.

The crack patterns observed in the Semi-Connected models exhibit varying degrees of damage. When employing weaker mortars such as  $m_1$  and  $m_2$  (Figure 88), a greater number and larger sizes of cracks are evident. Conversely, with stronger mortar types like  $m_4$  and  $m_6$  (Figure 89), the patterns show fewer significant cracks that cannot be directly associated with unit failure.

The cracks related to the conventional failure achievement of Semi-Connected models cannot solely explain the brittle behaviour exhibited by the pushover curves of these models, especially in the case of stronger mortar interface connection. For example, in the positive pushover of Unit 3 in the Semi-Connected aggregate with an  $m_6$  mortar interface, the curve displays pronounced resistance decay after the peak. In Figure 90a, the crack pattern reached at a displacement of the control node of  $d_x=13.9$  mm is shown, corresponding to the conventional failure of the highlighted case.

Even though conventionally and according to the NTC, this step of the pushover should be associated with the failure of the structure, there isn't any specific failure mechanism that could justify it. However, a failure mechanism becomes evident at the second floor of the Front Wall and at the base of the Middle and Back walls when the control node reaches a displacement of  $d_x=25.1$  mm, as shown in Figure 90b.

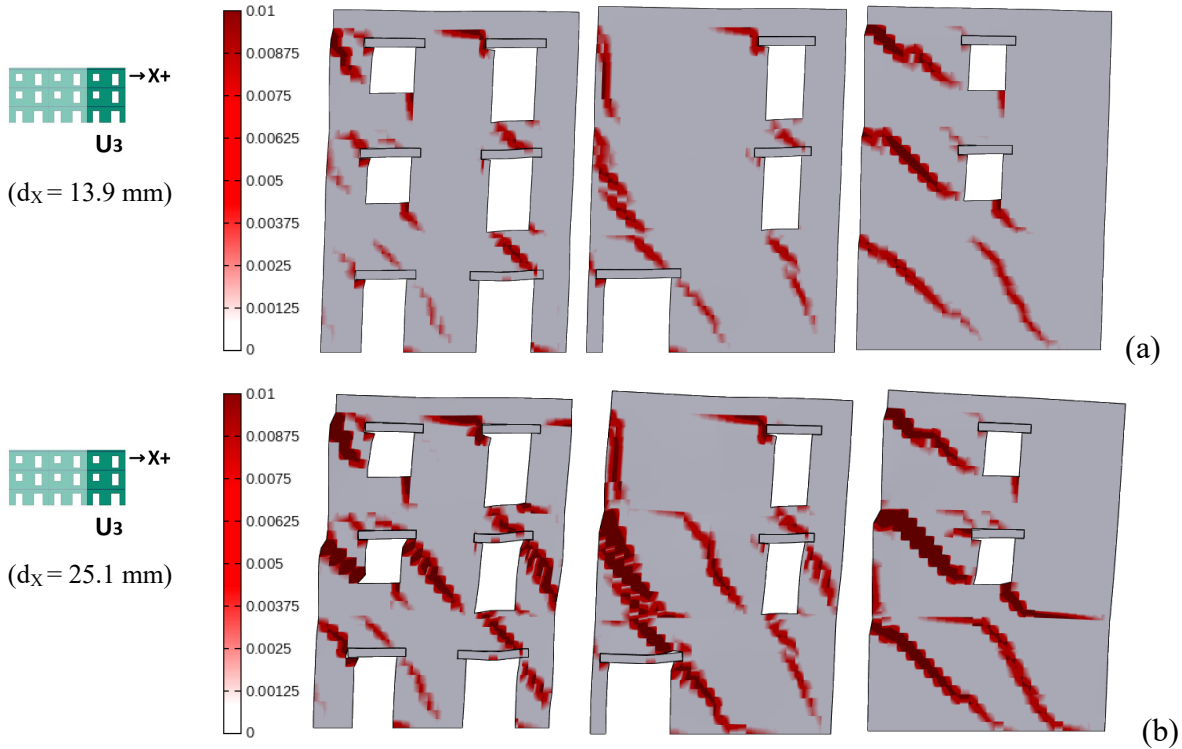


Figure 90: Conventional (a) and real (b) failure of Unit 3 in Semi-Connected  $m_6$ .

Additionally, it was observed that the beginning of the drop in resistance coincided with the failure of the mortar. This disconnection is evident in Figure 91 which displays the crack pattern at peak resistance, reached at a displacement of 10.9 mm of the control node. The failure of the mortar can potentially be attributed to shear stress resulting from the compression and decompression of the external units, which is caused by the redistribution of stresses associated with the aggregate effect.

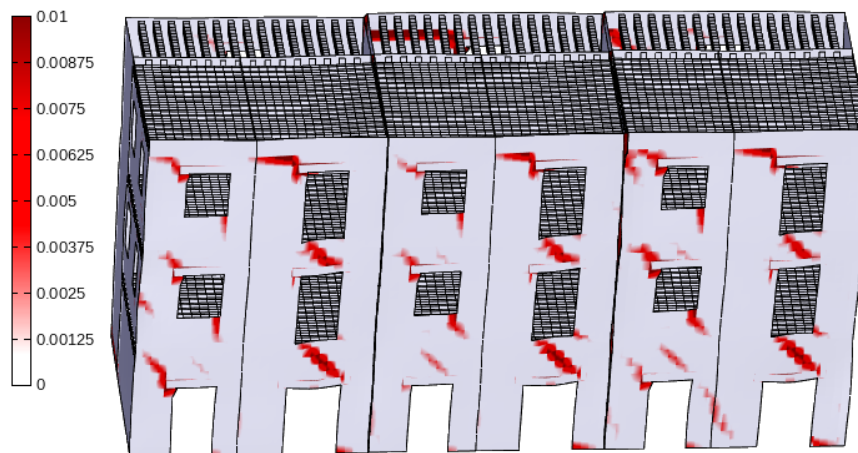


Figure 91: Disconnection between Unit 2 and 3 in the Semi-Connected  $m_6$  Crack pattern.

Given these observations, it is suggested that the decay observed in the pushovers is not caused by structural failure but rather associated with the disconnection of units caused by the rupture of the interface. The behaviour described for Unit 3 of the Semi-Connected  $m_6$  model can also be observed in the other units of the different Semi-Connected cases to a different extent. In the case of a less resistant interface mortar, the decrease in resistance is less pronounced due to the lesser impact of the aggregate effect.

In positive direction pushovers, the stronger the interface mortar, the greater the compression in Unit 3 and the decompression in Unit 1 become, leading to higher tangential stress at the interfaces. Once the interconnecting mortar between the units fails, the horizontal redistribution of forces is no longer feasible, and the units tend to exhibit resistance similar to that in the isolated case.

Another example is evident in the case of negative pushover of Unit 1 in the Semi-Connected configuration with mortar  $m_4$  at the unit interface. In this scenario, the pushover curves show that a 15% reduction in strength is obtained when the control node reaches a displacement of  $d_x=13.9$  mm, and the corresponding crack pattern is shown in Figure 92a. However, the failure of the structure cannot be associated with this crack pattern. The real failure of the unit occurs



when the first-floor pillars of the front wall reach their limits, at a displacement of 19.1 mm for the control node (Figure 92b). Even in this example, the drop in the pushover curve must be attributed to the disconnection of units caused by the failure of mortar at the interfaces.

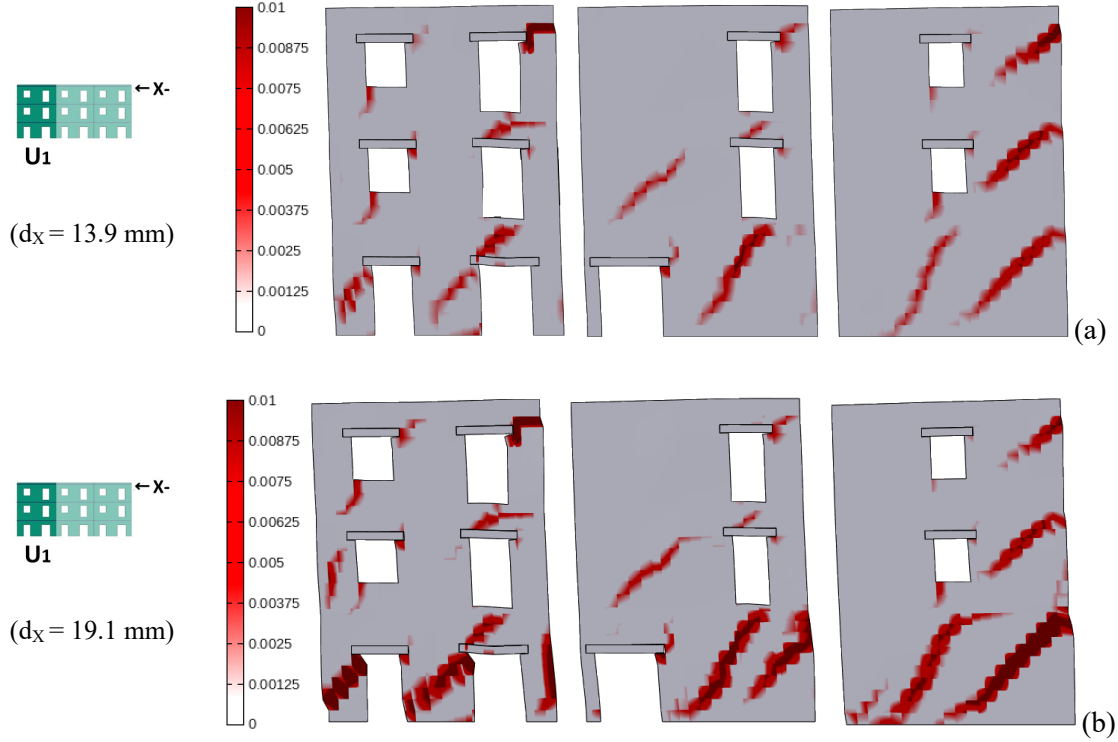


Figure 92: Conventional (a) and real (b) failure of Unit 1 in Semi-Connected  $m_4$ .

For both the positive and negative pushovers, it can be concluded that Semi-Connected cases tend to exhibit behavior similar to the isolated case once the mortar is damaged. The reduction in resistance is caused by the loss of the aggregate effect due to the failure of the mortar and not by the failure of the structure itself. This phenomenon is observed in cases where the mortar is most resistant, as it initially provides a higher increment in structural resistance.

### 8.3 Quantitative verification using the N2 method.

The curves derived from the pushover analyses were assessed using the N2 method (57) to evaluate the seismic vulnerability of the units under investigation, taking into account varying degrees of interconnection between units within the aggregate.

Each pushover curve, resulting for the multi-degree of freedom system, was transformed into its equivalent Single-Degree-of-Freedom (SDOF) capacity curve. This transformation involved scaling the base reaction by the first modal participation factor of the structure. The first modal participation factor was determined individually for each unit, taking into account its mass and the fundamental eigenmode obtained from modal analysis.

Table 19 displays the fundamental modal participation factor along with the properties characterizing the equivalent SDOF system, including its period  $T^*$  and mass  $m^*$ .

*Table 19: Parameters evaluated for the N2 method from pushovers conducted in the positive direction.*

		$\Gamma_1$	$m^*$ [ton]	$T^*$ [s]	$q^*$	$\mu_c$	$\zeta_e$
<b>Isolated</b>	Unit 1	1.413	344.1	0.221	2.41	4.30	1.00
	Unit 2	1.411	350.7	0.226	2.38	4.08	0.99
	Unit 3	1.410	346.9	0.218	2.25	3.88	0.98
<b>SC - <math>m_1</math></b>	Unit 1	1.382	364.2	0.219	2.47	3.67	0.86
	Unit 2	1.382	369.4	0.208	2.22	3.85	0.97
	Unit 3	1.380	366.6	0.203	2.07	3.33	0.93
<b>SC - <math>m_3</math></b>	Unit 1	1.380	365.4	0.201	2.71	3.49	0.73
	Unit 2	1.380	370.6	0.188	2.21	4.27	0.99
	Unit 3	1.378	367.9	0.191	1.98	3.24	0.92
<b>SC - <math>m_4</math></b>	Unit 1	1.378	366.5	0.200	2.91	3.21	0.64
	Unit 2	1.378	371.7	0.192	2.03	2.70	0.80
	Unit 3	1.376	369.0	0.198	1.66	1.82	0.79
<b>SC - <math>m_6</math></b>	Unit 1	1.378	366.6	0.198	2.86	3.32	0.66
	Unit 2	1.378	371.8	0.193	2.00	2.52	0.79
	Unit 3	1.376	369.1	0.199	1.59	1.99	0.87
<b>Fully Connected</b>	Unit 1	1.377	321.2	0.181	2.43	6.4	1.19
	Unit 2	1.377	321.2	0.173	1.38	3.95	1.44
	Unit 3	1.377	321.2	0.177	1.04	2.84	1.56

In each scenario, the masses of the different units are similar, with the central unit being slightly heavier due to the absence of lateral openings. The period associated with the equivalent Single-Degree-of-Freedom (SDOF) decreases when considering a more rigid connection between units. In the isolated configuration, the period tends to be higher for each unit, reaching its minimum in the Fully Connected configuration.

Subsequently, the curves were bilinearized, featuring two distinct parts: an initial elastic branch followed by a perfectly plastic behaviour. Figure 93 illustrates the bilinearization of the pushovers conducted in the positive direction for both the Fully Connected and isolated cases. The pushover curves were truncated upon reaching failure, whether real or conventional.

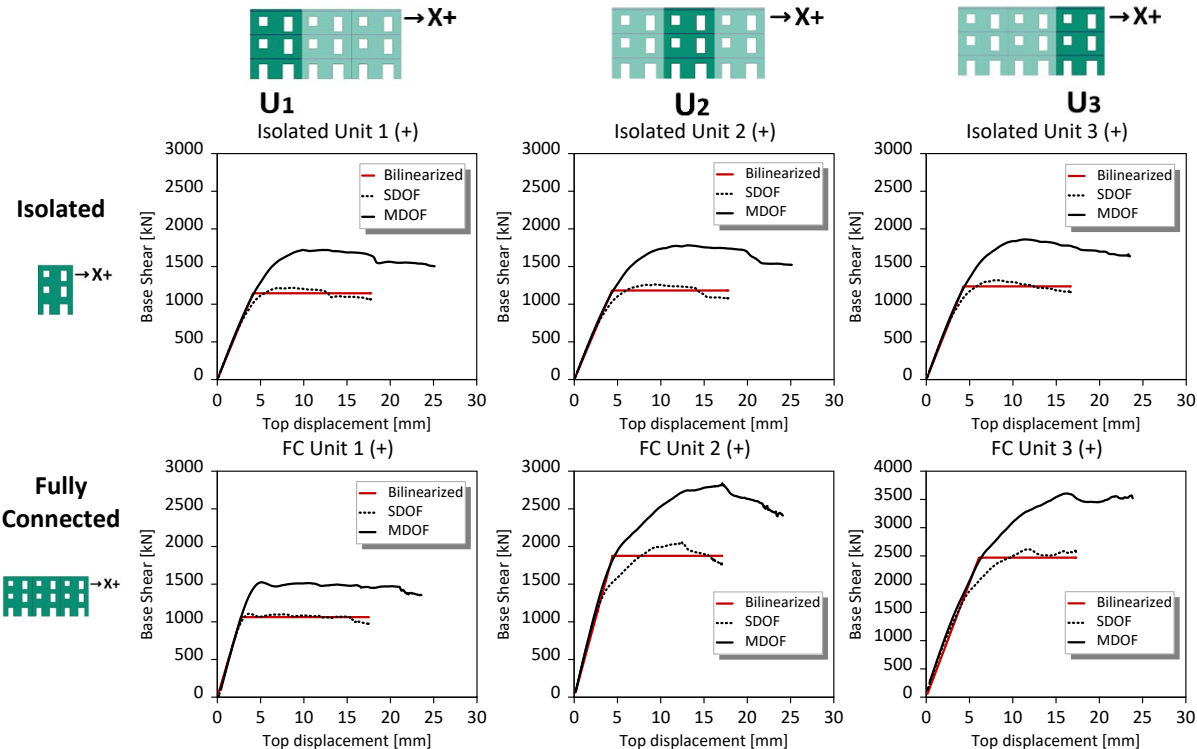


Figure 93: Equivalent SDOF and Bilinearized curves for Fully Connected and Isolated cases derived from pushovers in the positive direction.

For the positive direction pushover, the units modelled as isolated exhibit a similar trend. However, in the fully connected condition, the units demonstrate significantly different behaviours: Unit 3 shows higher resistance compared to Unit 1, yet its corresponding plastic branch is less extensive, indicating a less ductile behaviour. Unit 2 displays an intermediate behaviour between the two external units.

Figure 94 depicts the bilinearization for the Semi-Connected cases. Upon examining the trend of curves associated with these cases, it becomes evident that with the implementation of a stronger mortar at the interface, the curves tend to exhibit increased brittleness, resulting in

smaller plastic branches. The more rigid connection causes an increase in resistance for the compressed Unit 3 and the central unit, while Unit 1 experiences a reduction in resistance.

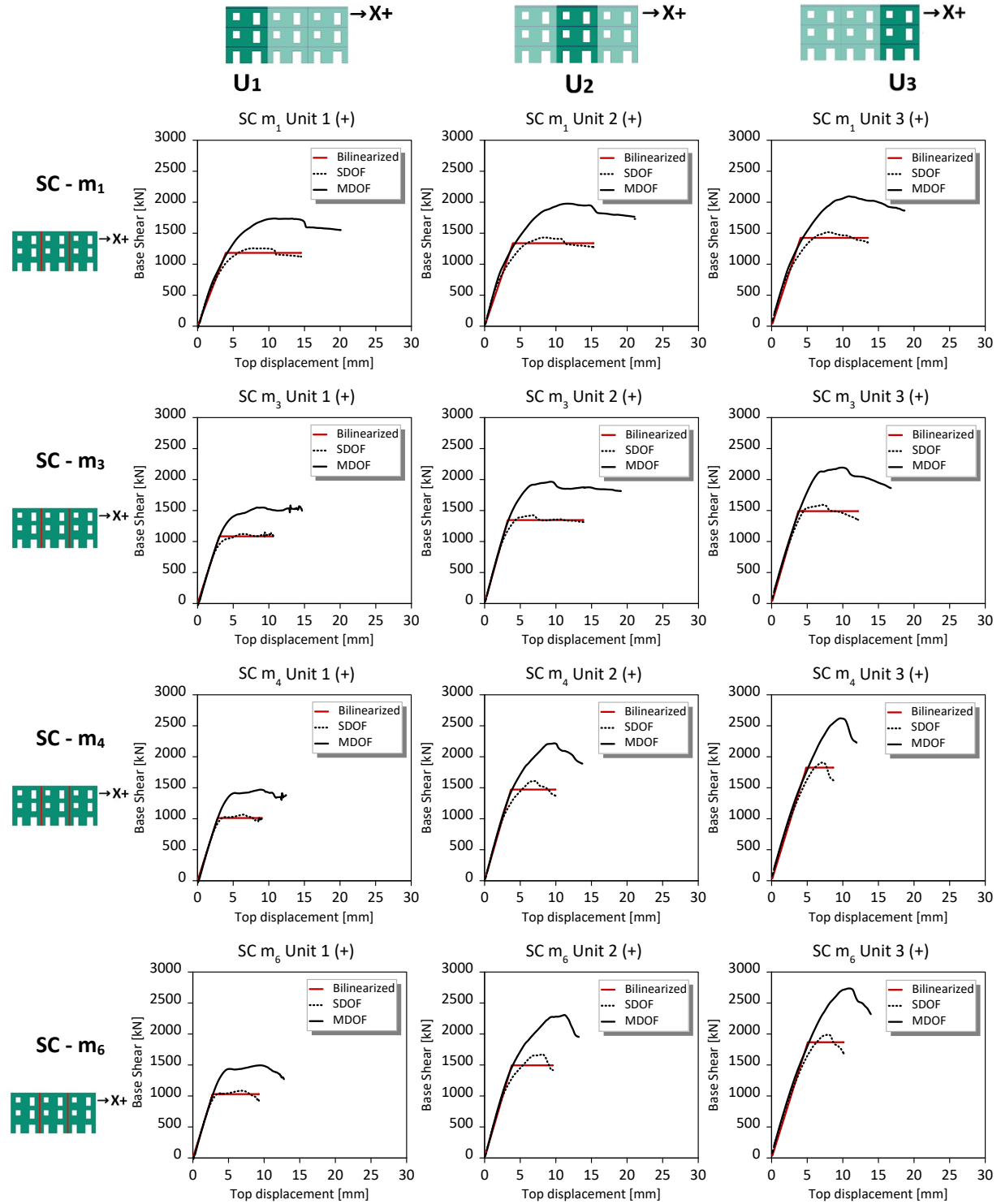


Figure 94: Equivalent SDOF and Bilinearized curves for Semi-Connected cases derived from pushovers in the positive direction.

The seismic vulnerability was assessed by defining three parameters: the ductility capacity of the system  $\mu_c$ , the reduction factor of the system  $q^*$ , and the vulnerability index  $\xi_E$ . These parameters are presented in Table 19. The trends described above, considering the curves' behaviour, can be revisited through the values assumed by  $\mu_c$ , which accounts for ductility, and  $q^*$ , which represents strength. In the case of isolated units, the three units exhibit similar  $q^*$  and  $\mu_c$  parameters. However, in the fully connected configuration, lower  $q^*$  values are observed compared to the isolated case, while ductility remains high. Additionally, the units tend to have different values from each other. Considering the Semi-Connected cases, when a weaker mortar is assumed at the interface layer, the values of  $q^*$  e di  $\mu_c$  tend to approach those of the isolated case, and the difference in parameters between the units is less pronounced. However, when increasing the connection stiffness,  $q$  decreases towards the fully connected case, while  $\mu_c$  decreases significantly, unlike in the fully connected scenario.

The comments expressed can be summarized in the evaluation of the vulnerability index values represented graphically in Figure 95.

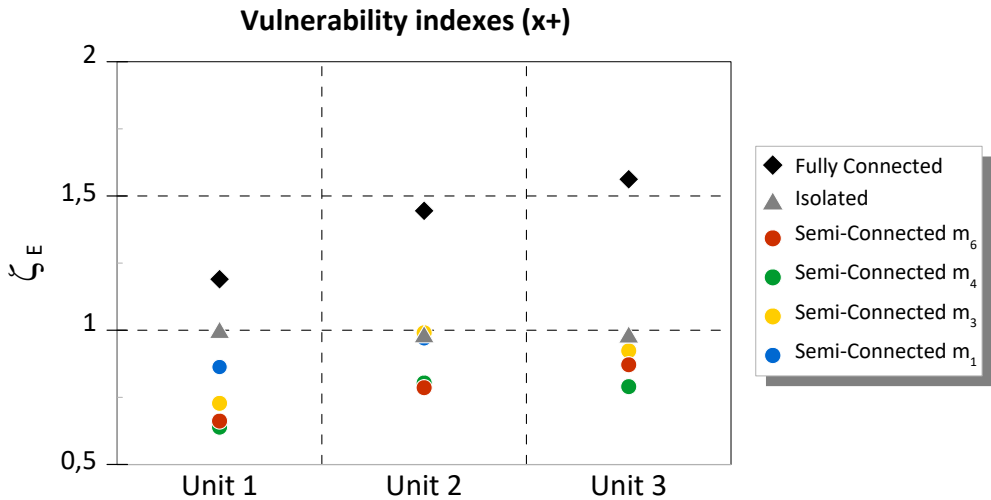


Figure 95: Vulnerability indexes comparison for pushovers in positive direction.

The vulnerability indexes associated with the Fully-Connected condition are higher for all units compared to the isolated condition. The isolated units exhibit nearly equivalent vulnerability index values due to their similar geometric characteristics. Unit 1 demonstrates closer vulnerability index values between the fully connected and isolated conditions, mainly because of the decompression resulting from the aggregate effect when subjected to positive-directional push.

The vulnerability indexes of Semi-Connected units are indeed lower than both fully connected and isolated units, resulting in a majority of cases where the verification is not satisfied. Additionally, cases with a stronger mortar at interfaces exhibit the minimum vulnerability index values. This phenomenon can be attributed to the fact that although a stronger mortar increases the maximum strength achieved by each unit, it also induces a more brittle curve. Consequently, the increase in strength is insufficient to compensate for the lack of ductility, leading to a decrease in the seismic vulnerability index.

The same analysis was conducted for the pushovers in the negative direction. Table 20 presents the most relevant parameters evaluated for the different cases for the assessment with the N2 method.

Table 20: Parameters evaluated for the N2 method from pushovers conducted in the negative direction.

		$\Gamma_1$	$m^*$ [ton]	$T^*$ [s]	$q^*$	$\mu_c$	$\zeta_e$
<b>Isolated</b>	Unit 1	1.413	344.1	0.216	2.27	3.74	0.95
	Unit 2	1.411	350.7	0.222	2.76	4.59	0.92
	Unit 3	1.410	346.9	0.216	2.72	4.09	0.84
<b>SC - m<sub>1</sub></b>	Unit 1	1.382	364.2	0.191	2.24	3.21	0.81
	Unit 2	1.382	369.4	0.201	2.44	3.04	0.73
	Unit 3	1.380	366.6	0.214	2.90	3.35	0.68
<b>SC - m<sub>3</sub></b>	Unit 1	1.383	363.5	0.185	2.05	2.91	0.82
	Unit 2	1.383	368.7	0.184	2.47	3.97	0.83
	Unit 3	1.381	366.0	0.200	3.50	4.20	0.64
<b>SC - m<sub>4</sub></b>	Unit 1	1.378	366.5	0.190	1.64	1.89	0.81
	Unit 2	1.378	371.7	0.190	1.99	2.90	0.85
	Unit 3	1.376	369.0	0.197	3.32	3.71	0.61
<b>SC - m<sub>6</sub></b>	Unit 1	1.378	366.6	0.192	1.59	2.28	0.93
	Unit 2	1.378	371.8	0.189	1.88	2.50	0.82
	Unit 3	1.376	369.1	0.197	3.30	3.55	0.60
<b>Fully Connected</b>	Unit 1	1.377	321.2	0.180	1.06	3.30	1.70
	Unit 2	1.377	321.2	0.169	1.35	4.74	1.65
	Unit 3	1.377	321.2	0.176	2.75	3.68	0.70

Similarly to the positive direction, the fundamental mode participation factor and the period  $T^*$  of the equivalent Single-Degree-of-Freedom (SDOF) decrease when there is a connection between units and the rigidity of the connection is enhanced. Figure 96 depicts the equivalent SDOF and bilinearized curves for the Fully connected and Isolated conditions. While Figure 97 displays the same for the Semi-Connected conditions.

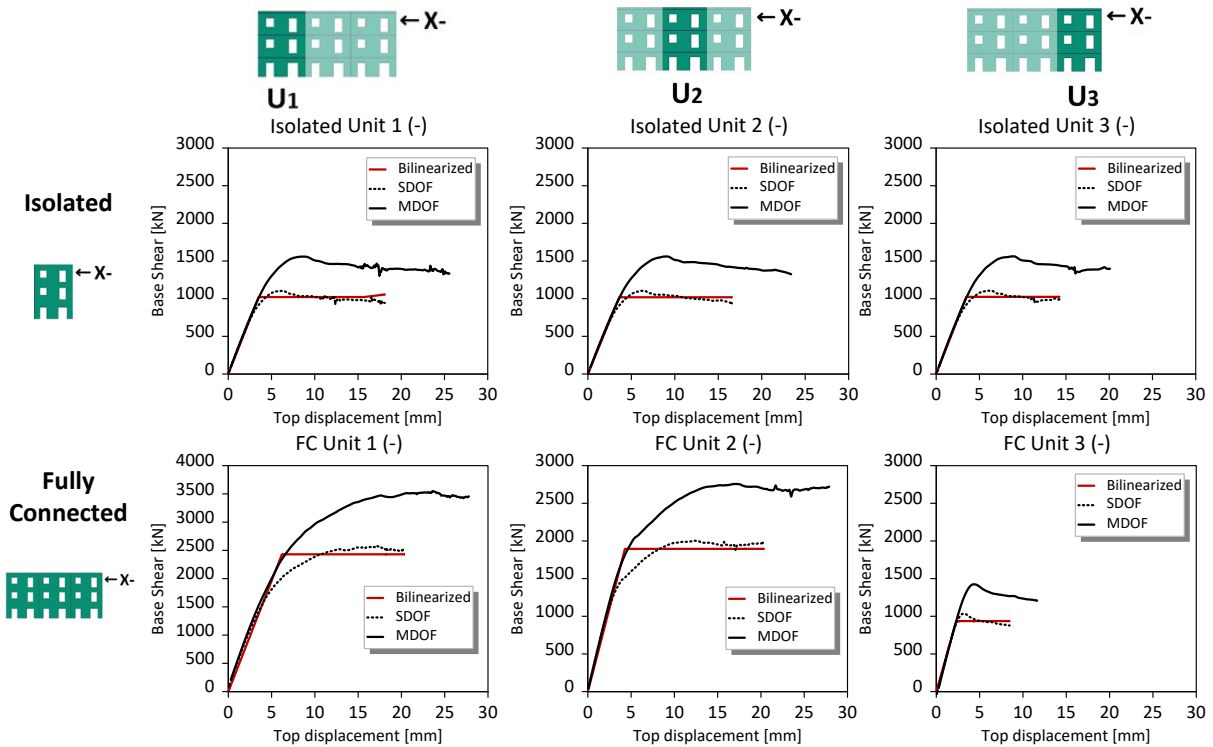


Figure 96: Equivalent SDOF and Bilinearized curves for Fully-Connected and Isolated cases derived from pushovers in the negative direction.

The isolated units exhibit similar curves. In the fully connected condition, Unit 1 displays high resistance and good ductility, while Unit 3 exhibits low resistance and significant brittleness. This disparity is associated with the aggregate effect, which generates confinement in Unit 1 and decompression in Unit 3. Unlike in the positive direction, in this case, the decompressed unit exhibits less resistance, with a very short plastic branch. The distinct behavior observed when structures are subjected to positive or negative loading directions can be attributed to the asymmetrical placement of openings in walls.

Similar observations made for the positive direction curves can be extended to the non-rigid connection between units: when a stronger mortar is assumed at the interface layers, the compressed unit and the central one achieve greater resistance, but the plastic branch tends to be smaller due to increased brittleness. For Unit 3, the decompressed unit, a more rigid connection seems to pose a problem, as it not only reduces the strength but also results in a smaller plastic branch.

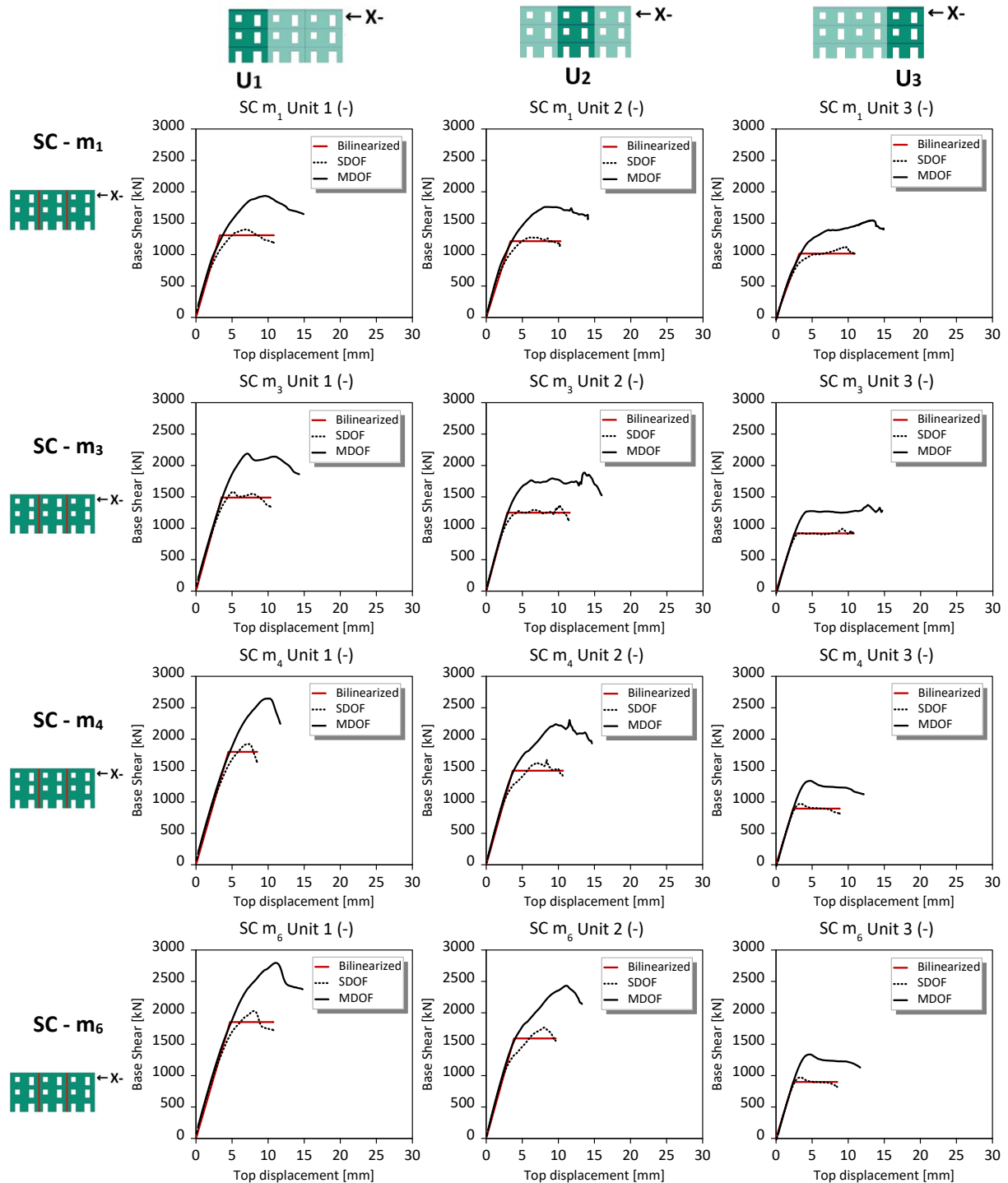


Figure 97: Equivalent SDOF and Bilinearized curves for Semi-Connected cases derived from pushovers in the negative direction.

Referring to Table 20, in the fully connected condition, units 1 and 2 demonstrate a lower value of  $q^*$  and similar value of  $\mu_c$  compared to the isolated condition. Meanwhile, Unit 3 also exhibits similar values of  $q^*$ , attributed to the decompression effect of the aggregate. In the case of Semi-Connected condition, reducing the strength of the mortar layer, the  $q^*$  tends to decrease and  $\mu_c$  increases toward the case of isolated condition. On the other hand, when a stronger



mortar is assumed, unit 1 and 2 reduce both  $q^*$  and  $\mu_c$ . The drastic reduction of  $\mu_c$  is in discrepancy with the case Fully-Connected. Unit 3 maintains value of  $q^*$  and  $\mu_c$  similar to isolated and fully connected also in the case of Semi-connected.

Figure 98 shows the vulnerability indexes trend evaluated for all the models analysed.

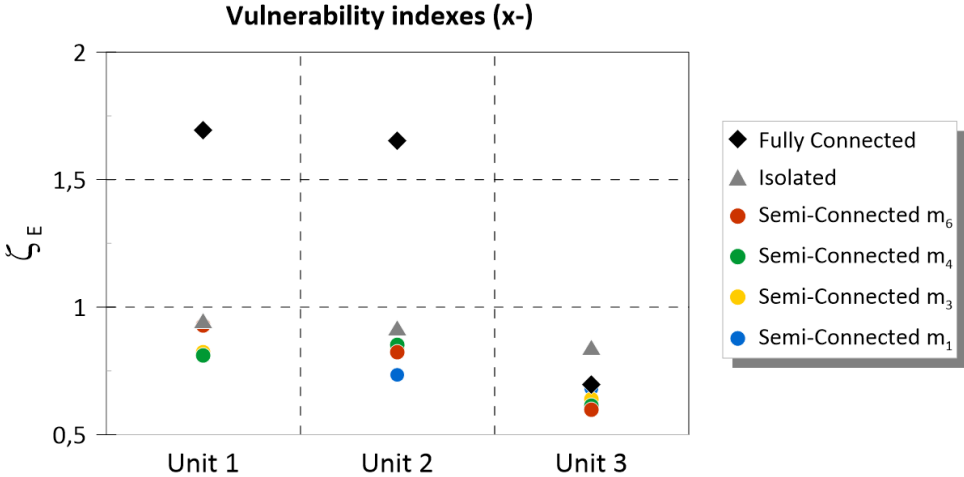


Figure 98: Vulnerability indexes comparison for pushovers in negative direction.

In this scenario, only Unit 1 and Unit 2 verified when they are related to the Fully Connected condition. Units in the isolated and Semi-Connected conditions do not satisfy seismic verification. The indexes related to the Semi-Connected case are lower than the isolated case in all cases.

In the negative direction, the decompression caused by the aggregate effect is so significant that the vulnerability of Unit 3 is higher when it is rigidly connected to other units compared to when it is isolated. Comparing positive and negative loading directions, it can be noted that Unit 2 consistently exhibits lower vulnerability when a Fully Connected configuration is adopted. However, the vulnerability of external units can change drastically depending on whether the load is applied in one direction rather than the other.

Based on the assessment conducted through the N2 method, it can be concluded that the Semi-Connected condition exhibits higher seismic vulnerability compared to the other models. However, it's crucial to recognize that this assessment method, which considers bilinearization into an elastic-perfectly plastic behaviour, might not be the most appropriate for cases where the loss of resistance is not associated with the failure of the building but rather with the disconnection between structural units. Therefore, further analyses and considerations

regarding the behaviour and structural response were made to fully understand the implications of the Semi-Connected condition in terms of seismic vulnerability.

## **8.4 Non-linear dynamic analysis results**

The non-linear dynamic analysis was conducted on the structure, utilizing the ground acceleration data recorded by the Colle Grilli station (L'Aquila) in 2009, specifically in the building's longitudinal direction. The aggregate was studied assuming the different degree of connection between units proposed and compare results with previous analyses.

Figure 99 depicts the individual base reactions of each unit relative to the displacement of the barycentre of the third floor of each unit, whereas Figure 100 illustrates the reaction of the entire aggregate building, with the displacement assumed to be related to the node on the central unit. In the case of isolated units, each unit was analysed independently, without considering their collective response.

Figure 99 explicitly illustrates how the dynamic response of each unit varies based on different degrees of connection. The connections between units not only influence their strength but also affect the distribution of stress between them. When Unit 1 is assumed isolated, it responds similarly to both negative and positive forces. However, by connecting Unit 1 to adjacent units and reinforcing their connection, its resistance improves in the negative direction but diminishes in the positive direction. This is attributed to the aggregate effect, where Unit 1 experiences confinement under negative forces and decompression under positive forces. Conversely, Unit 3 demonstrates the opposite trend: a stronger connection results in higher resistance when pushed in the positive direction and lower resistance in the negative direction. Meanwhile, the central unit consistently benefits from the aggregate effect: with a reinforced interface, its resistance increases regardless of the direction of force applied. In the charts, the envelopes of dynamic tests exhibit correspondence with pushover curves.

Semi-connected cases demonstrate intermediate trends between isolated and fully connected units. Increasing the degree of connection leads to greater structural resistance, with a tendency to maintain predominantly elastic behaviour and reduce maximum displacements reached.

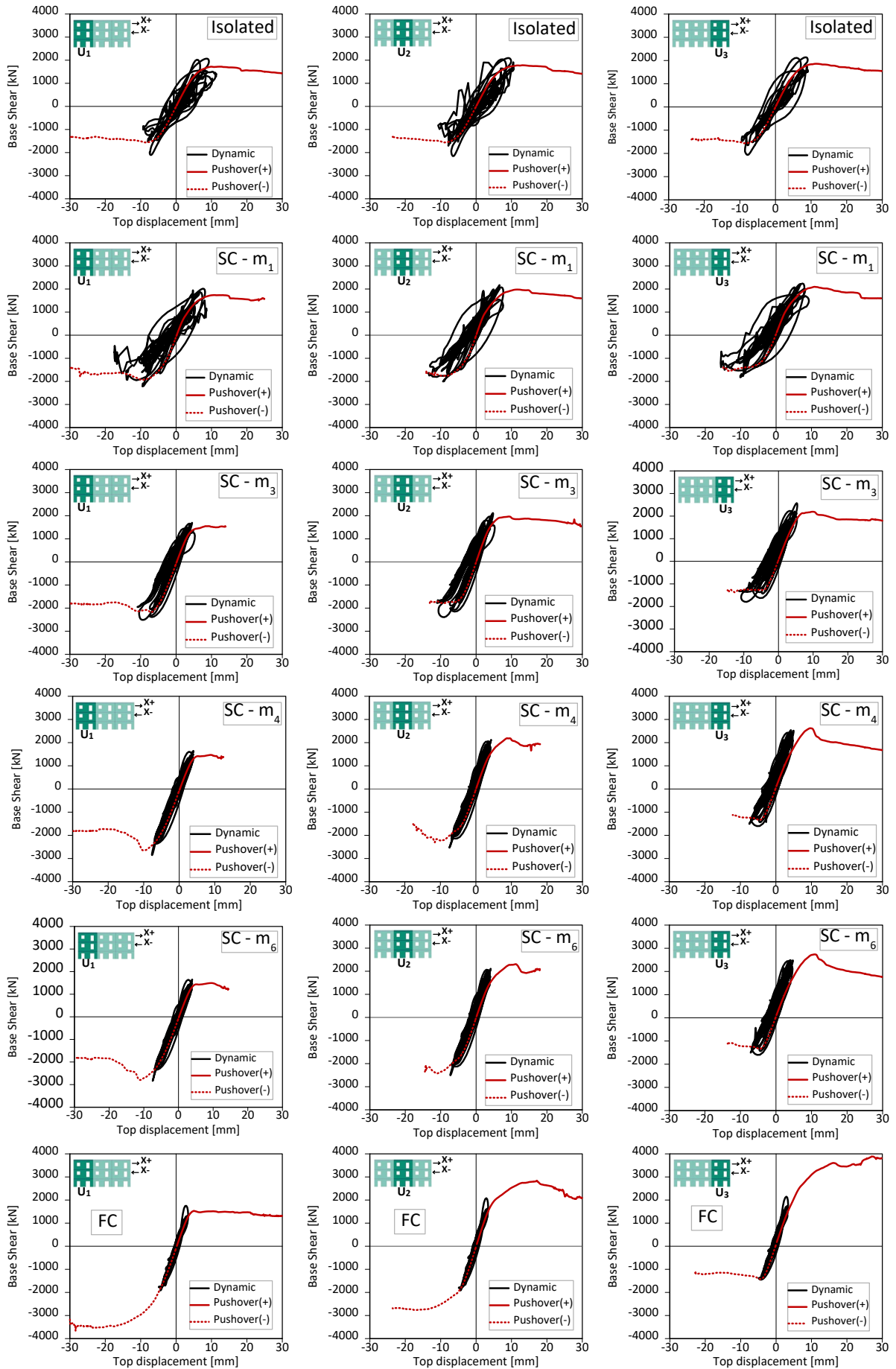


Figure 99: Non-linear dynamic analysis showing the individual reactions of each unit.

The aggregate reactions shown in the Figure 100 demonstrate that with a rigid connection between units, such as in fully connected and semi-connected configurations with mortar  $m_4$  or  $m_6$ , the aggregate largely maintains an elastic response to seismic activity. Conversely, when a less rigid connection between units is assumed, the dynamic input causes some elements to exceed their elastic limit, resulting in plastic deformation.

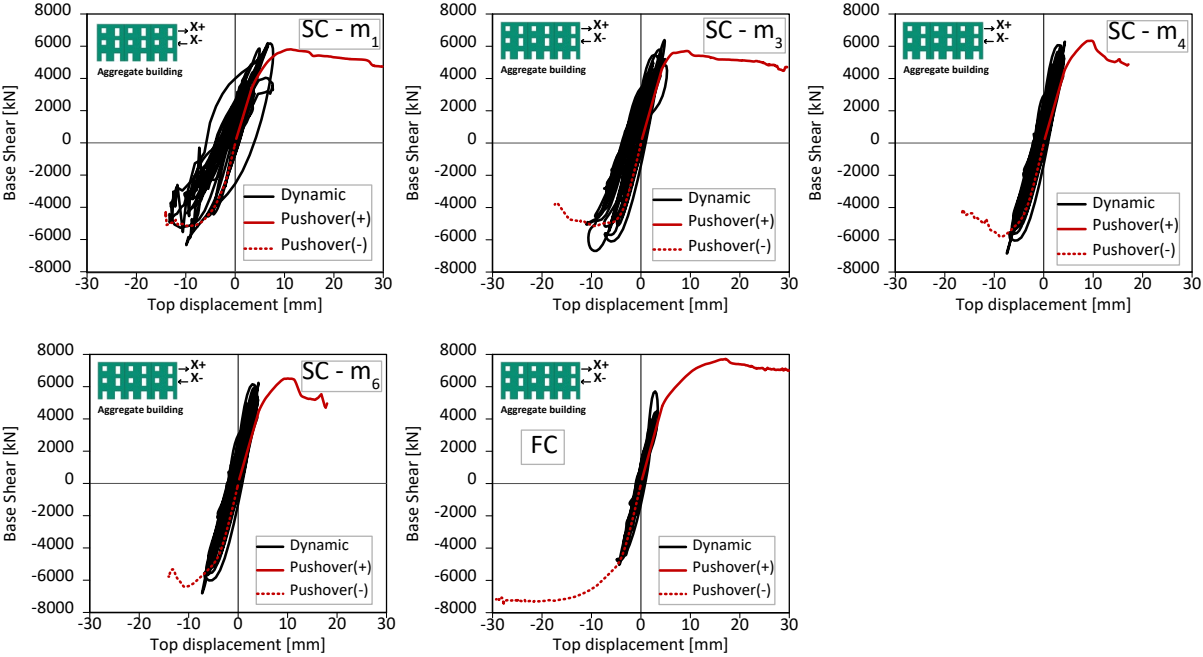


Figure 100: Nonlinear dynamic analysis results on aggregate building.

The dynamic analysis related to isolated units and semi-connected units with the weaker mortar ( $m_1$ ) at the interface could not be completed due to the units reaching collapse. In these cases, the failure occurred at time  $dt=3.8$  s, after the maximum acceleration was applied (as shown in Figure 101). However, the dynamic analysis for the other models was fully completed.

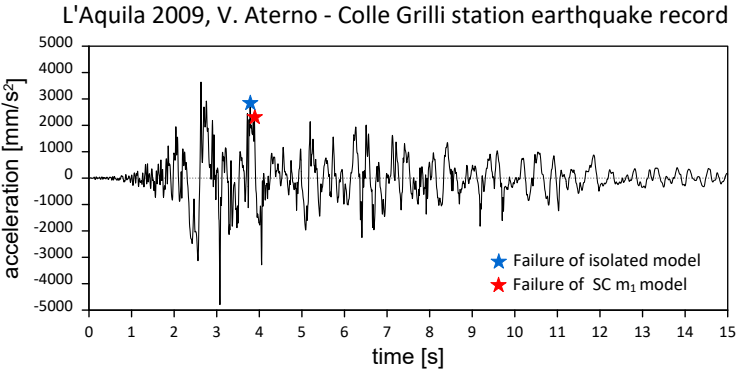


Figure 101: Acceleration record with highlighted point indicating the interruption of dynamic analysis for Isolated units and Semi-Connected  $m_1$  case.

Figure 102, 103 and 104 illustrate damage plots resulting from dynamic analysis for the different models, considering each unit's longitudinal walls. The damage plot shows both tensile cracking and crushing during seismic analysis. Notably, the front wall exhibits the most damage compared to the other two scenarios due to its higher number of openings, which increase its flexibility and therefore its displacement demand.

Reduced damage is evident when the degree of connection between units is more rigid. In isolated conditions, substantial damage is visible, indicating unit failure and an inability to withstand higher stresses: the front wall pillars have collapsed. Similarly, in the case of Semi-Connected  $m_1$  models, a high level of damage is observed, signifying failure achievement. However, this damage is comparatively smaller than that observed in the isolated model. Assuming a stronger mortar at interfaces, Semi-Connected models exhibit a lower degree of damage, gradually approaching the damage pattern of Fully Connected models, which demonstrate the least damage among all cases.

The Fully-Connected model shows limited damage, indicating that its response to seismic input was predominantly elastic.

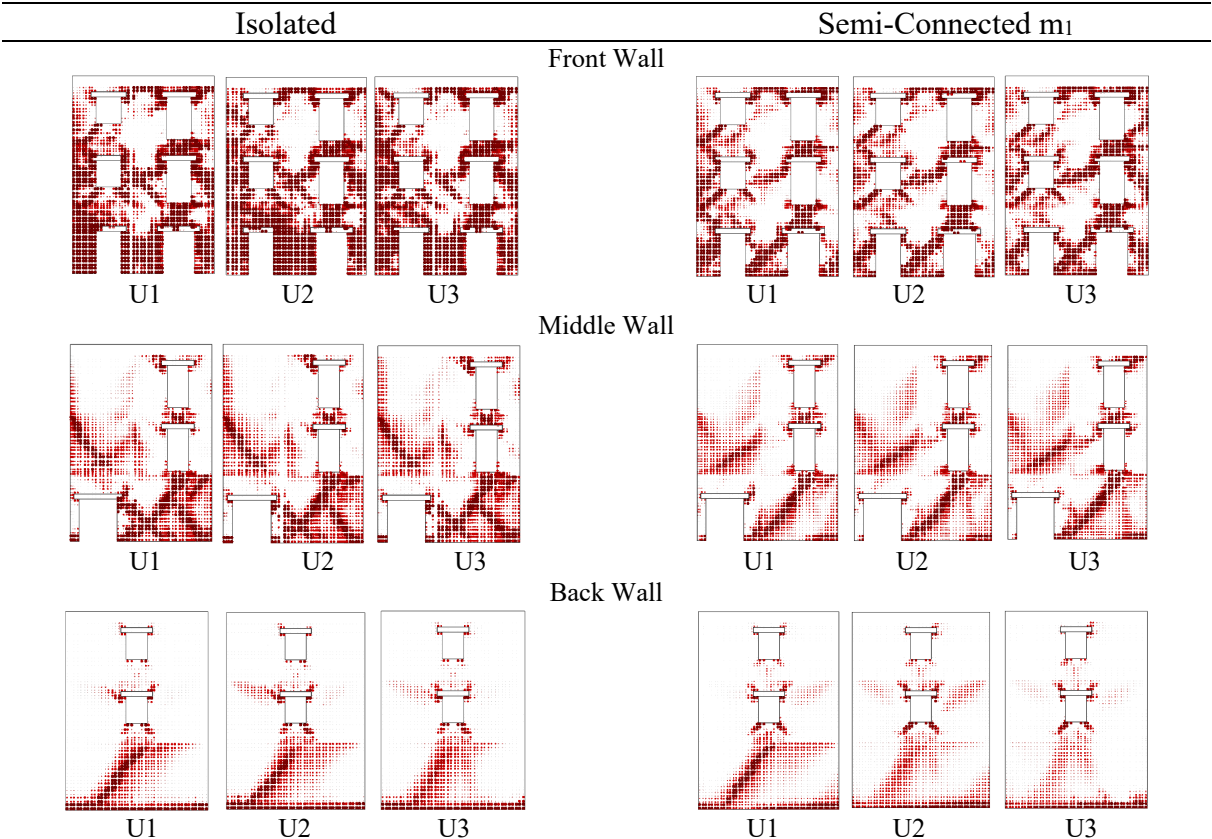


Figure 102: Damage plot from dynamic analysis for Isolated and Semi-Connected  $m_1$  models.

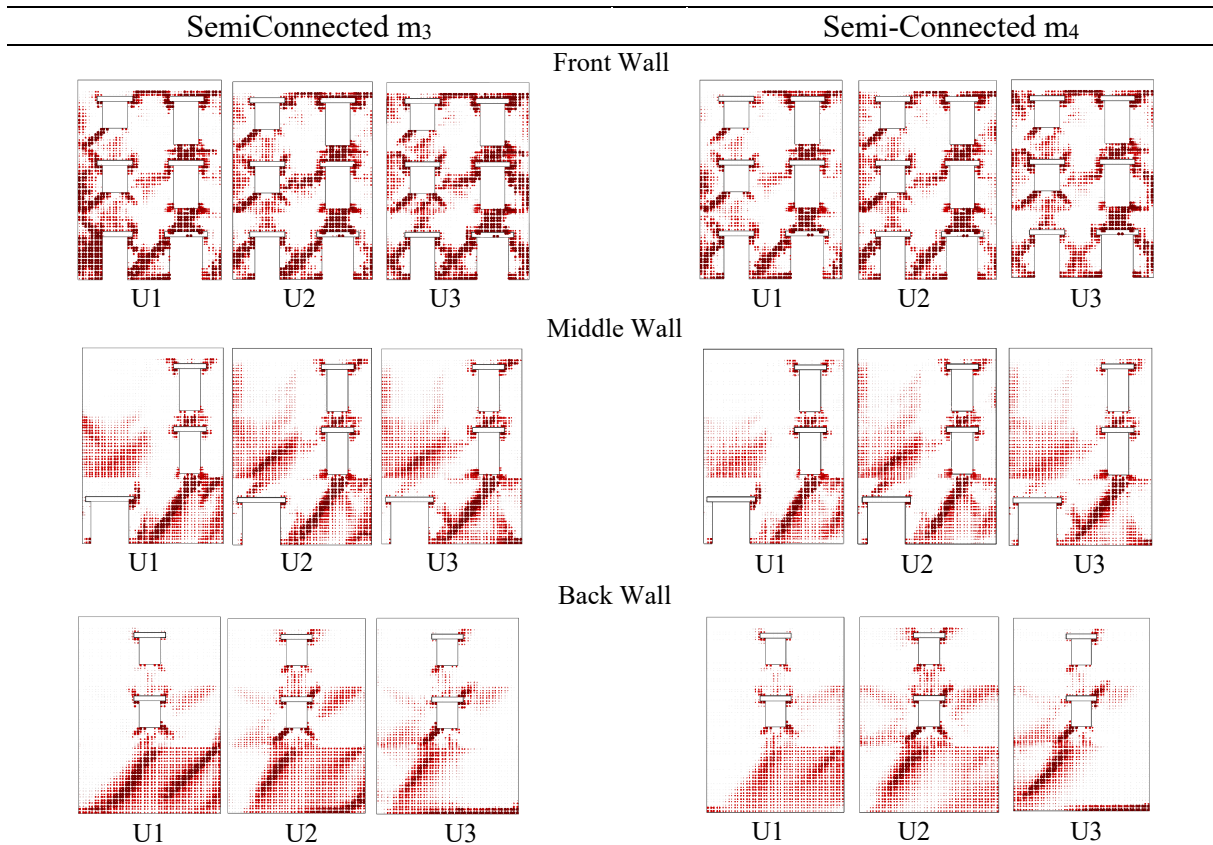


Figure 103: Damage plot from dynamic analysis for Semi-Connected m<sub>3</sub> and Semi-Connected m<sub>4</sub> models.

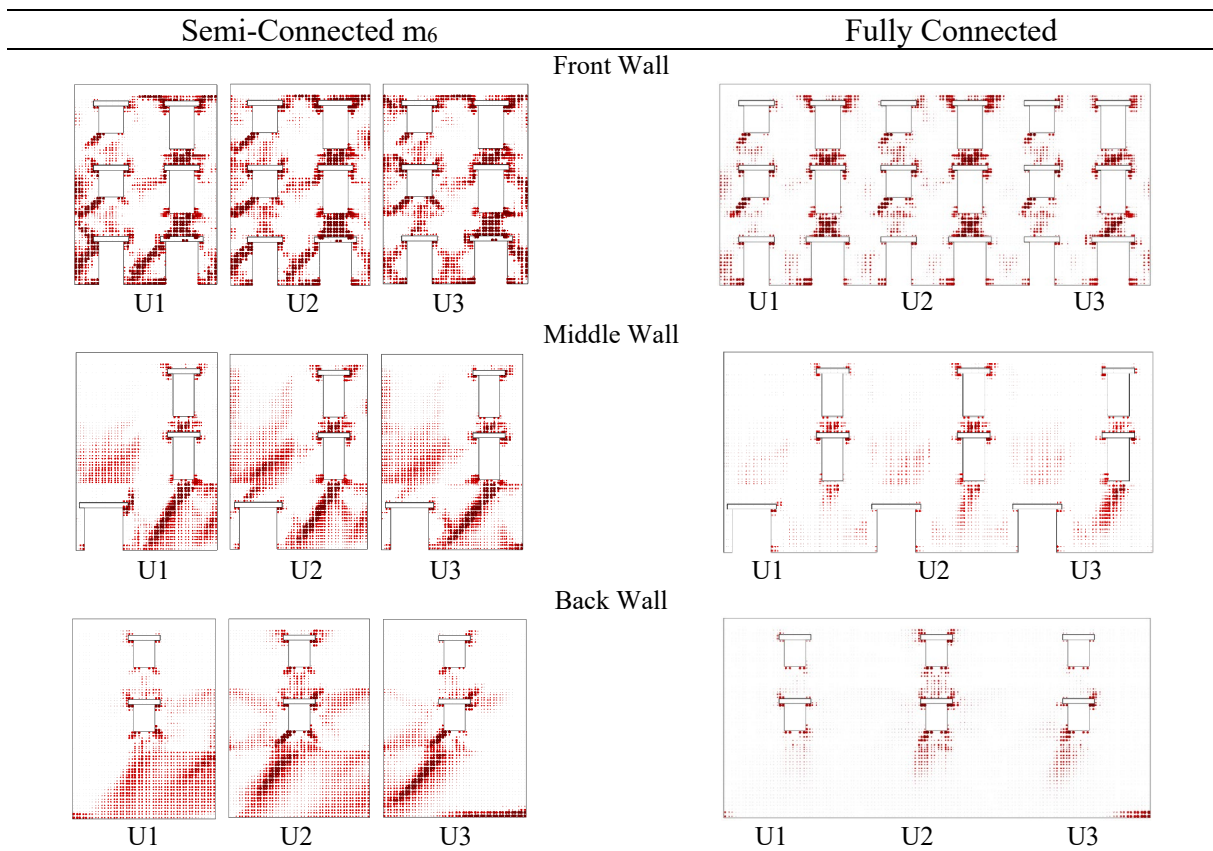


Figure 104: Damage plot from dynamic analysis for Fully Connected and Semi-Connected m<sub>6</sub> models.

The dynamic analysis reveals that the Semi-Connected models exhibit behavior that falls between isolated and fully connected units. When the structure was modeled as isolated and Semi-Connected with mortar  $m_1$ , numerous elements achieve plastic deformation and ultimately failed. In contrast, in other cases, the models successfully completed the dynamic analysis, indicating that a stronger connection between units resulted in reduced structural damage.

### 8.5 Results comparison and discussion

From the conducted analyses, it was found that units modelled as Fully Connected benefit from the aggregate effect: both the compressed external unit and the central unit exhibit increased resistance compared to the isolated case. However, the aggregate effect may have a negative impact on the decompressed external unit, as shown in the pushover analyses, which can lead to lower vulnerability indexes compared to the isolated case. The results of the analyses are controversial regarding the Semi-connected case. This chapter provides explicit comments on the observed phenomena and compares the different results.

Figure 105 displays the pushover curves in the positive direction for each unit in all models.

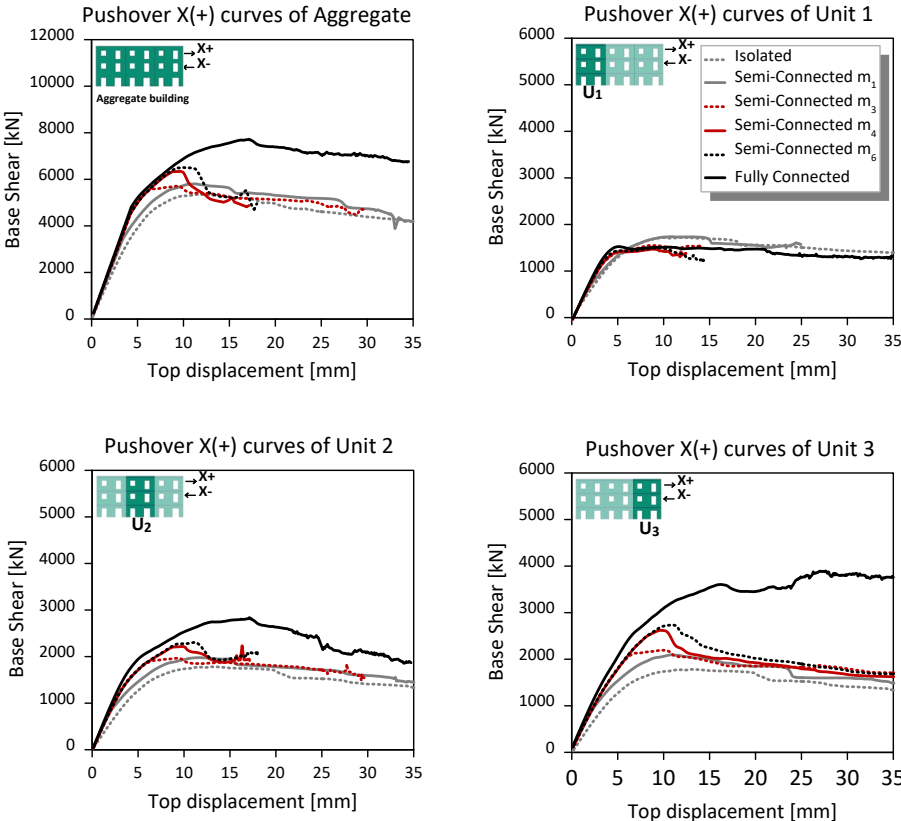


Figure 105: Pushover curves in the positive direction evaluated for each unit.

Improving the degree of contact between each unit leads to an overall increase in aggregate resistance. This phenomenon is evident in the overall aggregate reaction and in the curves related to Unit 2 and Unit 3. Meanwhile, Unit 1 is influenced by the decompression produced by the aggregate effect, resulting that the higher base reaction is achieved in the case of isolated respect other cases. Examining the curves related to the Semi-Connected condition for Unit 2 and 3, it becomes evident that enhancing the resistance of the interface mortar results in an increasement of the unit resistance. However, this improvement is accompanied by a more brittle failure, characterized by resistance drop after the achievement of the peak resistance.

Figure 106 displays the pushover curves in the negative direction of all models for each unit. It can be observed that by enhancing the degree of connection between units, both the aggregate reaction and the reaction of Unit 1 and 2 increase.

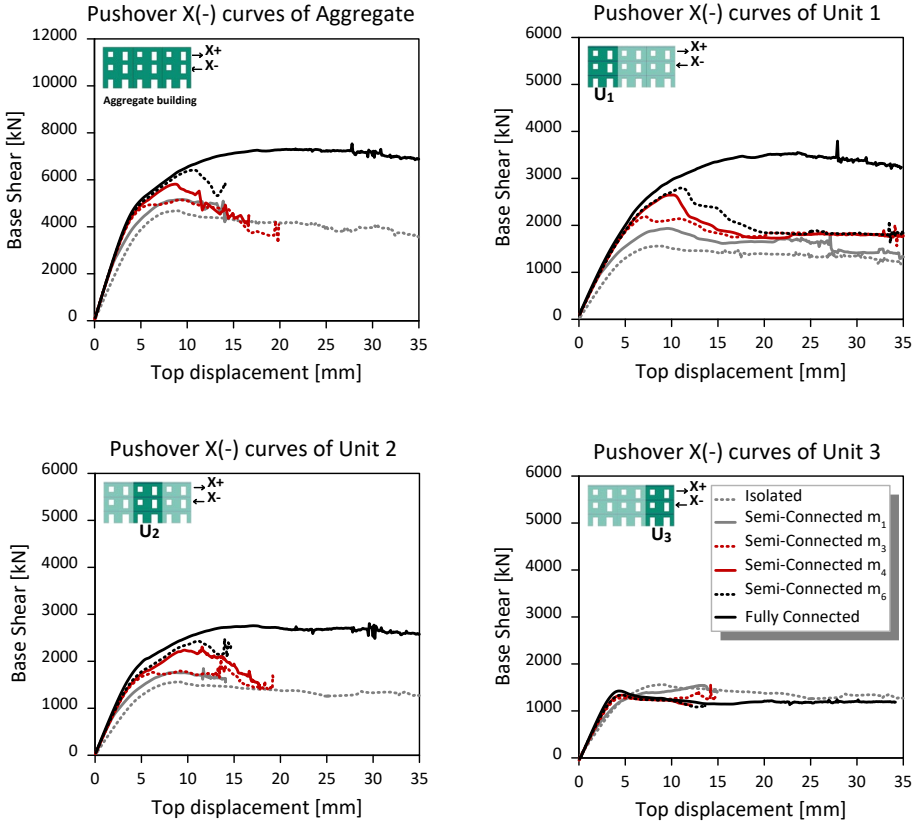


Figure 106: Pushover curves in the negative direction evaluated for each unit.

Unit 3 experiences decompression, resulting in a reduction of its reaction. Although the aggregate displays increased resistance globally, Unit 3 reaction diminishes when the units are more rigidly connected. In the Semi-Connected case, after reaching the peak, the curves tend to drop, indicating brittleness and converging towards the behaviour observed in the curves of isolated units. In pushover analyses, for Semi-Connected cases, an increase in the stiffness of



the connection degree results in higher resistance for both the central and compressed external unit, but it also leads to much more fragile curves. Additionally, in both directions of the analysis aggregates showcased a tendency to return to the resistance level of the isolated case after a decay in resistance. This decay in resistance was therefore studied in detail by observing the damage patterns.

Regarding crack patterns, the conventional failure assessed from the pushover trends does not align with any damage or kinematics that could justify unit resistance limit. The achievement of the maximum base reaction is actually reached in correspondence with the failure of the mortar placed at the interface between the units to simulate a non-rigid connection. This suggests that the tendency towards the isolated unit resistances is due to the loss of the aggregate effect caused by the rupture of the mortar.

As an example, the curve for Unit 3 in the Semi-Connected  $m_6$  case with push in the positive direction is provided. Figure 107 depicts the pushover curve as well as the crack patterns recorded at the peak, conventional failure instant, and real failure instant. In the example, a noticeable softening branch develops once Unit 3 moves away from the other two units.

The reduction of the resistance can be justified with the loss of the aggregate effect due to the failure of the mortar and not by the failure of the structure. This phenomenon is observed in the cases where mortar is most resistant as it develops a higher initial increment in structural resistance.

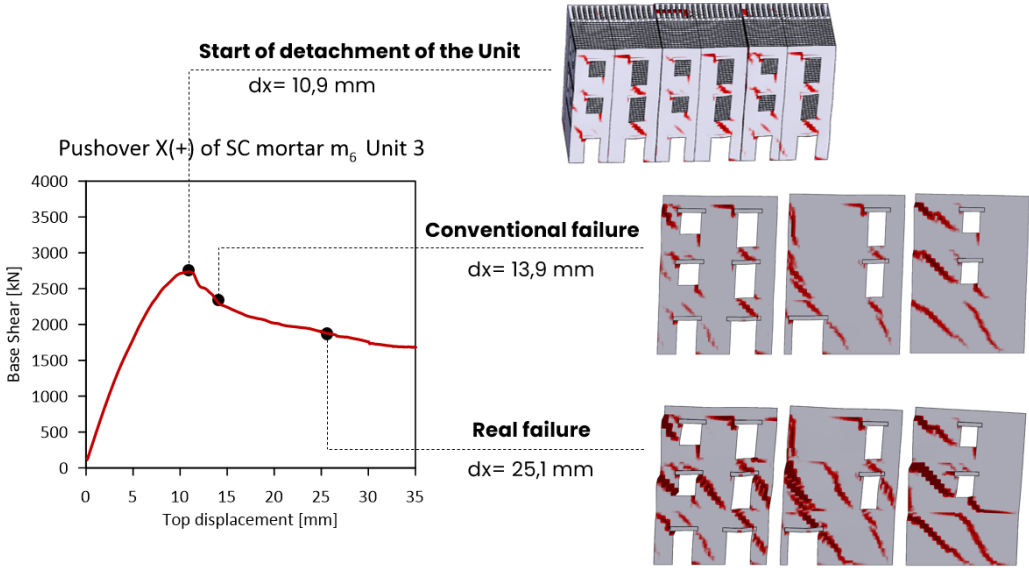


Figure 107: Pushover in X+ for Unit 3, Semi-Connected  $m_6$ .

The application of the N2 assessment method on the pushover curves indicates that in the semi-connected case, seismic vulnerability is even greater compared to units modelled as isolated. Figure 108 shows the vulnerability indexes for both the positive and negative directions. In almost all cases, the indexes related to the Semi-Connected condition are lower compared to fully connected and isolated configurations. This happens because while assuming a mortar with greater resistance at the connection between units results in an increase in resistance in the pushover curves, this increase is not sufficient to compensate for the significant loss of ductility showcased in the capacity curve when the interface mortar breaks.

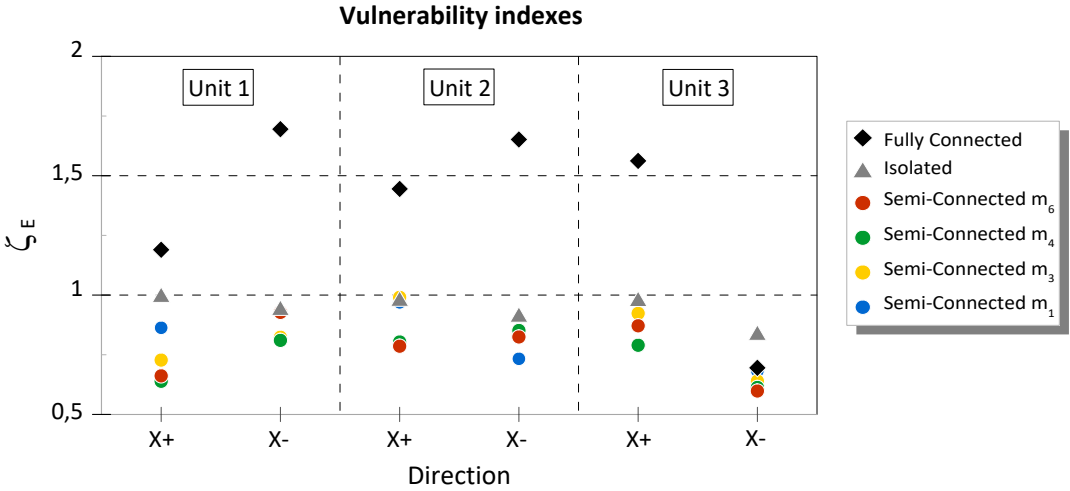


Figure 108: Vulnerability indexes related to pushovers in positive and negative direction.

While the N2 method results in a lower vulnerability index for cases with higher interface resistance, dynamic analysis shows opposite results, indicating that the aggregate effect is beneficial. When a stronger interface is assumed between units, the aggregate better withstands seismic action. With the seismic input remaining constant, the damage is reduced when a stronger connection exists between units within the aggregate.

Dynamic analysis elucidates how the Semi-Connected cases exhibit an intermediate trend between Fully Connected and isolated cases, as reflected in section 8.4. Additional insights are provided in Figure 109, where the crack patterns corresponding to the various cases at the end of the non-linear dynamic analysis are presented. These patterns exclusively depict cracks associated with tensile stress. The more rigid the connection between units, the less visible cracks appear in the models.

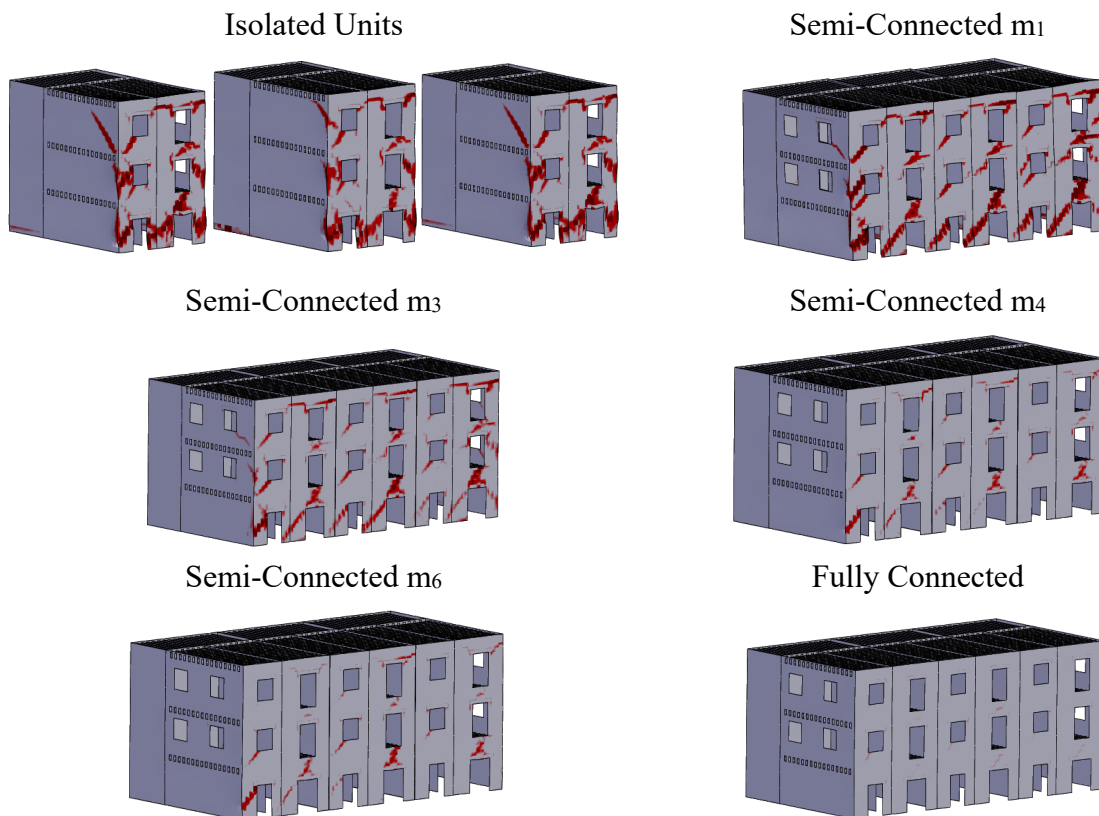


Figure 109: Dynamic analysis crack pattern 3D.

Figure 110 displays the damage plot at the end of the analysis of Unit 1 across three scenarios: fully connected, semi-connected with mortar  $m_4$ , and isolated. These cases were selected to emphasize the difference between rigidly connected units, isolated and an intermediate boundary connection considering a degrading interface.

The reduced damage of the unit is evident when the degree of connection between units is more rigid. In the isolated condition, significant damage is visible, indicating unit failure and the inability to withstand higher stresses. In the Semi-Connected case with mortar  $m_4$ , the damage is greatly reduced, but remains fairly distributed across the ground floor pillars and spandrels between the openings of the front wall. The damage to the middle and back walls is much less pronounced in the Semi-Connected case compared to the isolated one. The Fully Connected configuration exhibits limited damage, suggesting maintenance within the elastic regime of the elements.

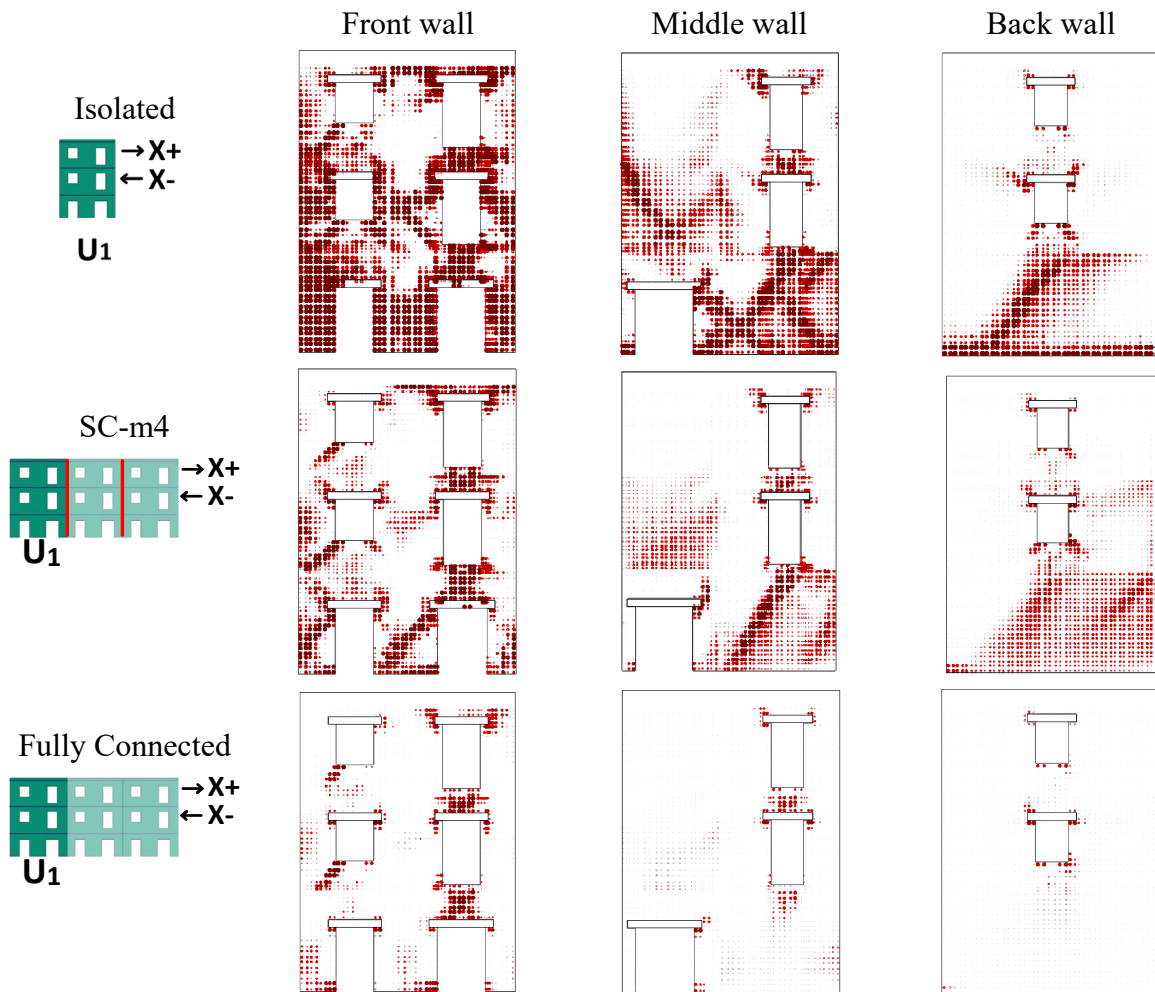


Figure 110: Damage plot resulting from non-linear dynamic analysis.

It can be concluded that there is a discrepancy between the vulnerability assessment provided by the N2 method and the level of damage evaluated in dynamic tests and pushover analyses. This can be attributed to the fact that the N2 method focuses on the reduction of resistance at a global level, neglecting local damage or effects, such as the loss of the aggregate effect due to mortar failure at interfaces.

The N2 method utilized for assessment in this research is reliable for fully connected cases and for units modelled as isolated. However, for Semi-Connected configurations, where the disappearance of the aggregate effect leads to an "apparent" brittle failure, the method underestimates the capacity of the units.

The challenge related to masonry aggregates also involves selecting the most appropriate modelling method to accurately capture and assess it. An alternative bilinearization criterion should be employed to account for the effect of mortar failure at the interface in the case of Semi-Connected aggregate.

Peter Fajfar and Matjaz Dolsek proposed a new  $q$ - $\mu$ - $T$  relation in reference in (78), which can be applied to structural systems where the failure of certain secondary structural elements leads to a global strength degradation, while the primary structural system continues to bear loads. In (79) the same authors utilized this method to assess the vulnerability of a reinforced concrete frame structure with masonry infills. The presence of infilled masonry significantly impacts the response of the global frame. Although masonry infills increase the overall resistance of the building, they are very fragile, and their contribution disappears at low levels of deformation. Even after infill failure, the frame continues to support loads. Essentially, infills act as secondary elements, and their failure leads to a degradation in overall strength but not necessarily to the collapse of the entire structure.

A similar scenario arises with the "aggregate effect" on the behaviour of individual units within an aggregate building. The behaviour of the individual unit is strongly influenced by the aggregate effect, until the connection between units is lost and the structure tends to behave as if it were isolated. The greater the mechanical properties of the mortar used at the interface layer, the more significant will be the impact of the aggregate effect on the unit's behaviour, both in terms of resistance and increase in degradation when the mortar interface breaks.

Therefore, it is considered beneficial to attempt utilizing other assessment methods for units modelled as Semi-Connected, despite the N2 method being the one proposed by regulations.

## 9. Conclusion

The analysis and modelling of unreinforced masonry aggregate buildings present a highly complex procedure due to numerous factors influencing the response of individual units, with one of the most relevant being the degree of connection between them. The absence of specific guidelines has led to the adoption of simplifications in practice, such as modelling units in isolation from adjacent ones, thus neglecting the "aggregate effect". This study focuses on assessing the effect of a different degree of connection between units using modal, nonlinear static, and nonlinear dynamic analyses. Additionally, it explores whether the current most used method for assessing seismic vulnerability of buildings is suitable for this context.

A 3D finite element model was developed to simulate a masonry aggregate building consisting of three similar units, each with three stories. The model utilized 2D shell elements to represent the structural components. To accurately capture the behaviour of masonry while maintaining computational efficiency and accuracy, a homogenized masonry approach was employed. The model was implemented in STKO, using a Layered Shell section with the *ASDShellQ4* element. Physical properties were assigned using *ASDConcrete3D* for masonry and *DamageTC3D* for mortar. The integration of the *IMPLEX* algorithm with model partitioning in *OpenSeesMP* ensured time-efficient analyses.

Units were modelled considering three different boundary conditions: first, individually as isolated units; second, as rigidly connected structures referred to as "Fully-Connected"; and third, with an intermediate connection type, named "Semi-Connected" configuration, where a degrading layer of mortar between the longitudinal walls of the units was implemented. For the intermediate connection, four mortars with varying mechanical properties were included at the interface to evaluate how different strengths of connection might impact the structural behavior. Each mortar was characterized in terms of friction and cohesion.

Each model was dynamically characterized by conducting a modal analysis. Pushover analyses were conducted in both positive and negative longitudinal directions, considering lateral force distributions proportional to the fundamental mode. The seismic vulnerability of each unit, considering the different degrees of connection within the aggregate, was evaluated using the N2 method. Finally, the models were subjected to nonlinear dynamic analysis, utilizing the L'Aquila earthquake in the longitudinal direction as the seismic input.

The results reveal that when a connection between the units that constitute the aggregate is considered, their response differs significantly from their isolated behavior. This difference is highly dependent on the relative position of the unit being examined within the aggregate and the direction of the load. In fully connected conditions, the aggregate effect enhances the overall resistance of the structure and induces compression on the leeward unit, thereby increasing its strength, while reducing resistance in the windward unit. Conversely, in isolated configurations, all three units exhibit similar behavior, both in the positive and negative directions.

When the mortar layer is introduced between the longitudinal walls of units, assuming a stronger mortar enhances the overall resistance of the aggregate. However, pushovers reveal a more brittle behavior, attributed not to the failure of the units themselves, but to the mortar failing at the interfaces between units, resulting in the loss of the aggregate effect. Once the mortar layers fail, the pushover curves exhibit a softening branch that converges towards the curves associated with isolated conditions. This phenomenon is particularly evident when the mortar is highly resistant, leading to a significant initial increase in structural resistance. Conversely, when the mortar is weaker, the results tend to align with the trend of isolated units. Results show that both the rigid diaphragm and high degree of connection are fundamental to the development of the aggregate effect as it ensures load transference in the longitudinal direction (due to the connection between units) and in the transverse direction (due to the rigid diaphragm)

The N2 method used for seismic assessment tends to judge cases with non-rigid connections between units as more severe compared to isolated ones. This is because it only accounts for the overall resistance, ignoring other factors that could affect the response of structures, even if they don't lead to collapse, such as when the connection between units breaks. The crack patterns observed in pushover tests imply that the conventional failure criteria, considered in the N2 method, doesn't accurately represent structural collapse. Furthermore, damage from nonlinear dynamic analysis indicates that semi-connected configurations fall between isolated and fully connected structures, with reduced damage observed in configurations with stronger mortar. Consequently, connecting units with increasingly rigid connections gradually leads to beneficial results due to the aggregate effect.

The classic N2 method provides reasonable results for isolated and fully connected cases. However, for Semi-Connected cases, where fragile curves are observed in pushovers, another bilinearization approach should be employed, such as the one proposed in (78). This criterion

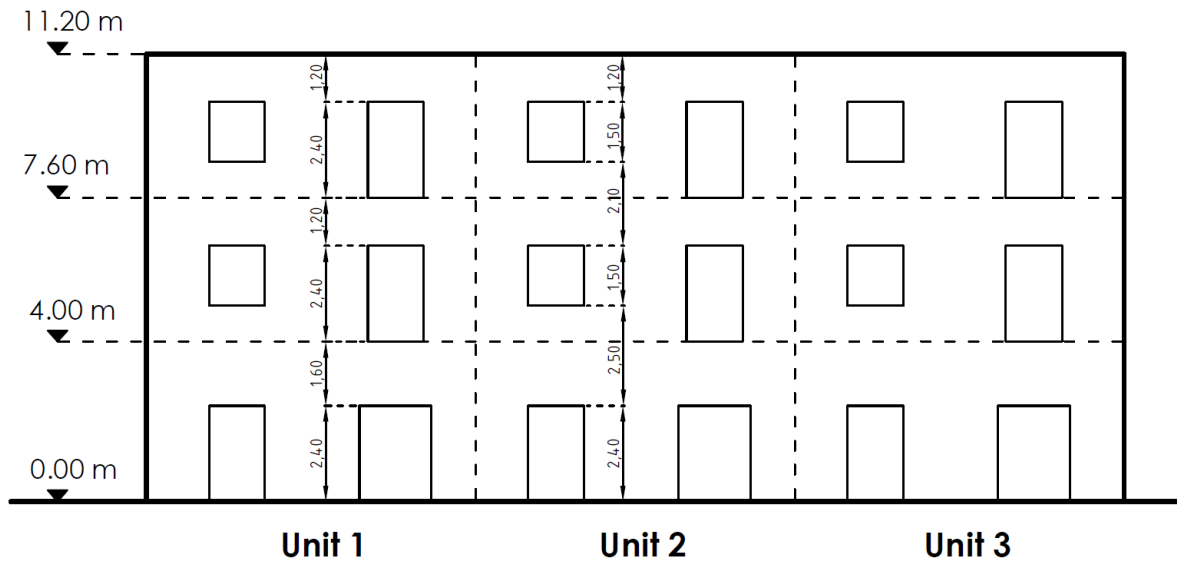
was developed for infilled frame models to consider the rupture of infills, which drastically reduces the global resistance while the frame continues to resist. The proposed bilinearization system can be extended to units modeled as Semi-Connected, where the aggregate effect is the secondary factor influencing the global response, but when it disappears, it does not lead to actual structural failure.

Potential extension to this work involves abandoning the assumption of a rigid diaphragm and examining how the distribution of forces between longitudinal walls changes with a flexible diaphragm. Additionally, future studies could statistically evaluate dynamic responses to various seismic inputs, expanding beyond the single input considered in this context. Furthermore, it's interesting to consider the influence of other factors such as diverse planometric geometries among units, variations in masonry quality, and the effects of non-rigid connections between orthogonal walls. This exploration would contribute to a deeper understanding of the complex behavior exhibited by these structures.

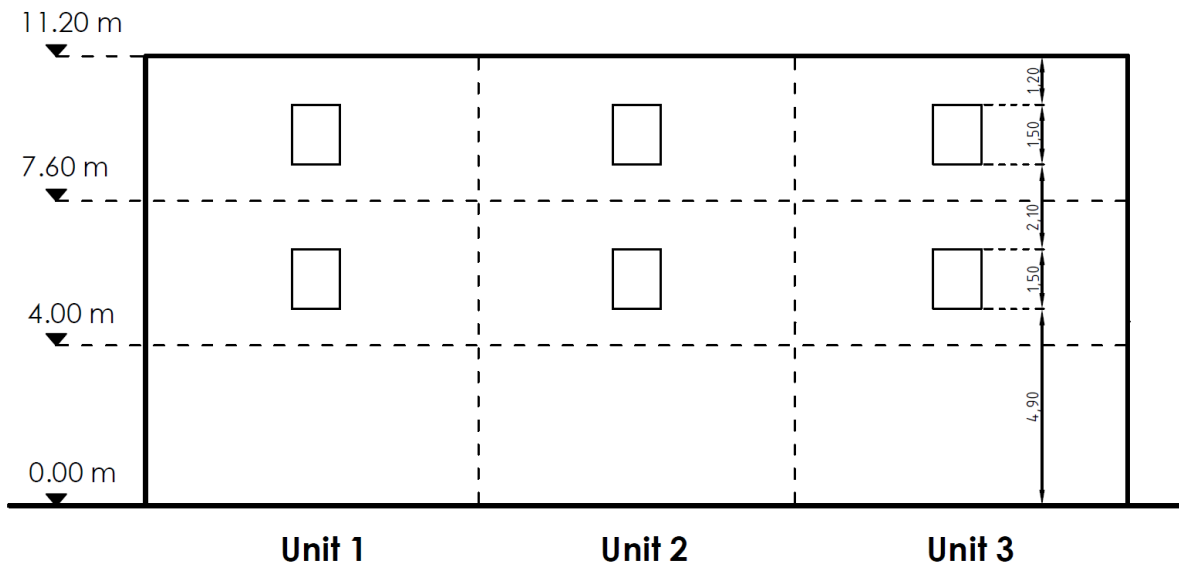


# Appendix A

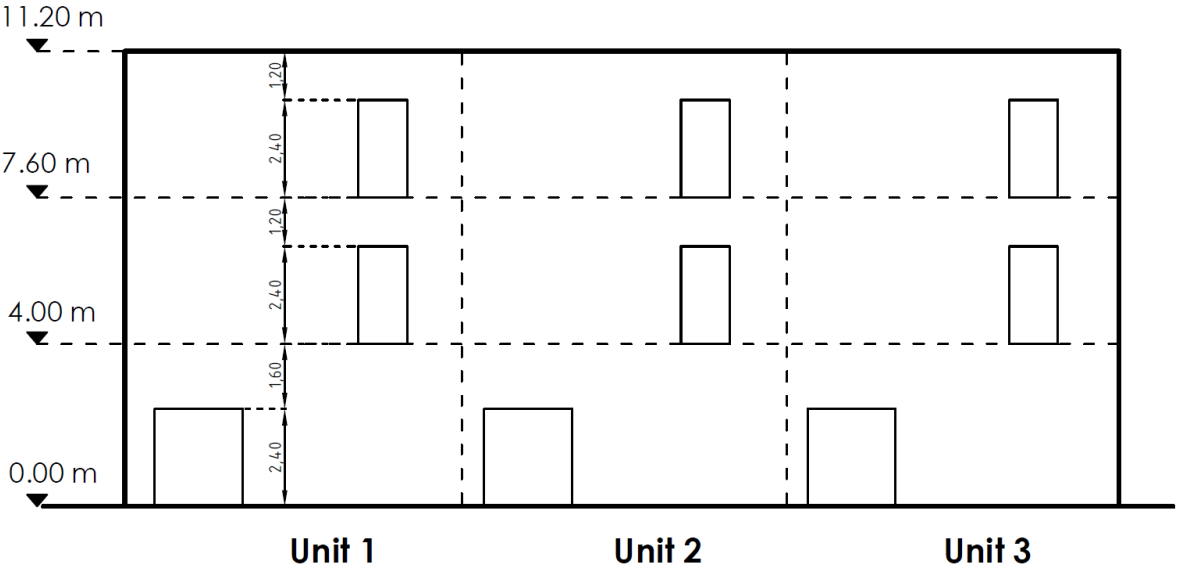
## Front Wall



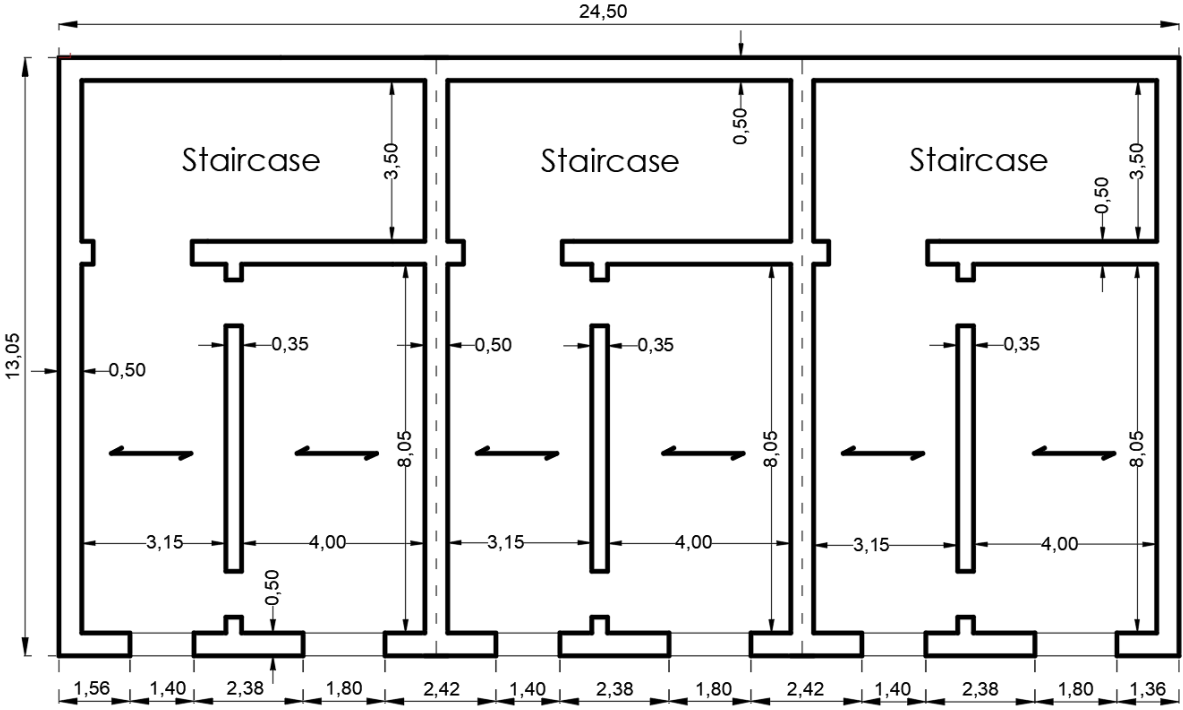
## Middle Wall



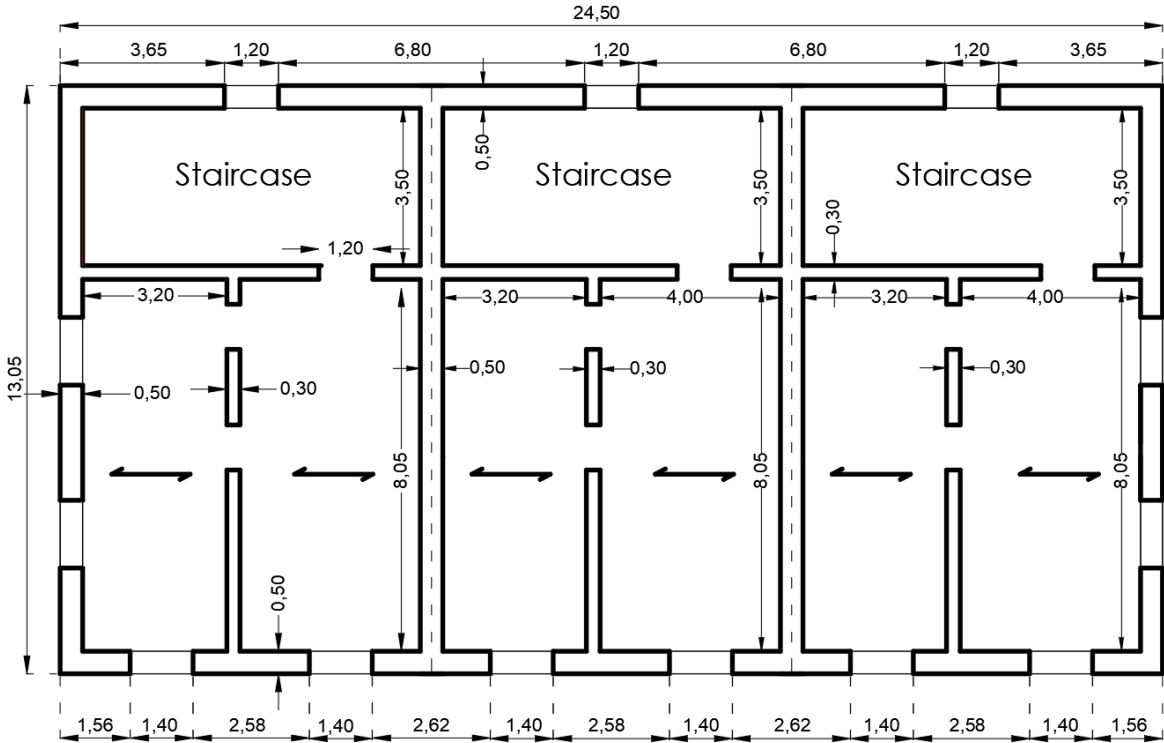
Back Wall



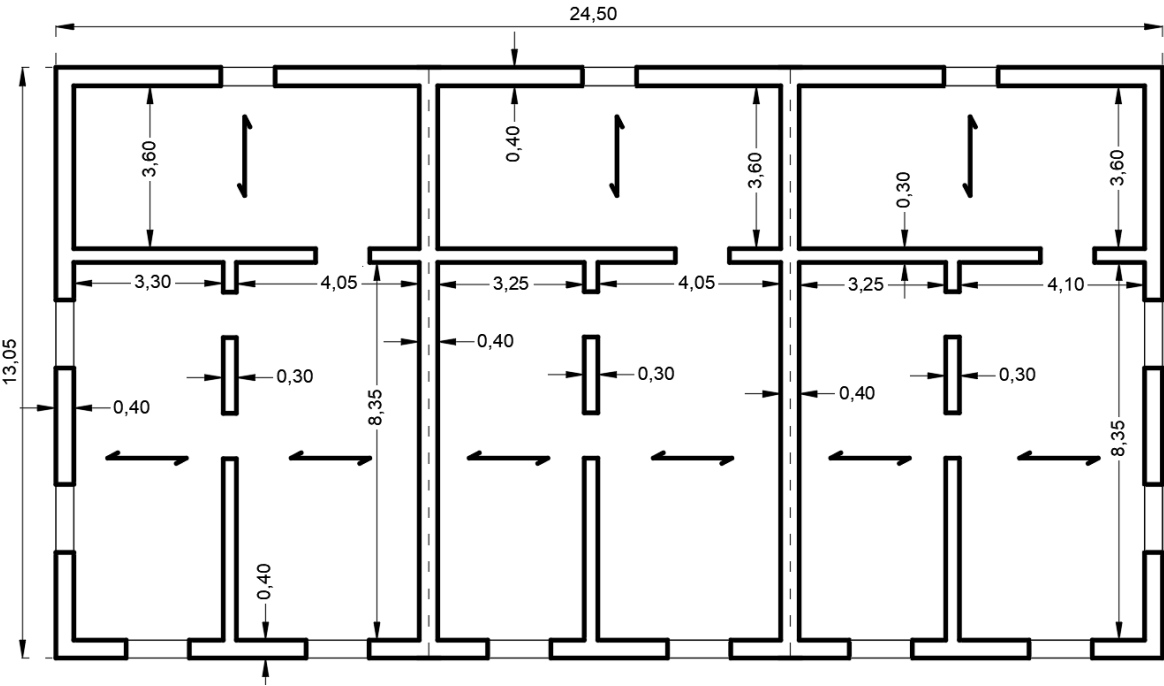
First Floor



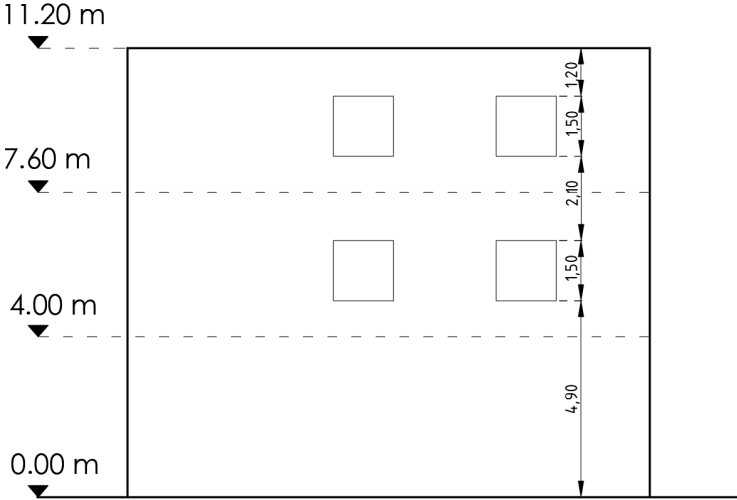
Second Floor



Third Floor



Trasverse Wall



# References

1. Carocci CF. Small centres damaged by 2009 L'Aquila earthquake: on site analyses of historical masonry aggregates. *Bull Earthq Eng.* 2012;10(1):45-71. doi:10.1007/s10518-011-9284-0
2. Angiolilli M, Lagomarsino S, Cattari S, Degli Abbati S. Seismic fragility assessment of existing masonry buildings in aggregate. *Eng Struct.* 2021;247:113218. doi:10.1016/j.engstruct.2021.113218
3. Bernardini C, Maio R, Boschi S, Ferreira T, Vicente R, Vignoli A. The seismic performance-based assessment of a masonry building enclosed in aggregate in Faro (Portugal) by means of a new target structural unit approach. *Eng Struct.* 2019;191:386-400. doi:10.1016/j.engstruct.2019.04.040
4. Valente M, Milani G, Grande E, Formisano A. Historical masonry building aggregates: advanced numerical insight for an effective seismic assessment on two row housing compounds. *Eng Struct.* 2019;190:360-379. doi:10.1016/j.engstruct.2019.04.025
5. Sorrentino L, Cattari S, da porto F, Magenes G, Penna A. Seismic behaviour of ordinary masonry buildings during the 2016 central Italy earthquakes. *Bull Earthq Eng.* 2019;17. doi:10.1007/s10518-018-0370-4
6. Brunelli A, de Silva F, Cattari S. Observed and simulated urban-scale seismic damage of masonry buildings in aggregate on soft soil: The case of Visso hit by the 2016/2017 Central Italy earthquake. *Int J Disaster Risk Reduct.* 2022;83:103391. doi:10.1016/j.ijdr.2022.103391
7. Tomić I, Penna A, DeJong M, et al. Shake table testing of a half-scale stone masonry building aggregate. *Bull Earthq Eng.* Published online November 17, 2023. doi:10.1007/s10518-023-01810-y
8. Tomić I, Beyer K. Shake-table test on a historical masonry aggregate: prediction and postdiction using an equivalent-frame model. *Bull Earthq Eng.* Published online September 8, 2023. doi:10.1007/s10518-023-01765-0
9. Petracca, M., Candeloro, F., Camata, G. ASDEA. manual\_STKO\_Oct\_2021. STKO.com.
10. Command Manual - OpenSeesWiki. [https://opensees.berkeley.edu/wiki/index.php/Command\\_Manual](https://opensees.berkeley.edu/wiki/index.php/Command_Manual)
11. *NTC 2018 - Norme Tecniche per le costruzioni, Italian RuleCode - Decree of the Minister of the Infrastructures.*
12. *DPC-ReLUIs 2010-2013 - Linee Guida per Il Rilievo, l'analisi Ed Il Progetto Di Interventi Di Riparazione e Consolidamento Sismico Di Edifici in Muratura in Aggregato.*
13. Formisano A, Chieffo N, Vaiano G. Seismic Vulnerability Assessment and Strengthening Interventions of Structural Units of a Typical Clustered Masonry Building

- in the Campania Region of Italy. *GeoHazards*. 2021;2(2):101-119. doi:10.3390/geohazards2020006
14. Lagomarsino S, Cattari S, Ottonelli D. The heuristic vulnerability model: fragility curves for masonry buildings. *Bull Earthq Eng*. 2021;19(8):3129-3163. doi:10.1007/s10518-021-01063-7
  15. *Teoria E Tecnica Delle Strutture In Muratura - Augenti Nicola; Parisi Fulvio | Libro Hoepli 01/2019 - HOEPLI.it - ISBN: 978-88-203-8947 5.*
  16. Cescatti E, Vignoli A, Boschi S, Modena C. *In-Situ Mechanical Characterization of Existing Masonry Typologies: A Research Project in Italy Finalized to Update the Structural Codes.*; 2016.
  17. Benedetti A, Pelà L. Experimental characterization of mortar by testing on small specimens. In *15th IB2MaC: developing the future of masonry (pp 1-10) IB2MaC*. Published online June 5, 2012.
  18. Giuffré A, Carocci C. *Codice di pratica per la sicurezza e la conservazione del centro storico di Palermo - Sicurezza e Conservazione del Centri Storici, Il Caso Ortigia I*. Laterza; 1999.
  19. Tarque N, Camata G, Espacone E, Varum H, Blondet M. Numerical modelling of in-plane behaviour of adobe walls - SÍSMICA 2010 – 8° CONGRESSO DE SISMOLOGIA E ENGENHARIA SÍSMICA. In: ; 2010.
  20. Micromodels for the In-Plane Failure Analysis of Masonry Walls with Friction: Limit Analysis and DEM-FEM/DEM Approaches - In Proceedings of XXIV AIMETA Conference 2019 24 (pp. 1883-1895). In: ; 2020:1883-1895.
  21. *Metodi di calcolo e tecniche di consolidamento per edifici in muratura - III EDIZIONE - ISBN 9788857909509. Dario Flaccovio Editore.*
  22. Senaldi I, Penna A. Numerical Investigations on the Seismic Response of Masonry Building Aggregates. *Adv Mater Res*. 2010;133-134:715-720. doi:10.4028/www.scientific.net/AMR.133-134.715
  23. Tena-Colunga A, Ju S. Discussion of: Comparison of Building Analyses Assuming Rigid or Flexible Floors. *J Struct Eng*. 2000;126:272-273. doi:10.1061/(ASCE)0733-9445(2000)126:2(272)
  24. F. Di Trapani. Safety Assessment and Retrofitting of Existing Structures and Infrastructures - didactic material - PUSHOVER ANALYSIS.
  25. Formisano A, Massimilla A. A Novel Procedure for Simplified Nonlinear Numerical Modeling of Structural Units in Masonry Aggregates. *Int J Archit Herit*. 2018;12(7-8):1162-1170. doi:10.1080/15583058.2018.1503365
  26. Lourenco P. Masonry Modeling. In: ; 2015:1419-1431. doi:10.1007/978-3-642-35344-4\_153

27. Lemos JV. Discrete Element Modeling of Masonry Structures. *Int J Archit Herit.* 2007;1(2):190-213. doi:10.1080/15583050601176868
28. Lourenco P. Computations on historic masonry structures. *Prog Struct Eng Mater.* 2002;4:301-319. doi:10.1002/pse.120
29. Dolce M. Schematizzazione e modellazione degli edifici in muratura soggetti ad azioni sismiche / l'Industria delle Costruzioni, 242 (1991).Page 124. 113. In: ; 1991.
30. Serena Cattari. Equivalent frame idealization of walls with irregular openings in masonry buildings , “Equivalent frame idealization of walls with irregular openings in masonry buildings.” *Engineering Structures* 256 (2022): 114055. DOI:10.1016/j.engstruct.2022.114055.
31. Cattari S, Calderoni B, Calì I, et al. Nonlinear modeling of the seismic response of masonry structures: critical review and open issues towards engineering practice. *Bull Earthq Eng.* 2022;20(4):1939-1997. doi:10.1007/s10518-021-01263-1
32. Quagliarini E, Maracchini G, Clementi F. Uses and limits of the Equivalent Frame Model on existing unreinforced masonry buildings for assessing their seismic risk: A review. *J Build Eng.* 2017;10:166-182. doi:10.1016/j.job.2017.03.004
33. Pacella G, Sandoli A, Calderoni B, Brandonisio G. Open issues on non-linear modelling for seismic assessment of existing masonry buildings. *Procedia Struct Integr.* 2023;44:1324-1331. doi:10.1016/j.prostr.2023.01.170
34. Vanin F, Penna A, Beyer K. Equivalent-Frame Modeling of Two Shaking Table Tests of Masonry Buildings Accounting for Their Out-Of-Plane Response. *Front Built Environ.* 2020;6.
35. Vanin F, Penna A, Beyer K. A three-dimensional macroelement for modelling the in-plane and out-of-plane response of masonry walls. *Earthq Eng Struct Dyn.* 2020;49. doi:10.1002/eqe.3277
36. Lourenco P. Analysis of masonry structures with interface elements. *Theory Appl.* Published online January 1, 1994:1-25.
37. Page AW. Finite Element Model for Masonry. *J Struct Div.* 1978;104(8):1267-1285. doi:10.1061/JSDEAG.0004969
38. Ravichandran N, Losanno D, Parisi F. Comparative assessment of finite element macro-modelling approaches for seismic analysis of non-engineered masonry constructions. *Bull Earthq Eng.* 2021;19(13):5565-5607. doi:10.1007/s10518-021-01180-3
39. Petracca M, Camata G, Spacone E, Pelà L. Efficient Constitutive Model for Continuous Micro-Modeling of Masonry Structures. *Int J Archit Herit.* Published online January 2, 2023.
40. Magenes G, Kingsley G, Calvi G. *Seismic Testing of a Full-Scale, Two-Story Masonry Building: Test Procedure and Measured Experimental Response.*; 1995. doi:10.13140/RG.2.1.4590.2962

41. Petracca M, Pelà L, Rossi R, Zaghi S, Camata G, Spacone E. Micro-scale continuous and discrete numerical models for nonlinear analysis of masonry shear walls. *Constr Build Mater.* 2017;149:296-314. doi:10.1016/j.conbuildmat.2017.05.130
42. Zucchini A, Lourenço PB. A micro-mechanical model for the homogenisation of masonry. *Int J Solids Struct.* 2002;39(12):3233-3255. doi:10.1016/S0020-7683(02)00230-5
43. Ma G, Hao H, Lu Y. Homogenization of Masonry Using Numerical Simulations. *J Eng Mech-Asce - J ENG MECH-ASCE.* 2001;127. doi:10.1061/(ASCE)0733-9399(2001)127:5(421)
44. Peng B, Wang D, Zong G, Zhang Y. Homogenization strategy for brick masonry walls under in-plane loading. *Constr Build Mater.* 2018;163:656-667. doi:10.1016/j.conbuildmat.2017.12.133
45. de Buhan P, de Felice G. A homogenization approach to the ultimate strength of brick masonry. *J Mech Phys Solids.* 1997;45(7):1085-1104. doi:10.1016/S0022-5096(97)00002-1
46. Lourenco P, Rots JG. On the use of micromodels for the analysis of masonry shear walls. *Proceeding 2nd Int Symp Comput Methods Struct Mason.* Published online January 1, 1993:14-26.
47. Modal Analysis - an overview | ScienceDirect Topics. <https://www.sciencedirect.com/topics/engineering>
48. Rao SS. *Mechanical Vibrations - 978-0-13-436130-7.* 6° edizione. Pearson College Div; 2016.
49. *Edifici Antisismici in Cemento Armato. Nuove Normative Tecniche. Eurocodici e Classi Di Rischio Sismico. Con CD-ROM - Ghersi, Aurelio, Lenza, Pietro - Libri - ISBN 9788857907758.*
50. PETER FAJFAR\*, Faculty of Civil and Geodetic Engineering, University of Ljubljana, Ljubljana, Slovenia. "Capacity spectrum method based on inelastic demand spectra." *Earthquake Engineering & Structural Dynamics* 28.9 (1999): 979-993.
51. Anil K. Chopra Anil K. Chopra. *Dynamics of Structures - Pearson Education India, 2007.*
52. Eurocode 8: Design of structures for earthquake resistance | Eurocodes: Building the future. <https://eurocodes.jrc.ec.europa.eu/EN-Eurocodes/eurocode-8-design-structures-earthquake-resistance>
53. Albanesi T. Camillo Nuti. "Analisi statica non lineare (pushover)." University La Sapienza in Rome Internal Report, Roma (Italy) (2007).
54. Jain, Ritu. "Solution Procedure for Non-Linear Finite Element Equations." Project Report. University of California, Davis (2003).



55. University of Tokyo course. Satoshi Izumi - Nonlinear Analysis in Civil Engineering - Didactic material (2023).
56. Chambers J, Kelly T. “Nonlinear dynamic analysis—the only option for irregular structures.” 13th World Conference on Earthquake Engineering. 2004.
57. PETER FAJFAR AND PETER GASPERSIC, Department of Civil Engineering, University of Ljubljana, Jamova 2, 61001 Ljubljana, Slovenia. THE N2 METHOD FOR THE SEISMIC DAMAGE ANALYSIS OF RC BUILDINGS.
58. Asdea Software | Software Development for Numerical Simulation and Data Visualization. <https://asdea.eu/software/>
59. Noor-E-Khuda S, Dhanasekar M, Thambiratnam DP. An explicit finite element modelling method for masonry walls under out-of-plane loading. *Eng Struct*. 2016;113:103-120. doi:10.1016/j.engstruct.2016.01.026
60. Saba M, Meloni D. Comparison of different approaches of modelling in a masonry building. *J Phys Conf Ser*. 2017;935:012072. doi:10.1088/1742-6596/935/1/012072
61. Baetu S, Ciongradi I. “Nonlinear Analysis Models of the Reinforced Concrete Structural Walls.” *Proceedings of International Conference DEDUCON—Sustainable Development in Civil Engineering, Iasi. Vol. 1. 2011.*; 2011.
62. 3.1.6.16. ASDConcrete3D Material — OpenSees Documentation documentation. Accessed March 29, 2024. <https://opensees.github.io/OpenSeesDocumentation/user/manual/material/ndMaterials/ASDConcrete3D.html>
63. Oliver J, Huespe AE, Cante JC. An implicit/explicit integration scheme to increase computability of non-linear material and contact/friction problems. *Comput Methods Appl Mech Eng*. 2008;197(21):1865-1889. doi:10.1016/j.cma.2007.11.027
64. Walraven J, Bigaj-van Vliet A. *Walraven, J. C. (2010). The 2010 Fib Model Code for Concrete Structures. Concrete Plant International, 2010(5), 32-37.*; 2010.
65. Boer A, Hendriks M, den Uijl J, Belletti B, Damoni C. Nonlinear FEA guideline for modelling of concrete infrastructure objects. *Comput Model Concr Struct - Proc EURO-C 2014*. 2014;2:977-985. doi:10.1201/b16645-109
66. Guettafi N, Yahiaoui D, Abbeche K, Bouzid T. Numerical Evaluation of Soil-Pile-Structure Interaction Effects in Nonlinear Analysis of Seismic Fragility Curves. *Transp Infrastruct Geotechnol*. 2022;9. doi:10.1007/s40515-021-00161-y
67. Bruschi E, Calvi PM, Quaglioni V. Concentrated plasticity modelling of RC frames in time-history analyses. *Eng Struct*. 2021;243:112716. doi:10.1016/j.engstruct.2021.112716
68. Michael H. Scott\*, January 26, 2011. Numerical Integration Options for the Force-Based Beam-Column Element in OpenSees.

69. Uprety R, Suwal R. Effect of earthquake components on global and local response of RC moment resisting frames. *Asian J Civ Eng.* 2023;24:1-14. doi:10.1007/s42107-023-00583-8
70. Terzic V. “Force-based element vs. Displacement-based element.” University of Berkeley, OpenSees, NEES, & NEEScomm (2011).
71. ZeroLengthContact Element - OpenSeesWiki.  
[https://opensees.berkeley.edu/wiki/index.php/ZeroLengthContact\\_Element](https://opensees.berkeley.edu/wiki/index.php/ZeroLengthContact_Element)
72. Parrinello F, Failla B, Borino G. Cohesive–frictional interface constitutive model. *Int J Solids Struct.* 2009;46(13):2680-2692. doi:10.1016/j.ijsolstr.2009.02.016
73. Kaushik HB, Rai DC, Jain SK. Stress-Strain Characteristics of Clay Brick Masonry under Uniaxial Compression. *J Mater Civ Eng.* 2007;19(9):728-739. doi:10.1061/(ASCE)0899-1561(2007)19:9(728)
74. Marilisa Di Benedetto, Fabio Di Trapani, Sofia Villar, Massimo Petracca, Guido Camata. Seismic response of different masonry building aggregate configurations by a refined fe model - 9th ECCOMAS Thematic Conference on Computational Methods in Structural Dynamics and Earthquake Engineering.
75. “Proceedings of the US Italy workshop on Guidelines for seismic evaluation and rehabilitation of unreinforced masonry buildings.” Proceedings of the US Italy workshop on Guidelines for seismic evaluation and rehabilitation of unreinforced masonry buildings. 1994. <https://nehrlsearch.nist.gov/static/files/NSF/PB95138749.pdf>
76. CNTC19-Circolare applicativa delle Norme Tecniche delle Costruzioni di cui al DM 17/01/2018 (NTC 2018). *Gazzetta Ufficiale*, (42).
77. Bonaventura L, Marmol MG. The TR-BDF2 method for second order problems in structural mechanics. *Computers & Mathematics with Applications*, 92, 13-26.
78. Matjaz Dolsek\*; and Peter Fajfar. Inelastic spectra for infilled reinforced concrete frames. *Earthquake engineering & structural dynamics*, 33(15), 1395-1416.
79. Matjaz Dolsek, Peter Fajfar. “The effect of masonry infills on the seismic response of a four-storey reinforced concrete frame—a deterministic assessment.” *Engineering Structures* 30.7 (2008): 1991-2001.

# Acknowledgements

Desidero esprimere profonda gratitudine al Professor Fabio di Trapani per la sua preziosa guida e disponibilità. Grazie per i fondamentali spunti offerti durante la stesura di questo lavoro e per avermi orientato nei momenti di incertezza. La sua competenza e dedizione sono di grande ispirazione per me.

Un sentito ringraziamento è rivolto a Sofia Villar, che con disponibilità e gentilezza mi ha accompagnato in ogni fase della realizzazione di questo elaborato. Le auguro il meglio nel suo percorso di ricerca accademica e sono convinto che diventerà un'eccellente e rispettata insegnante.

Ringrazio anche il gruppo di ASDEA software di Pescara per aver concesso l'utilizzo del software STKO, indispensabile alla presente ricerca per ottenere risultati di alta qualità. Grazie per il vostro supporto prezioso e la vostra collaborazione.

Un ringraziamento speciale va alla mia famiglia e a Debora, che sono stati un costante sostegno per me.